2013

Design and Improve Energy Efficiency and Functionalities of Electrical Wheelchairs

Dewei Guan
Wright State University

Design and Improve Energy Efficiency and Functionalities of Electrical Wheelchairs

A thesis submitted in partial fulfillment

of the requirements for the degree of

Master of Science in Engineering

By

DEWEI GUAN

B.S., Dalian Jiaotong University, 2010

2013

Wright State University

WRIGHT STATE UNIVERSITY

GRADUATE SCHOOL

May 1,2013

I HEREBY RECOMMEND THAT THE THESIS PREPARED UNDER MY SUPERVISION BY Dewei Guan ENTITLED Design and Improve Energy Efficiency and Functionalities of Electrical Wheelchair BE ACCEPTED IN PARTIAL FULFILLMENT OF THE REQUIREMENTS FOR THE DEGREE OF Master of Science in Engineering.

Hong Huang, Ph.D.

Thesis Director

Junghsen Lieh, Ph.D.

Thesis Director

George Huang, Ph.D., Chair

Department of Mechanical and Materials Engineering College of Engineering and Computer Science

Committee on

Final Examination

Hong Huang, Ph.D.

Junghsen Lieh, Ph.D.

Ha-Rok Bae, Ph.D.

R. William Ayres, Ph.D.

Interim Dean, Graduate School

ABSTRACT

Dewei Guan. M.S.Egr, Department of Mechanical & Materials Engineering, Wright State University, 2013. Design and Improve Energy Efficiency and Functionalities of Electrical Wheelchairs.

There are millions of people who have lost their abilities to walk and wheelchairs offer the ONLY opportunities for their interactions with people and environments outside their houses. These individuals are becoming more and more eager to adapt modern technologies on their wheelchairs to improve quality of social life and the life of freedom. However, most available electric wheelchairs, driven by traditional lead-acid batteries and gear motors, are heavy and bulky in design with low energy efficiency, limited travel radius, and scarce communication/navigation functionalities. This project is to design and prototype an electric wheelchair that is lighter, more flexible in mobility, and more energy-efficient. It will use light-weight high power density Li-ion batteries and be driven by the light and energy-efficient direct drive hub motors. It will be also designed to readily integrate with high-tech accessories for increased independence, connectivity, and useful mobility for disabled individuals. This research is focused on the following four tasks: 1) installing and testing Li-ion battery performances to prolong the wheelchair

running time per charge; 2) installing and testing direct-drive hub motor to reduce the weight and energy loss; 3) designing a dynamometer based on eddy current theory to determine the efficiency of electrical motor; and 4) designing several functional components/accessories, such as iPad holder, automated battery release drawer, and wheel-extend mechanism to improve consumers' onboard independence and convenience

TABLE OF CONTANTS

LIST OF FIGURES

LIST OF TABLES

Chapter 1: Introduction

There are millions of people who have lost their abilities to walk by themselves due to diseases, traffic accidents, wars, and natural disasters etc. Meanwhile, with the growth of population and progress in medical technology, an aging society has become one of the most important issues that many countries have to take seriously in consideration. For these individuals, wheelchairs offer the ONLY opportunities for their interaction with people and environments outside their houses. Currently, more than 3.3 million people in the US over the age of 15 reply on wheelchairs, and this number is expected to increase as Baby Boomers age over the next few decades [1-3].

To improve quality of social life and the life of freedom, people with disabilities are becoming more and more eager to adapt modern technologies on their wheelchairs. Unfortunately, the advent of battery-powered motorized wheelchairs developed in the 1950s represents the single major innovation in wheelchair technology over the last century. Subsequent incremental improvements in performance and functionality have not kept pace with changes in the rest of society. However, most available electric wheelchairs are still heavy and bulky in design with low energy efficiency, limited travel radius and scarce communication/navigation functionalities.

The objective of this project is to design and manufacture an electric wheelchair

that is lighter, more flexible, and more energy-efficient. It will use light-weight high power density batteries that will be easier/faster to recharge and replace. It will be driven by the lighter and more energy-efficient motors. It will be also designed to readily integrate with high-tech accessories for increased independence, connectivity, and useful mobility for disabled individuals.

1. Basic Components of an Electric Wheelchair

An electric-powered wheelchair is a wheelchair that is moved via the means of electrical motor and navigational controls. The electric drive system for wheelchairs normally consists of power converter, motor/reducer, controller, and energy storage unit (battery). Besides the three major key components, seat and accessories are also very important in Electrical Wheelchair Design.

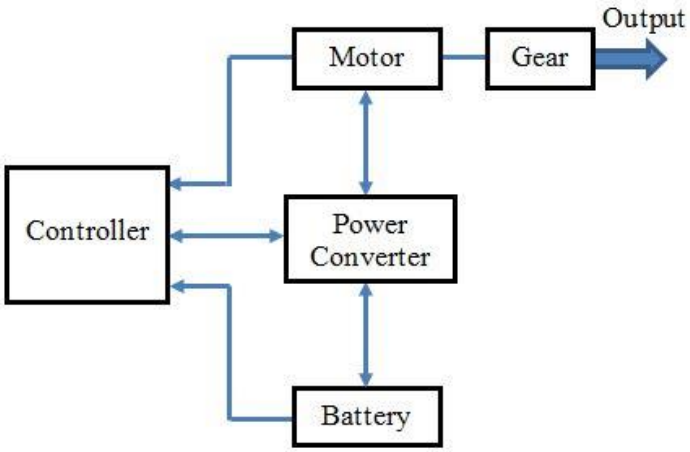

Figure 1.1 Block diagram of a typical electric drive system in an electric wheelchair

Figure 1.1 shows a standard block diagram of an electric drive system in electric wheelchairs. The battery supply electric energy to the wheelchair. The motor is to convert electric energy into mechanical power thus to drive the wheel in motion. The function of the power converter is to ensure proper voltage and current delivered to the motor system. The controller commands the power converter using control signals and modulates the operation of the motor in order to produce proper speed and torque.

1.1 Motor

The key component in the drive system is the motor. DC motor is widely used in wheelchairs because of its simplicity and technological maturity, and capability in handling variable speed, frequent start/stop, reversing, and braking. A brushless DC motor (BLDC) is created by inverting the stator and rotor of a conventional DC motor by abandoning its mechanical commutator and slip rings, having advantages including the use of electronic switches, the ability to produce a large torque, and more cross-sectional area for armature windings. BLDC motors can be subdivided into sensored BLDC motors and sensorless BLDC motors. Sensorless BLDC motors use EMF voltage, instead of using position sensors, to detect rotor magnet positions. The elimination of position sensors not only reduces the size and cost of the motor but also increases the reliability of the whole system.

The system efficiency of a DC motor is very low at low-speed regions. With the assistance of a gear reducer, the speed of the motor can operated at high-efficient ranges. However, the gear reducer increases the weight and reduces energy efficiency. Alternative motor concepts, such as 3-phase sensorless BLDC motors and direct drive

(DD) DC motors, are in development and integration into the electric wheelchairs for high efficiency. *Figure 1.2* present typical conventional DC motor with reducer, 3-phase sensorless BLDC motor, and DD DC motor. *Table 1.1* compares the weight and efficiency of the three types of motors, the advantage of Direct Drive motor is 20% higher energy efficiency and in order to produce 1HP, it only need 5.0lb. Because of its simplicity, lightweight and high-efficiency property, DD DC motor is the promising candidate in next generation electric wheelchairs.

Figure 1.2 Three different types of motors for electric wheelchairs

Table 1.1 Weight and efficiency comparison of the three types of motors

	Standard DC Motor	Sensorless 3-phase BLDC Motor	Direct Drive (DD) DC Motor
Energy Efficiency	Low (70%)	High (90^+ %)	High (90^+ %)
Motor (1 HP)	7.5 lb	0.7 lb	5.0 lb
Gear Reducer	4.7 lb	4.7 lb	N/A
Total Weight	12.2 lb	5.4 lb	5.0 lb
Weight Reduction	------	55.7%	59.0%

1.2 Battery

The motors of electrical wheelchairs are usually powered by 12Vor 24V, 4 to 8 amp rechargeable deep-cycle lead-acid available in wet or dry options. Many electrical wheelchairs carry an on-board charger which can be plugged into a standard wall outlet. Older or more portable models may have a separate charger unit.

Table 1.2 shows the comparison of lead-acid batteries with lithium-ion batteries in the market. The advantage of lead acid batteries is obvious in terms of technology maturity and low cost, their performances in the aspects of energy efficiency, cycle life, charging time as well as self- discharge are the worse than Li-ion batteries. As can be seen in table 1.2, Li-ion batteries have high operating voltage (3.3-3.7V), highest energy conversion efficiency (over 90%), shortest charging time, longest cycle life (up to 2000 cycles), and lowest self-discharge rate etc. Unfortunately, lead-acid batteries are still dominant in the motorized wheelchair markets.

The Ni-MH battery technology was attempted to use in some wheelchair models. Ni-MH battery reduces weight by about half and increase energy density by 80% compared to lead-acid technology. However, this gain is relatively small compared to the cost, which is almost six times the cost of lead-acid per Watt-hour (Wh). The reduction in weight without increased performance in other areas has not been sufficient to overcome the price difference between Ni-MH and lead-acid systems. Consequently, Ni-MH batteries have not been widely adopted in wheelchairs.

Table 1.2 Comparison of lead-acid batteries and different kinds of Li-ion batteries [4, 5]

Battery Type	Lead acid Battery	Li-ion Batteries		
		$LiCoO_2$	$LiMn_2O_4$	$LiFePO_4$
Specific energy	30–40 Wh/kg	100-265 Wh/kg		
Energy density	60-75 Wh/L	250-730 Wh/L		
Specific power	180 W/Kg	250-340 W/Kg		
Operating Voltage	2V	3.7V	3.7V	3.3V
Patent protection	No	No	No	Yes
Price	1	4	6	10
Security	Good	Bad	Middle	Good
Green Product	No	Yes	Yes	Yes
Memory effect	No	No	No	No
Energy efficiency	60%	90%	90%	95%
Cycle life	400	500	500	2000
Charge time	8 Hours	2-4 Hours	2-4 Hours	2 Hours
Self-discharge	20% Month	10% Month	10% Month	8% Month

At the moment, cost and safety have been the primary barriers to Li-ion batteries used in wheelchairs. Recently the development of $LiFePO_4$ cathodes for use in Li-ion battery technology has improved both the cost and safety profile for Li-ion systems. Current Li-ion systems have the advantages of high energy per unit volume (0.23 Wh/cm^3 vs. 0.11 Wh/cm^3 for lead-acid and 0.15 Wh/cm^3 for Ni-MH), high energy per unit weight (170 Wh/kg vs. 36 Wh/kg for lead-acid and 65 Wh/kg for Ni-MH), and only marginally higher cost ($0.47/Wh vs. $0.17/Wh for lead-acid and $0.99/Wh for Ni-MH). According to Deutsche Bank, estimate cost of Li-ion technology will be less than $0.30/Wh by the end of the decade with little change in the cost of lead-acid and Ni-MH technology.

Current Li-ion batteries have at least doubled the operating time per charge and can be used at about 5 years without major maintenance required. It is anticipated that more wheelchair designs will incorporate Li-ion technology over the next few years as designers and manufacturers make the switch and consumers agree to pay a small upfront premium for reduced weight, shorter charge times, longer run times, and longer battery life.

Some other technologies like regeneration motor, fuel cell, solar power sunroofs are being studied in some electric wheelchair design.[6] Figure 1.3 shows a prototype installed a solar panel on the top, a fuel cell stack and the battery on the back and under the wheelchair, respectively. However, this technology is way from commercialization in consideration of the safety, cost, and convenience.

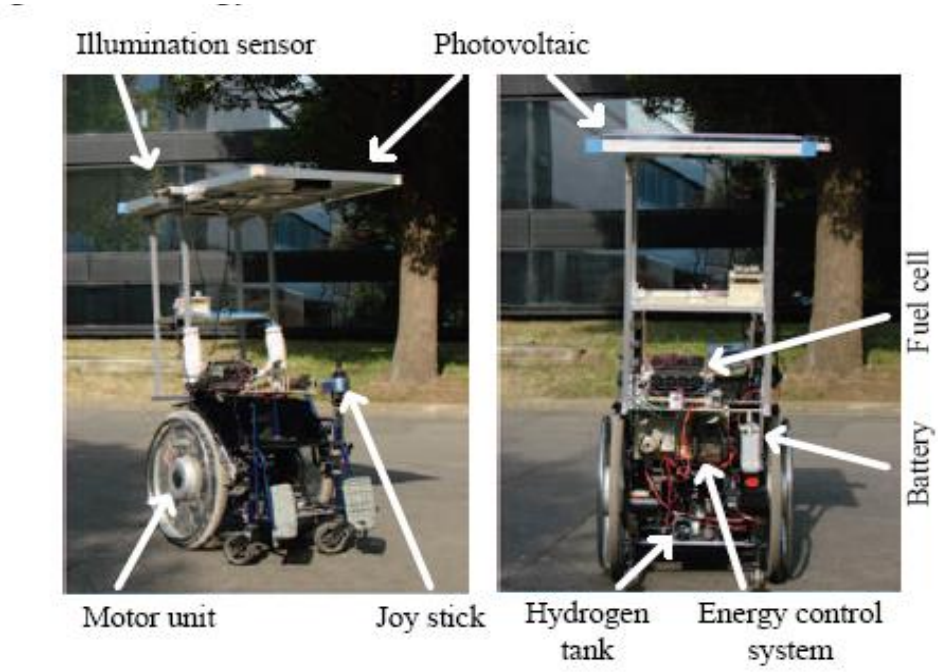

Figure 1.3 A prototype electric wheelchair powered by three different power sources, i.e. batteries, fuel cells, and solar cells for extending the operating time [6]

1.3 Drive Systems

There are four general styles of drive systems: front, center, rear wheel and all-wheel drive. Powered wheels are typically somewhat larger than the trailing or castoring wheels, while castoring wheels are typically larger than the castors on a manual chair. Centre wheel, which drives electrical wheelchairs, have castors located both in the front and in the rear for a six-wheel layout. Some manual wheelchairs may also be fitted with an auxiliary electric power system. This can take one of three forms: 1) integrated with the hub of hand-propelled wheels so that any force on the push rims is magnified by the drive system, 2) mounted under the wheelchair and controlled as for an electrical wheelchair but with the motive force either transmitted to the main wheels via a friction drive system, or 3) delivered directly through an auxiliary drive wheel.

1.4 Controller

Controllers are most commonly an arm-rest mounted joystick which may have additional controls to allow the users to tailor sensitivity or access multiple control modes. The controller may be swing-away to aid in side-transfers. For users who are unable to use a hand controller various alternatives are available such as sip-and-puff controllers, worked by blowing into a sensor. In some cases the controller may be mounted for use by an aide walking behind the chair rather than by the user. Capabilities include turning one drive wheel forward while the other goes backward, thus turning the wheelchair within its own length.

The most important advances come from greater use of microprocessors and computer technology. Technological researches making use of voice, eye, head gesture,

and even tongue gesture etc. to control wheelchairs emerge rapidly. Such control system can be more convenient and save effort for user to drive, especially for those severely disabled person. For instance, the tongue gesture estimation modules can be captured with the help of a camera.[7] For making the system safer and usable, obstacle avoidance and a real-time vibrotactile feedback modules are added to the system to inform the user by attaching 12 micro motors which can rotate at a certain frequencies arranged in a 2D array on the back of the Electrical Wheelchair and when an error occurred due to incorrect recognition by the tongue gesture estimation modules the user will notice by the abnormal vibration stimuli from the back.

Most recently, 'thought (brain)-control' of electrical wheelchair was reported and has been demonstrated in the laboratory environment, as shown in Figure 1.4 [8]. The robotic chair could revolutionize life for those with severe disabilities who are unable to use a conventional joystick. It works by the detection of brainwaves or nerve signals via sensors on the scalp or elsewhere, creating a three-dimensional picture of the area around it. To steer the chair, the user simply concentrates their thoughts on the part of the display where they want to go. Electrodes in a skullcap then detect the brain activity of the users - and work out their destination.

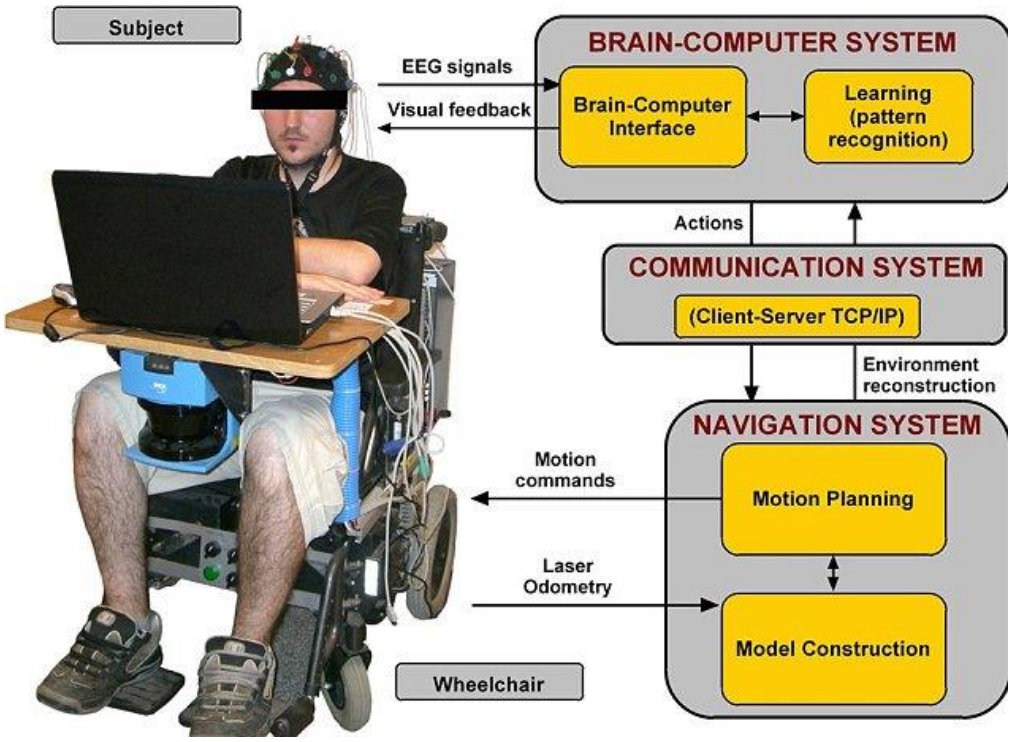

Figure 1.4 A conceptual advanced electric wheelchair with onboard navigating and communicating system and the ability of hand- free brain control [8]

Implementing a Laser-Based Road Detection and Recognition (LRF) system into an electrical wheelchair is a new way to improve wheelchair operation and safety. However, most road recognition systems cannot observe road conditions in detail and can be affected by scanning observation error and paved or unpaved road, water surface and fallen leaves etc. Adding a vision sensor module may allow the application of color information in road recognition, but color varying in different lighting conditions is still challenging to be solved. Moreover road recognition which is based on the combination of LRF and vision sensors requires a large amount of computational time. Figure 1.5 shows the Multi-layered LRF (MLRF) integrated on a wheelchair [9]. This consists of road detection and road edge detection by analyzing the road from laser image in static out door environments.

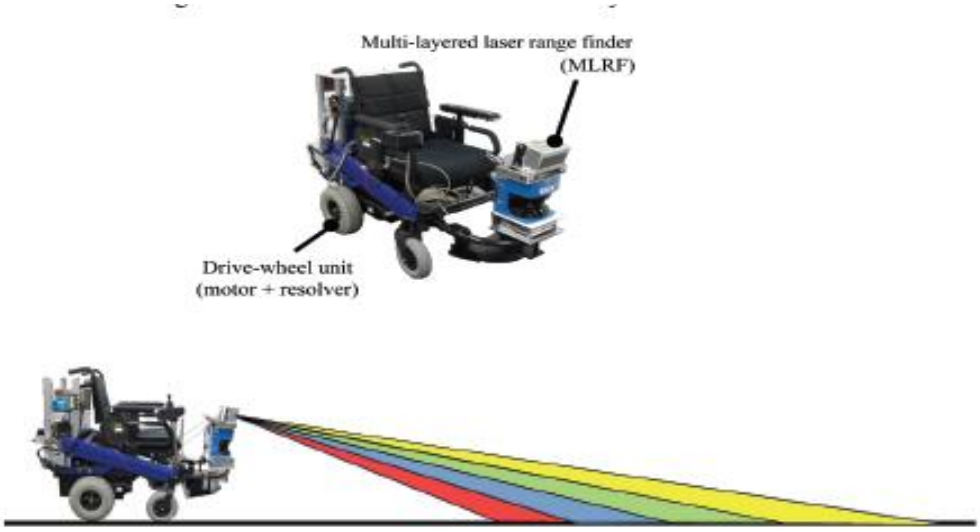

Figure 1.5 Scan planes of the MLRF; four different colors denote the laser layers **[9]**

1.5 Seating and Accessories

The sling seat is usually found on low-end manual wheelchairs. The seating on an electrical wheelchair is frequently in a 'captain's chair' design. Head rests are a common adaption and specialist seating solutions are available for users who need individually tailored support. Leg rests may be integrated into the seating design and may have powered adjustment for those users who need to vary their leg position. Electrical wheelchair may also have a reclining facility for users who are unable to maintain an upright seating position indefinitely.

The accessories of a power wheelchair can be divided into two categories: basic and revolutionary parts. The basic accessories like cushion, Lap tray, Beverage holder, Drink aid and etc. are used for making the Electric wheelchair more convenient and comfort to use (see *Figure 1.6*). The revolutionary improvements of an electric wheelchair, are to make it more intelligent and extend the operate time, by combing or adding some

electronic devices to the electric wheelchair. Certain high-end electrical wheel feature a 'standing' capability in which either the entire seat elevates to bring the user to standing height or the seat-base, seat-back or leg rests move in conjunction to bring the user into an upright position. For instance, *Figure 1.7* shows iBot can climb stairs and make the user stand up to a height of average person.

Figure 1.6 A few examples of basic accessories installed on prototype wheelchairs

Figure 1.7 A prototype of iBot electric wheelchair that "stand up" to a height of an average person

2. Scope of This Research Project and Thesis

As addressed in the previous sections, despite significant advancements in battery [10-15], drivetrain technologies [16-19] and the availability of computer-aided assistive technologies for individuals at all levels of ability. The development of current electric wheelchair has been relatively stagnant, preventing many individuals who use wheelchairs from participating in education, work, and pleasure activities available to the rest of the population. For instance, just name a few:

1) Most consumer chairs use older battery technology and less efficient motors, leading to problems of diminished power capacity and therefore limited travelling range with restricted functionalities.

2) At present, people have been toting smartphones, laptops, cameras, GPS units, and other electronic items with them through daily life. For customers' satisfaction and safety concerns, many new cars are now coming with onboard computers which can pull together all the controls, communication, navigation, and instant assistance solutions. However, even the latest powered wheelchairs have not advanced at the same pace, still concentrating only on the medical needs of the users. In order to adapt in the modern high-tech lifestyle, people on the chair have to find their own ways to Velcro, duct tape, glue, screw, etc, to attach all the same devices everyone else carries (and often more!).

3) The wheelchairs are not optimally designed to assist disabled individuals with integrating into the workforce or with other activities of daily life. They are commonly bulky and unwieldy, often too wide for doorways; there are less assistive solutions to those with additional upper torso, vision or hearing disabilities in the working/business

environment. A typical power wheelchair will not fold up or come apart. Most individuals who need to travel rely on a van or larger vehicle to store the power wheelchair; or the users may have to purchase an additional manual wheelchair for road trips.

4) An electric wheelchair is an expensive piece of equipment that includes multiple electrical components and a motorized element which will cause a series of difficulties to maintain. Any problems that occur with the chair usually will have to be resolved by a mechanic, which results in additional charges.

In the past few years, many new concepts and technology have emerged in the development and advancement of electrical wheelchairs. These efforts and studies towards solving the drawbacks mentioned above and improving the performances of an electric wheelchair are briefly reviewed in this introduction chapter.

Since the objective of this project is to design and prototype a wheelchair that is lighter, more flexible in mobility, and more energy-efficient, the past efforts and studies in the area related to this project area, i.e. batteries, motors, and accessary design, are briefly reviewed in chapter 2.

Short operating time of battery compared to customer high demand need to be addressed urgently. In this study, high- performance battery and motor, with improved energy density, energy efficiency and reduced weight of the wheelchair, are tested and compared with the traditional power/motor system. The results are presented in chapter 3.

To quantify the improvement of the energy efficiency before and after installing the hub motor, a dynamometer based on eddy current brake is designed, manufactured and

modified. Primary computational analyses on stresses and heat transfer are later conducted. These results are presented in chapter 4.

Meanwhile, to increase the user experience and makes it more functional, several accessories like Ipad holder, onboard power outlet, and automated rapid battery release mechanism are designed, which is presented in chapter 5.

The summary and reference list can be found at the end of the thesis.

Chapter 2: Literature Review

With the rise of demands on new light, comfortable, energy-efficient electric wheelchairs, there are more and more new concepts and technology are emerging from design engineers and inventors. The most important advancements are emphasized on highly cost-effective batteries, high efficient motor, and greater use of microprocessors. With the combination of these new technology and components, the electric wheelchair will become more comfortable and convenient to the consumers. This chapter will review some latest studies and testing results which are relevant with the objectives of this project.

1. Studies on Battery Power System

1.1 Exemplary Performances of a Lead Acid Battery

Due to its safety, inexpensiveness, a relatively good performance and environmentally friendly [20], the lead acid battery has dominated the market of electric wheelchair, golf cart, engine starter of automobile and even in a nuclear submarine. However, with the use of a lead acid battery utilized in electric wheelchairs, the disadvantages and limitations are apparent such as low current rate restricted temperature operating range etc.

The following results studied by Panasonic show the performance of Panasonic lead acid batteries tested under different charge and discharge current and temperatures. Each

test was repeated three times under CC/CV charge/discharge method. [21]The discharge capacities of a typical lead acid battery tested at the different current rate and temperatures are plotted in *Figure 2.1*. From the figure we can see, under the discharge current of 0.05CA, 100% of the capacity could be delivered, but as the discharge current increase to 1CA, the percentage of the capacity decreased rapidly from 100% to 63%. In addition, the figure indicated discharge performance of a lead acid battery not only influenced by output current but also affected by the ambient temperature, at the output current of 0.25CA, the percentage of discharge capacity changed from 81% to 44% ,when the ambition temperature change from 50°C to -20°C.

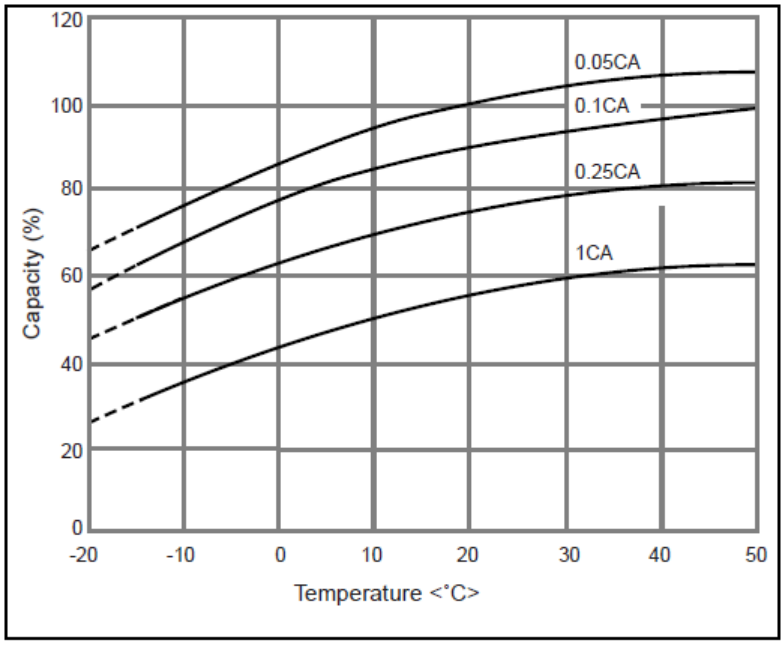

Figure 2.1 Discharge performance of a typical lead acid battery

The voltage and current as a function of time during a charging process of the same lead acid battery are showed in Figure 2.2, the maximum safety charge current is only up to 0.4CA, which means a long time charging is needed.

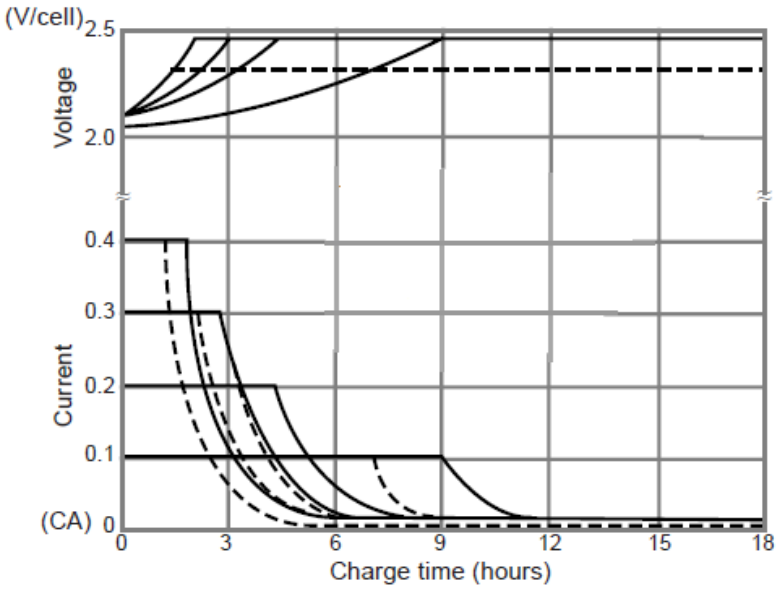

Figure 2.2 Charge performances of a typical lead acid battery at the charge condition:cut off voltage 2.45 V/cell and Temperature of 25°C

The cycle life of lead acid battery were shown in Figure 2.3,cycly life dependent on the depth of discharge in each cycle. Under a constant discharge current, the deeper discharge cycle is the smaller time of cycles will be. As the result,the maxmium number of lead acid battery life cycles is 1200, under the 30% depth of discharge.

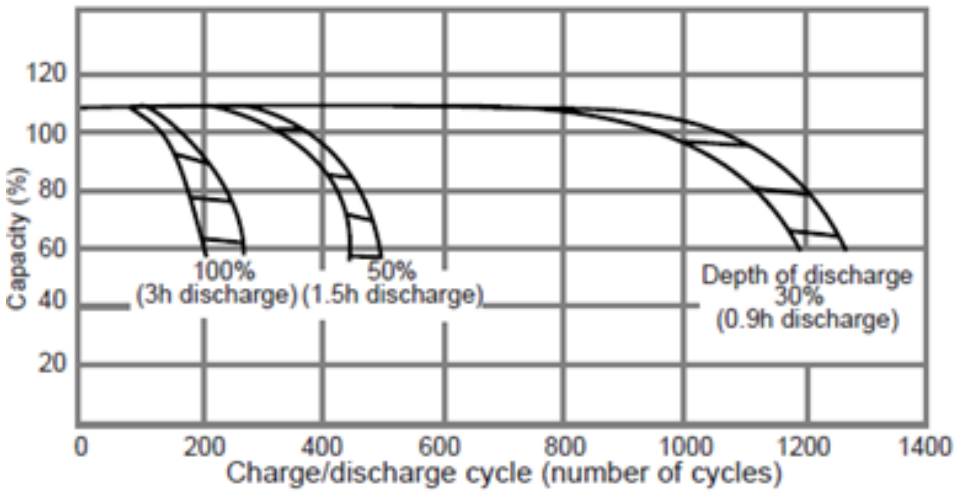

Figure 2.3 Depth of discharge vs. charge/discharge cycle number

We can draw the conclusion that the lead acid battery is not fit for large current output. And the long time needed for fully charging a lead acid battery is a serious obstable for people in their daliy use. In addition, we notice that if the output current over 3CA may result a permanent reduction of discharge capacity or decreasement in the time of repeatable discharge cycle, and compare to output current, low tempreature is a key factor for determing the performance of lead acid battery as well.

1.2 Exemplary Performances of a Li-ion Battery

Compared with lead acid battery, Li-ion technology not only provides a lighter weight, shorter charge times, and longer battery life but also offers safety improvements over previous battery technology in terms of retaining thermally stability when presented with electrical or physical abuse, eliminating free-electrolyte refilling and acid concerns, and eliminating hydrogen generation etc. [22] Phosphate-based Li-ion batteries have gained acceptance as a leading technology in electric automobiles (e.g. the Chevy Volt). It is anticipated that more wheelchairs will incorporate the Li-ion technology over the next few years as designers and manufacturers make the switch and consumers agree to pay a small upfront premium.

Mitsubishi Heavy Industries introduced the test result of a high performance lithium-ion battery “P140” and “P060”, whose specifications are listed in *Table 2.1*. [23]

Table 2.1 Specifications of the P140 and P060 li-ion batteries [23]

Item		P140 battery	P060 battery	Remark
Nominal capacity		50Ah	20Ah	0.2C,25°C
Nominal voltage		3.7V	3.7V	
Voltage range		4.15-2.70V	4.15-2.70V	
Energy density per weight		132 Wh/kg	87 Wh/kg	
Operational temperature range	Charge	0 to 50 °C	0 to 50 °C	
	Discharge	-20 °C to 5o °C	-20 °C to 50 °C	
	Storage	-30 °C to 40 °C	-30 °C to 40 °C	
Maximum Current	Continuous	100A	100A	25°C
	Instantaneous	300A	300A	25°C,10s
Cycle life		3500 cycles or more	3500 cycles or more	80% DOD@1C
Self-discharge rate		2% or less	2% or less	Per month
Weight		1.4kg	0.85kg	

The charging performances of the two batteries are shown in *Figure 2.4(a) and (b).* The test was conducted by using CC/CV (constant current/constant voltage) charge method, full charging was considered as CC: 4.15Vor CV: 0.02C in a 25°C thermostatic bath. The charge current varies from 0.2C to 8C. For P140, 90% or more was achieved during 2C-CC charging, 80% of charging capacity can be achieved during 6C-CC charging. In the case of P060, 96% or more of capacity was available under the charge current of 0.2C-CC.

The fully discharge condition was considered as CC: 2.7V and a good discharge rate characteristic of P140 and P060 can be seen from *Figure 2.5(a)* and *(b).* At the discharge current of 2C (100A) the capacity that can be withdrawn is as high as 95%. As the current increased to 6C (300A) a high capacity ratio of 94% still maintains. Under the discharge current of 15C (300A), the capacity up to 85% or higher is still able to be used.

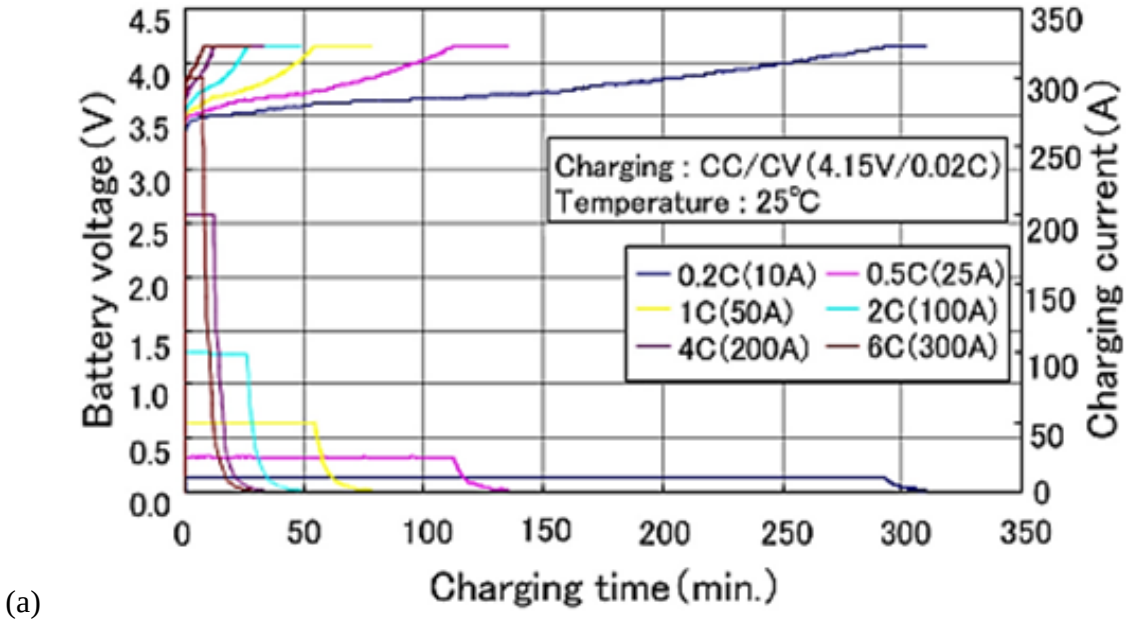

(a)

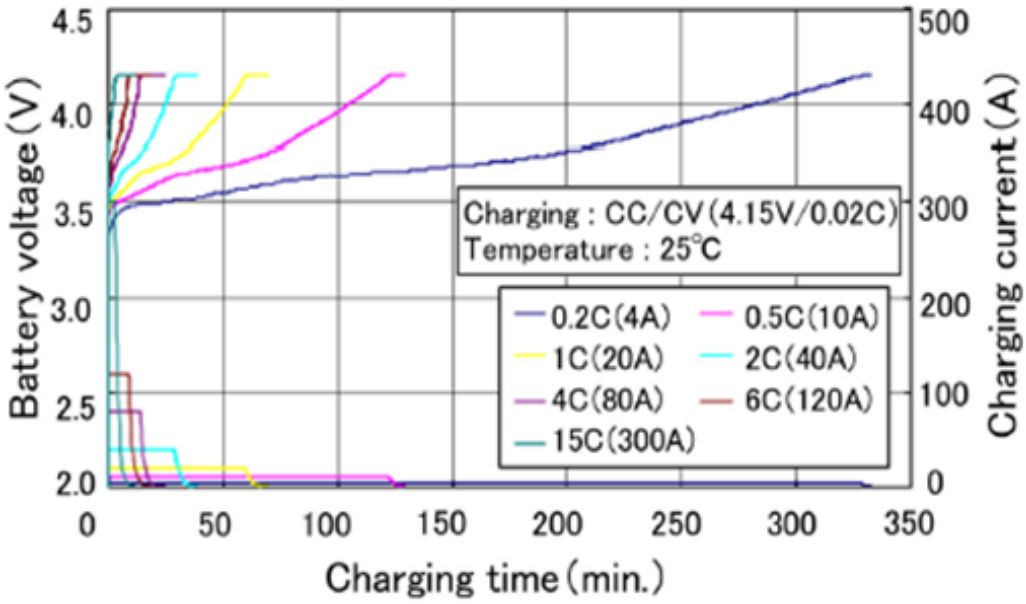

(b)

Figure 2.4 Li-ion battery charge characteristics obtained at the different charging current and 25°C. (a) P140 battery and (b) P060battery [23]

(a)

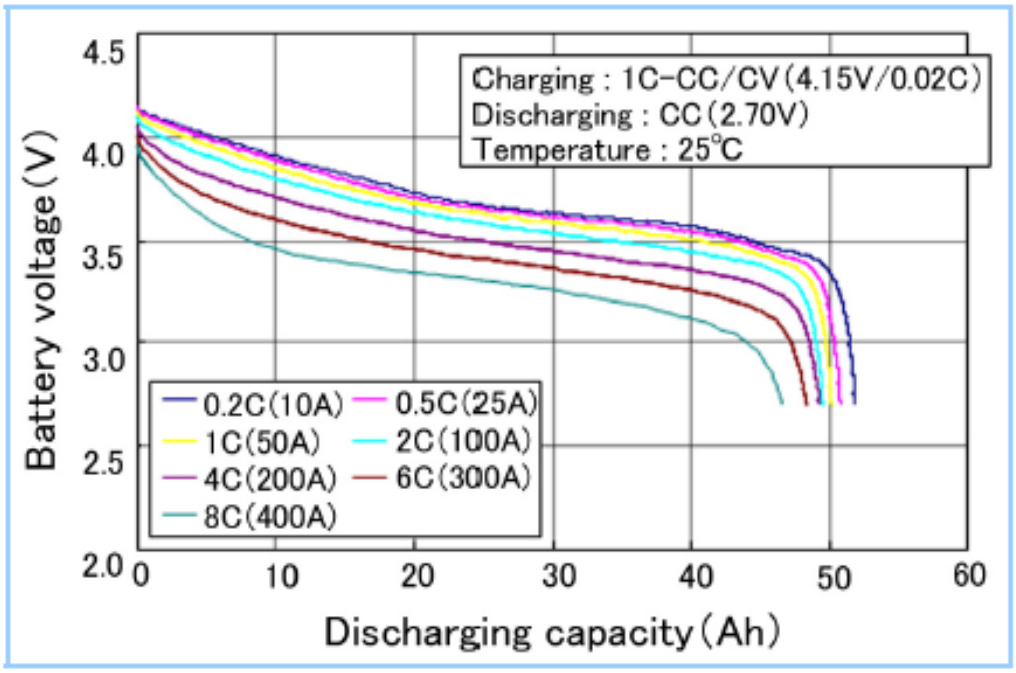

(b)

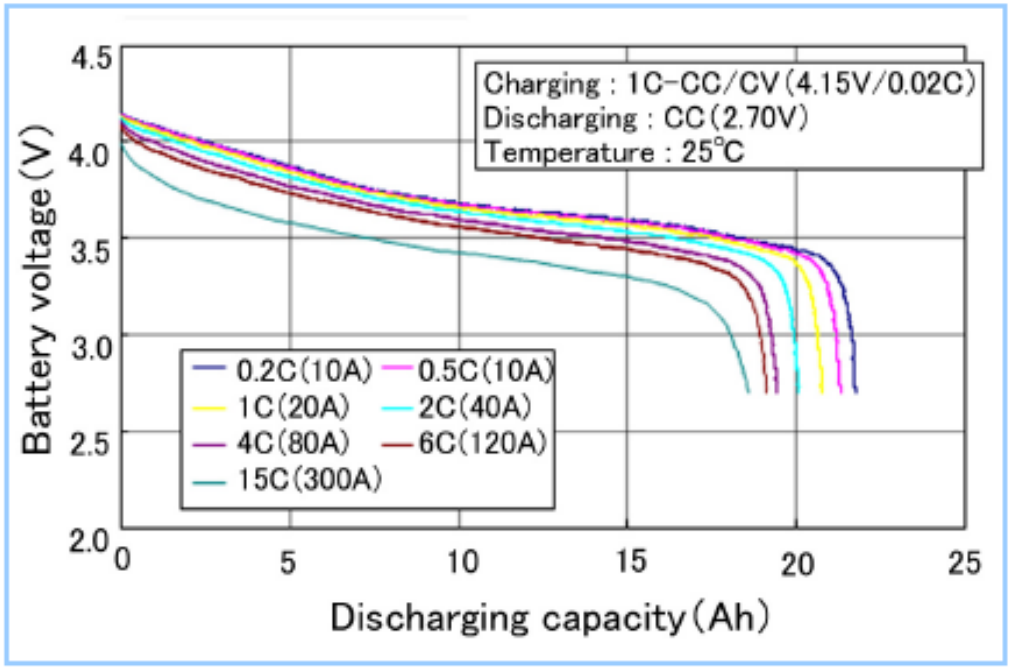

Figure 2.5 Li-ion battery discharge characteristics obtained at the different current and at 25°C. (a) P140 battery and (b) P060 battery [23]

The low temperature performances of P140 and P060 battery are shown in *Figure 2.6(a)* and *(b).* Each battery was fully charge before the test, fully charge condition was 1C-CC/CV CC: 4.15V cut and CV: 0.02C cut. The discharging cut was 1C-CC: 2.7V at each temperature condition. Normally, 80% of the capacity can be easily maintained at a low temperature of -15^{o}C. Meanwhile, even at the most worst temperature condition of -30^{o}C, 66% of the capacity still can be achieved

(a)

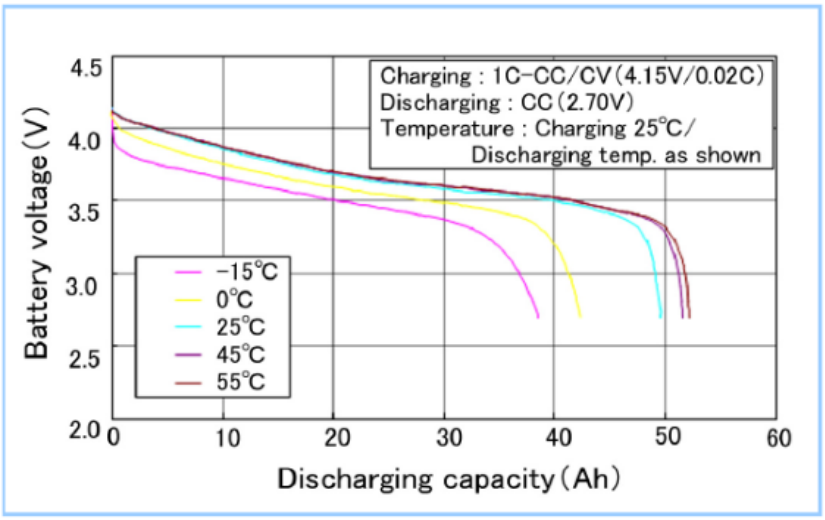

(b)

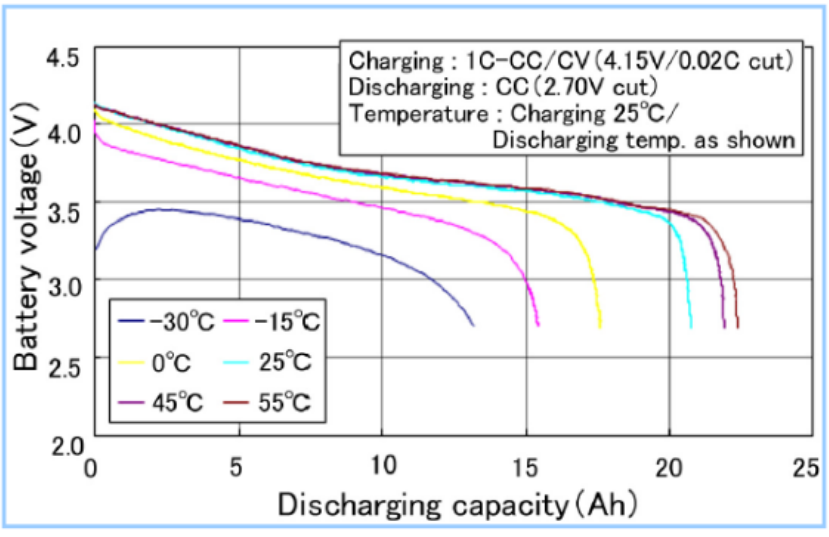

Figure 2.6 Li-ion battery discharge characteristics at low temperatures. (a) P140 battery and (b) P060 battery [23]

2. Studies in Motor System

2.1 Exemplary Design and Performances of a Rim Motor

Y.P. Yang and C.W. Lai proposed a concept of changing the rim on hand push wheelchair into a rim motor *(Figure 2.7)* to generate an enlarged torque through a large diameter of rim. [24] According to the authors, the large wheel provides better mobility over rough road.

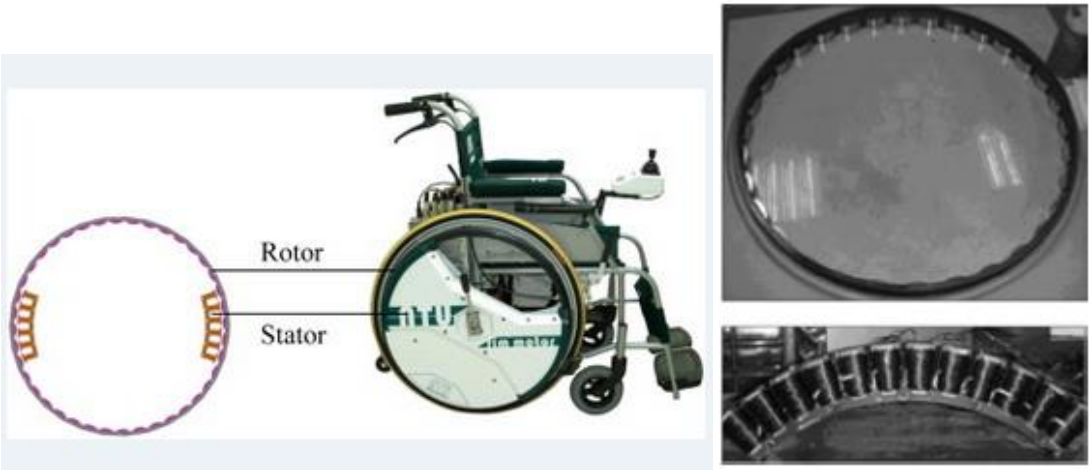

Figure 2.7 A prototype of a rim motor for electric wheelchairs [24]

The author presented the dynamic analysis and magnetic circuit model of rim motor in order to determine the factor of motor design. Afterwards, mathematic method and FEA method were used to optimize the initial design to increase the output torque and efficient. In the table 2.2, inner and outer radius represented by Rri and Rro,Ws and Ns is the width of slot and number of teeth in the stator, Tr is short for Torque ripple which is the design objective.

Table 2.2 Rim Motor Optimization Studies in Reference [24]

Design	Case1	Case2	Case3	Case4
Tq:Tq/W:Tr:Ωmax	1:1:4:2	1:1:8:3	2:1:7:1	2:1:5:1
Rri (mm)	220	220	230	220
Rro (mm)	180	180	166	180
⌀ (mm)	1	1	1	1
Ws (mm)	6	5	6	6
W(kg)	3.86	3.76	5.00	3.77
Tr(%)	15.3	13.4	21.4	19.0
MaxTq (Nm)	28	24	43	35
Tq/W (Nm/Kg)	7.20	6.44	8.50	9.26
Ωmax (rpm)	113	130	73	90

Meanwhile, the authors collected testing data from a prototype. The torque constant is 5.53Nm/A. The maximum toque is around 28.35Nm and maximum speed of 130 rpm, which satisfied the require specifications for a general purpose wheelchair. The maximum efficiency is about 54% at 100rpm. The result was not improved as much as expected which was attributed to optimal current in the back-emf form contaminated by many high frequency harmonics and noise.

2.2 Exemplary Performances of a Hub Motor

Hub motor is a mature product base on the brushless motor *(Figure 2.8)*. Hub motor incorporates into the hub of a wheel and drives it directly without gearing. Due to not having gear transmission inside, no lubricating oil, broken gear replacement and easy maintenance become the outstanding advantages for long time use. Having the hub motor being directly controlled by wire it will have a faster reaction on brake and turn to avoid a collision. Active brake bias renders that each wheel can brake individually for adjusting response to other inputs to maintain the stability of a vehicle. Hub motor reduces the cost and weight of traditional mechanical transmissions like gearboxes, differentials and drive

shafts commonly used in gear motors *(Figure 2.9).* Further, there are no transmission energy losses resulting in the improved efficiency.

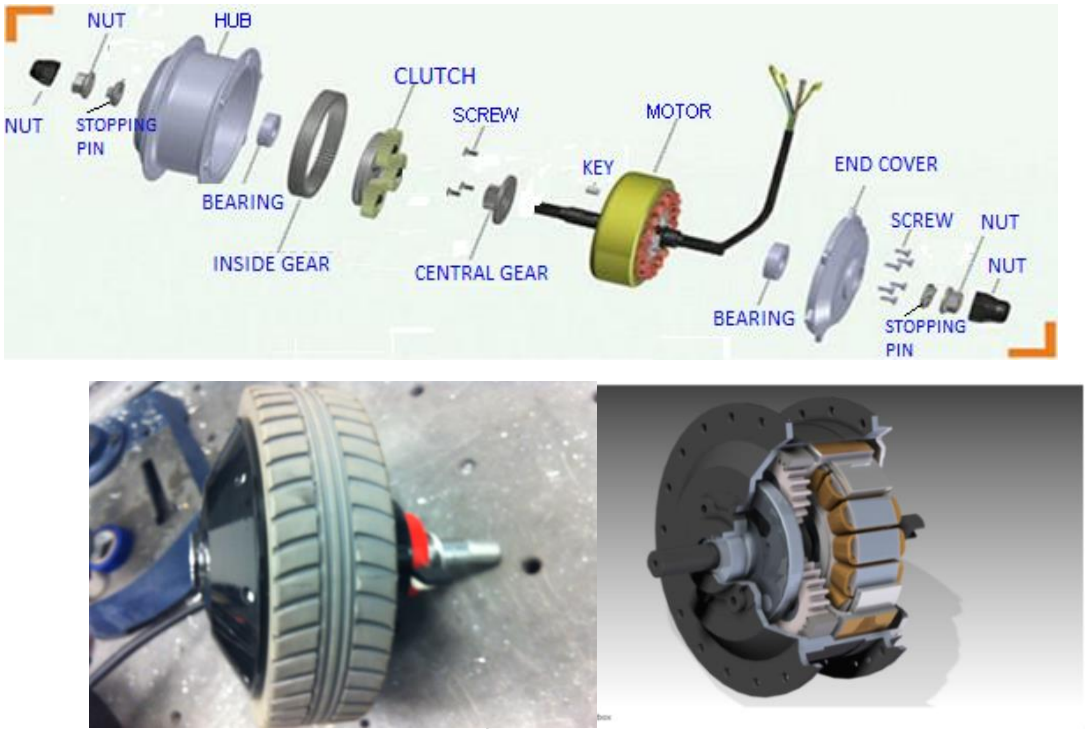

Figure 2.8 The explosive view (above) of a hub motor (bottom left) and section view (bottom right) of its planet gear transmission system [23]

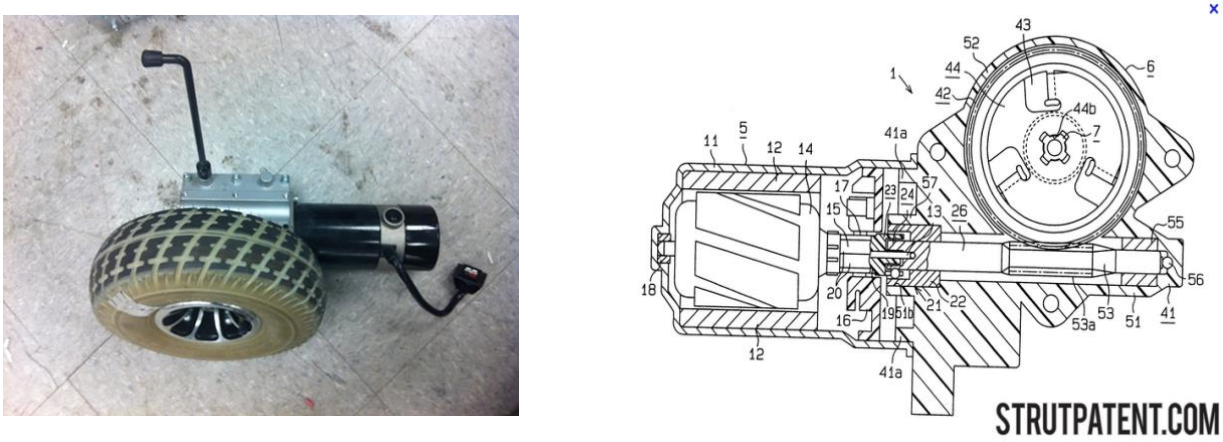

Figure 2.9 The image of the gear motor comes with Pride Jazzy 1113 and structural sketch of such a system in the sectional view [23]

3. Studies on Eddy Current Retarders

Two automobile engineers C. Y. LIU and K. J. JIANG introduced the design and test of an eddy current retarder.[25] The retarder is consisted of eight cores, an air gap, coils and rotor plates. When the driving shaft begin to decelerate or brake. A magnetic line among the stator, air gap and two rotor plates constitutes a loop which will generate a torque to against the input power *(Figure 2.10).*A mathematical model was developed to design the retarder with a brake torque of 1900Nm.

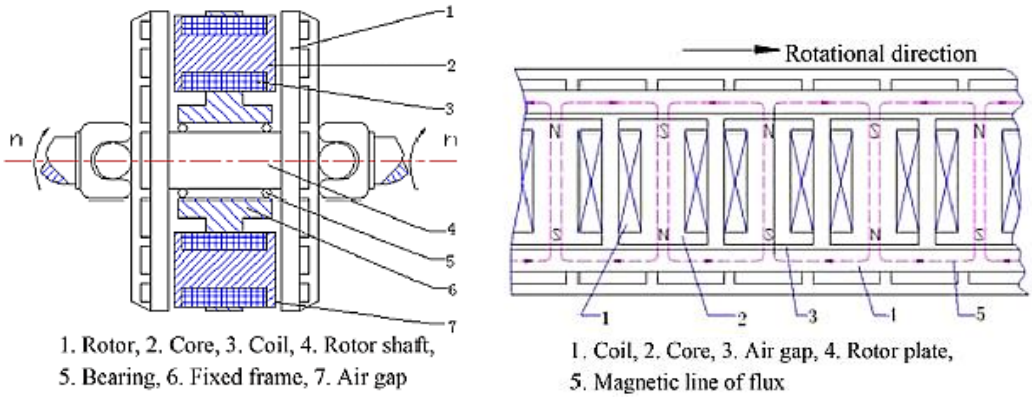

Figure 2.10 Sketch sectional view (left) and the location of each component (right) of an eddy current retarder [24]

In the section of design, parameters of this retarder were determined by the equation below, for instantaneous power of the eddy current retarder is as follows:

$$\rho = \frac{2S^2\Delta_h B^2\omega^2 sin^2\omega t}{\pi\rho} \tag{2.1}$$

Where S is the air-gap area of magnetic, Δ_h is the equivalent skin depth, B is the magnetic induction density, ω is the angular velocity of the magnetic field in the air gap, and ρ is the resistance of the rotor plate.

The effective braking power is given as follows:

$$P = \frac{1}{T}\int_0^T = \frac{s^2 \Delta_h B^2 \omega^2}{\pi\rho} \tag{2.2}$$

Accroding $P = T\omega_n$ the brake torque could be given as follows:

$$T = \frac{N_p^2 S^2 \Delta_h B^2 \omega_n}{\pi\rho} \tag{2.3}$$

The test of eddy current retarder was carried out at ambient temperature of 20°C and the results are shown in *Figure 2.11* and *Figure 2.12*. With the brake time increased, the temperature in the rotor plate went up from rapidly to slowly until reach the temperature of 505.6°C. However, to the stator, the temperature increased slowly before 230 seconds. From *Figure 2.13 and 2.14*, the maximum brake torque is 1750Nm at the speed of 500-700 rpm which satisfy the design requirement and consistence to the mathematical model. A noteworthy phenomenon happened in the test is that the relation between the brake torque and temperature, in *Figure 2.15*, the torque created by brake dropped about 40% when the temperature of rotor plate reached its maximum value on the continuous stage, The working life of the retard will be affected by the temperature raised in the rotor plates and it was adverse and inaccurate for a long time torque measurement. Therefore, in order to guarantee the operation without fluctuation, a strong cooling system is indispensable to reduce the heat generated by the retarder.

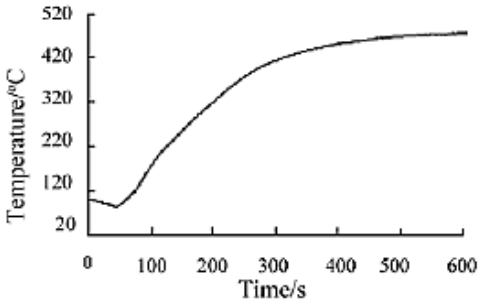

Figure 2.11 Brake torque-temperature of the stator curve eddy current retarder [24]

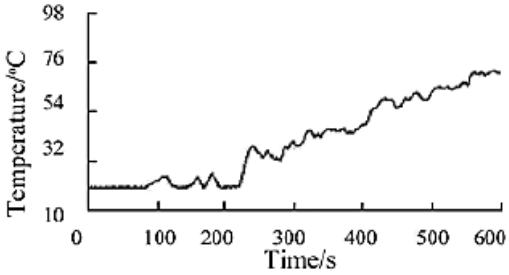

Figure 2.12 Brake torque-temperature of the rotor curve eddy current retarder[24]

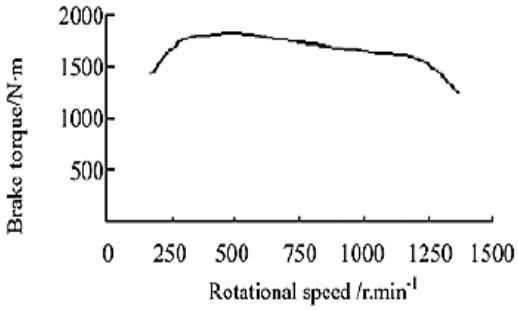

Figure 2.13 Brake torque-rotational speed curve [24]

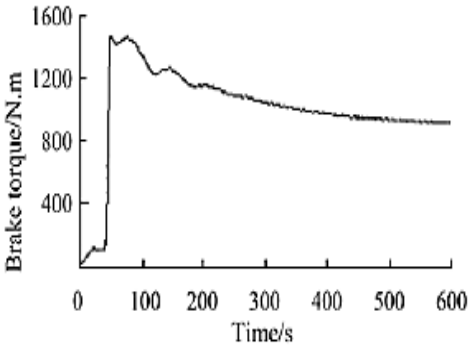

Figure 2.14 Brake torque-time curve [24]

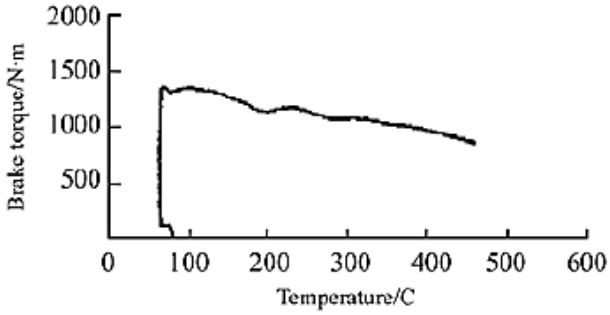

Figure 2.15 Brake torque-Temperature of rotor curve [24]

4. Conclusion

The literature review showed the drawbacks of lead acid battery in terms of power density and operating temperature range. The most possible and revolutionary alternatives is Li-ion battery. Compared to lead acid battery, the specific energy and energy density increased significantly form 40 Wh/kg and 75 Wh/L to 132Wh/Kg and 266 Wh/L, which means Li-ion batteries with one third weight and half volume of lead-acid battery can produce the same amount of energy. The performance improvement is more impressive under a low temperature and large current output situation.

The powertrain design and studies were reviewed as well. For the manual (hand-push) wheelchair, the rim motor is a good choice, not only because of the easily replacement but also due to the comfort and more suitable for outdoor use. The studies proved the optimizing design of the rim motor. On the other hand, small radius hub motor can improve the old gear motor by providing a high efficiency, low weight and low cost of maintenance and can be an alternative motor in electric wheelchairs.

For electric motor itself, the efficiency can also vary due to the design, material or assemble error. Therefore, an accurate dynamometer is indispensable to verify the efficiency of different motor. From the test result published by Liu and Jiang, we know that the dynamometer based on the eddy current has a wide rotational speed range of measurement and its accuracy is insensitive to the change of temperature.

Chapter 3: Installation and Testing of New Battery-Motor System

1. Introduction

In order to increase the operation time and the activity range of electric wheelchairs, reducing weight, improving battery performance and increasing the efficiency of motor are three key factors. A Jazzy 1113 Power Chair [26] used in this study is a representative midsize electric wheelchair which uses two lead-acid batteries and DC motors coupled with a gear reducer system. Lead-acid battery used by Jazzy 113 power chair has a low energy-to-weight ratio, a low energy-to-volume ratio. Limited by the reducing mechanism of gear motors, the Jazzy 1113 power chair has a low efficiency and high cost of maintenance. These two key components are the main hurdles for high-performance wheelchairs because of their heavy weight, poor efficiency, and poor life cycle characteristics. Table 3.1 lists each major component's weight used in this chair. Apparently, the lead-acid battery, in average, contributes up to one third of the total weight and the motor drive system contributes another third. These parts are accounts for 44.7% of the weight of Electric wheelchair. Therefore replacing with high-performance batteries and high- efficiency and low-weight motor as well as quantifying the improvement after replacement is the main task of this study. The studies and results of

the onboard performances of the lead-acid, phosphate-based Li-ion battery, gear motor and hub motor under different loads will be presented in this chapter.

Table 3.1 Weights of existing Jazzy 1113 power chair

	With Gear Motor and Lead-acid Battery		
	Chair (including the supporting arms):		53 lbs.
	Two batteries (33Ah each):	each	26.5 lbs.
	Two motor-reducer systems:	each	17.5 lbs.
	Bottom frame (including rear wheels):		35.5 lbs.
	Two front wheel assemblies:	each	4.5 lbs.
	Foot rest:		6 lbs.
	Controller box:		2 lbs.
	Two plastic frames (including some parts to connecting bottom frame):		3.5 lbs.
	Total weight:		197 lbs.

2. Experimental Aspects

2.1 Testing Stand

To determine the onboard performances battery and motor before and after replacement, we designed and manufactured a fixed wheelchair performance testing stand. In order to collect the battery performance data from a continuous running Electrical Wheelchair we designed a wheel support base with four roller inside *(Figure 3.1)* so that the wheels can keep running on it without making any displacement and with

less frictions. There are two-side support arm for fixing the sensors to monitor the current, voltage and speed.

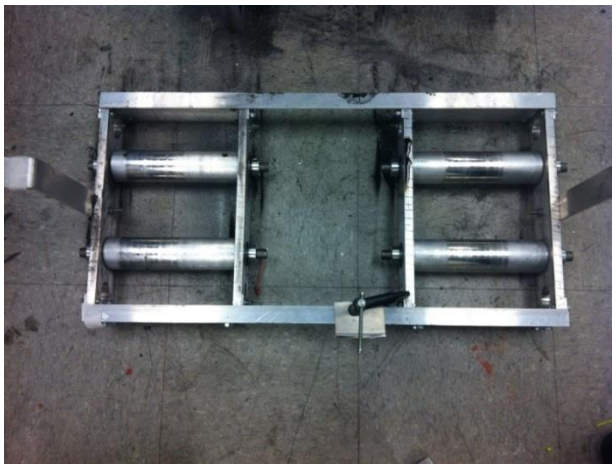

Figure 3.1 Roller support for testing onboard performances of batteries and motors

2.2 Data Collection

We use multifunctional compact monitoring and logging sensors (PowerLog 6S) to collect the voltage, current outputs of the batteries as a function of running time during the test (*Figure 3.2).* The sensors are connected with batteries and motors in series in the circuit. There is a test condition difference need to be noticed, because of the original design of the Electrical wheelchair Jazzy 1113. It uses two 12V batteries to power two geared motors respectively, so we use two sensors in the circuit to record the data respectively.

Figure 3.2 PowerLog 6s sensors for data logging

2.3 Batteries Testing

Table 3.2 Specification of each battery in the battery test

Abbreviation	Battery type	Capacity	Battery Name	Vendor Name
Li 50	Lithium-ion	50Ah	LiFePO4 12V	OPTIMUM BATTERY
Pb 50	Lead acid	50Ah	UB12500	UNIVERSAL BATTERY
Pb 35	Lead acid	35Ah	12V35AhU1(MF)	UNIVERSAL POWER

We used a drivetrain of a Jazzy 1113 Power Chair to compare the performance of 35Ah lead-acid batteries, 50Ah lead-acid batteries, and 50Ah Li-ion batteries. *Table 3.2* listed the specification of the three kinds of batteries we used in this study.

Figure 3.3 shows the testing setup where electric wheel chair has no extra load. Roller base testing stand is to support and keep the electric wheelchair in position while it is running during the test period. Powerlog is fixed on the arm of the testing stand for

recording the operating voltage, current and capacity. It is worth to mention that the first set of test is under "outermost case" in order to obtain the maximum performance of each kind of battery on the drivetrain with the traditional DC motor and gear reducer system. The outmost test means that we removed the seat and frame and located the batteries outside of the wheelchair to reduce the weight as many as possible. During the discharge testing, the joystick was fixed on the fastest speed setting. Voltage and current data were collected simultaneously with the help of the Powerlog sensors. After full discharge, the batteries are charged with the integrated charger and a standard 120-V outlet.

Figure 3.3 Images of the testing setup under no load case (left) and key component related to the test (right).

2.3.1 Battery Testing Under Different Loads

In addition, we made another series battery test to simulate practical power consumption of the electric wheelchair at the maximum speed. *Figure 3.4* shows the different battery test loading cases in the battery performance test. The first case is no load on the seat for reference. The second one is that we placed two barbells (each barbell weighs 45 pounds) on the seat to simulate a small child. The third case is to place four

barbells on the seat to simulate an average adult and the last one is to place six barbells on the seat to simulate an overweight adult.

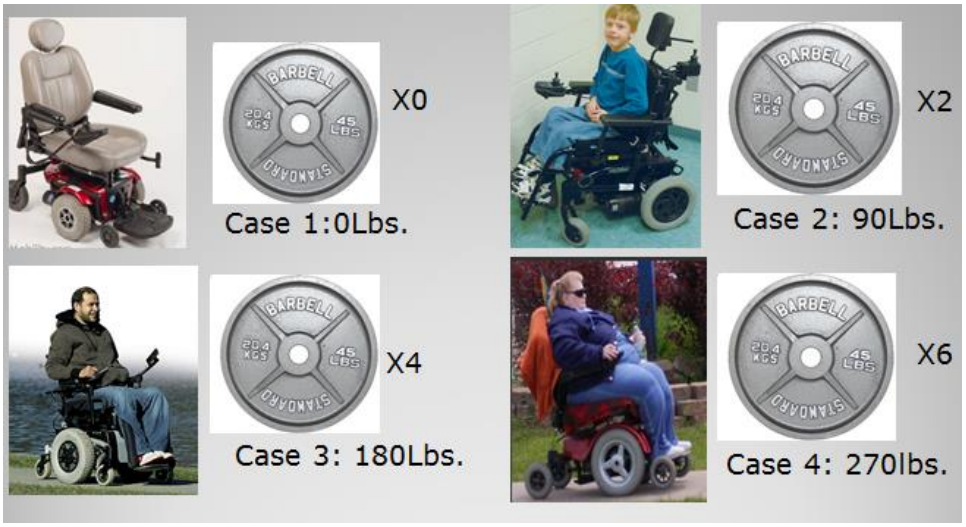

Figure 3.4 The four cases in the battery test, each case used the barbells as weight for simulating different usage condition

2.3.2 Li-ion Battery Charge under Different Currents

Moreover, to examine the battery charge rate capability and temperature variation, we have designed the third set of experiments. The batteries were charged using a 500 watt DC power supply and current was set constant in the range of 2A to 11A. Same as before, the current, voltage and capacity were recorded with Powerlog sensors. Meanwhile, the temperature change under different charge current is measured. A thermistor was attached to the top surface of batteries. The battery was placed in a by a thermal-insulating foam container to prevent the heat transfer with the ambient *(see Figure 3.5)*. Powerlog sensor was also used to record the temperature change of the batteries.

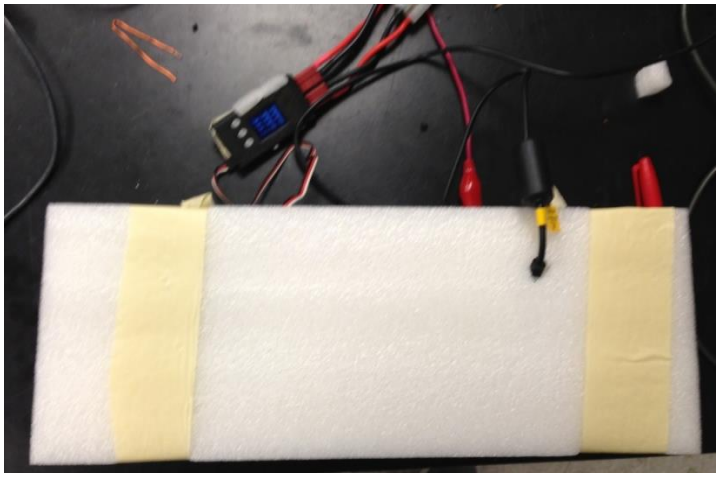

Figure 3.5 Different current battery charge conditions, the batteries were put inside of the foam container for insulate the ambient temperature

3. Results and Discussion

Figures 3.6, 3.7, and 3.8 show the battery performances of the three batteries, i.e. 35Ah lead-acid *(Pb 35),* 50Ah lead-acid *(Pb 50),* and 50Ah $LiFePO_4$ lithium-ion (*Li 50)* batteries tested under the outmost condition. *Figure 3.6 is* the curves of voltage and current as a function of time during the discharge. *Figure 3.7* is the charge curves of voltage and current as a function of time. *Fig 3.8 (a) and (b)* shows the discharge and capacity as a function of time revealing times needed for full discharge and charges of three batteries through a standard 120-V outlet .

As can be seen in Figure 3.6, the 50Ah Li-ion battery ran relatively uniformly at an operating voltage of 13V for 11 hours, whereas the 35Ah and 50Ah lead acid batteries demonstrated a steady decrease in voltage over time and was depleted at 5.5 hours and 8 hours, respectively. The discharge currents at the operating conditions are 5A for Li ion battery. 5.3A and 5.8A on average for 35Ah and 50Ah lead acid battery respectively. These results indicate that for the same capacity level, Li-ion batteries ran 3 hours longer

than lead acid batteries. The reason for this operating time difference can be attributed to voltage output difference between these two kinds of battery. Due to the faster voltage decrease speed of lead acid battery, in order to provide the same amount of power, the controller has to withdraw a higher current which consumed more capacity.

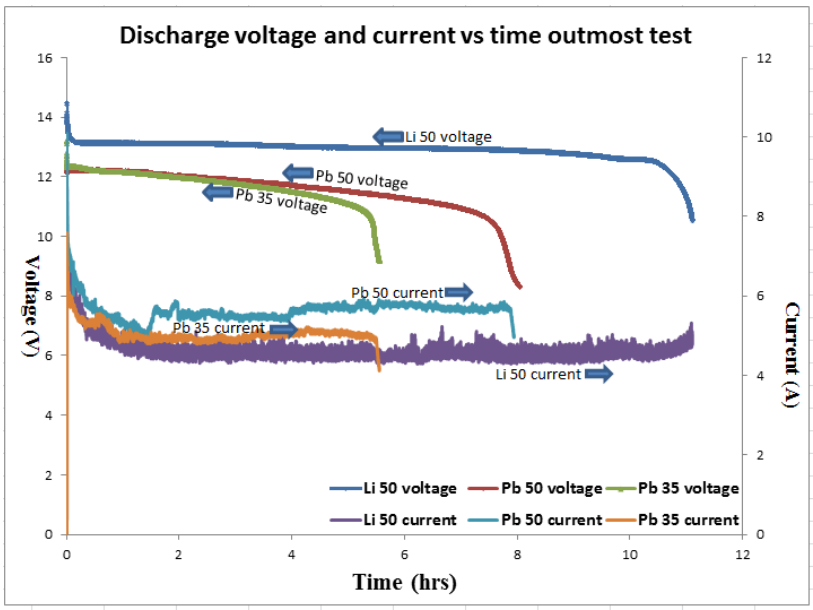

Figure 3.6 Battery discharge profiles, i.e. voltage and current as a function of time, under the outmost test condition.

From *Figure 3.7,* it can be seen that the charge voltage ran uniformly at 11.5 V and the charge current operating at 11A until to fully charge for Li-ion battery. For lead acid battery, the charge voltage increase slowly from 10V to 12.5 V and the charge current remains constantly at 3 A which is much smaller than that of Li-ion battery. It is apparent that Li-ion battery can be charged at the high current (about 4 times higher than lead acid battery), rendering the capability of fast charging. Li-ion 50Ah battery only needs 5.5 hours to be fully charged, but to fully charge the 35Ah lead acid battery needs 7.5 hours and the 50Ah need 15 hours which is 3 times longer than the same capacity Li ion battery. Further the voltage of 35Ah lead acid battery is higher than 50 Ah lead acid battery,

although their charging current is the same. This indicates that a high internal resistance exists in the 35Ah lead acid battery.

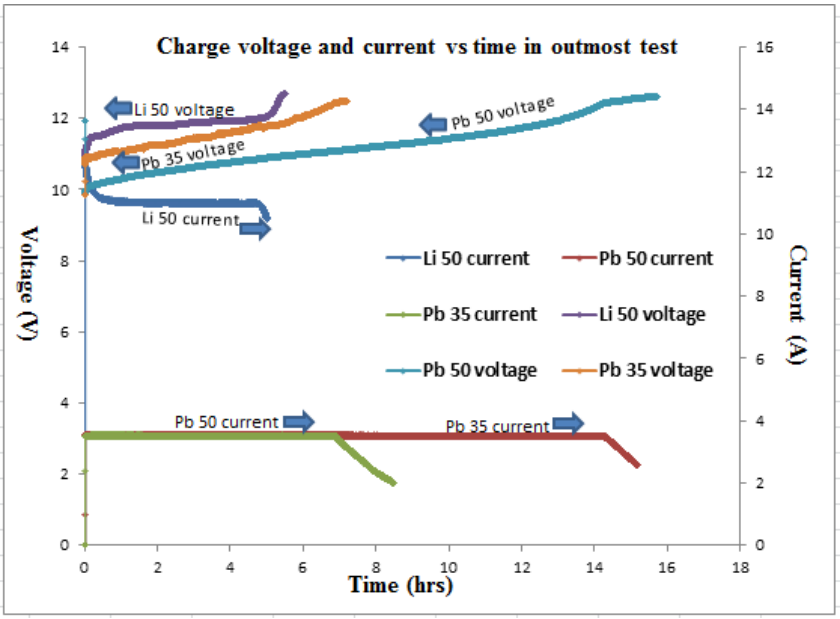

Fig 3.7 Profiles of voltage and current as a function of time of the three different batteries during charging under the outmost test condition.

Figure 3.8(a) shows the discharge capacity as a function of time. The discharge capacity increases linearly with the operating time until the controller stops the circuit when no enough power can be delivered from the battery. The Li-ion battery was able to withdraw all of its capacity 50Ah during the discharge and keep the wheelchair running continuously at the maximum speed for 11 hours. For lead acid battery, the running time of 50Ah is 8.5 hours and 6.5 hours for 35Ah. Compared to Li-ion battery, lead acid batteries can only deliver 45Ah and 30Ah, about 90% of their full capacity at maximum speed. *Figure 3.8(b)* shows the charge capacity as a function of time of these three batteries. The rising slop of Li ion battery is much higher than lead acid battery due to its ability of large input charge current shown in figure 3.6. And again, the Li-ion batteries outperformed the lead-acid batteries, reaching full charge in much short time (5 hours).

Compared to the same 50Ah capacity lead acid battery, the charge time saving is about 10 hours by replacing with Li-ion batteries.

(a)

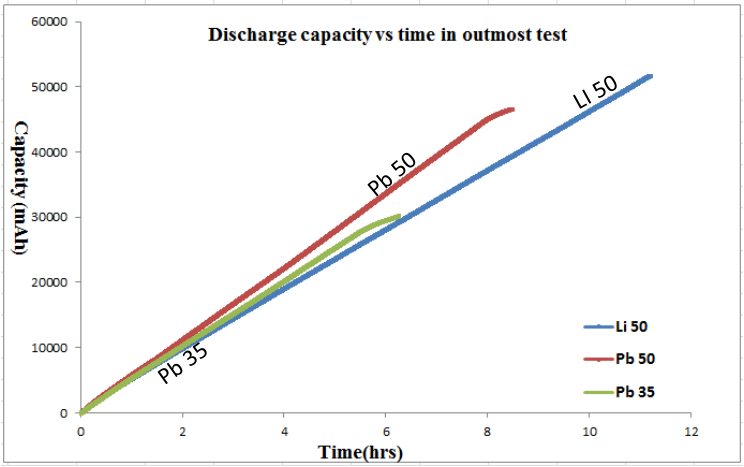

(b)

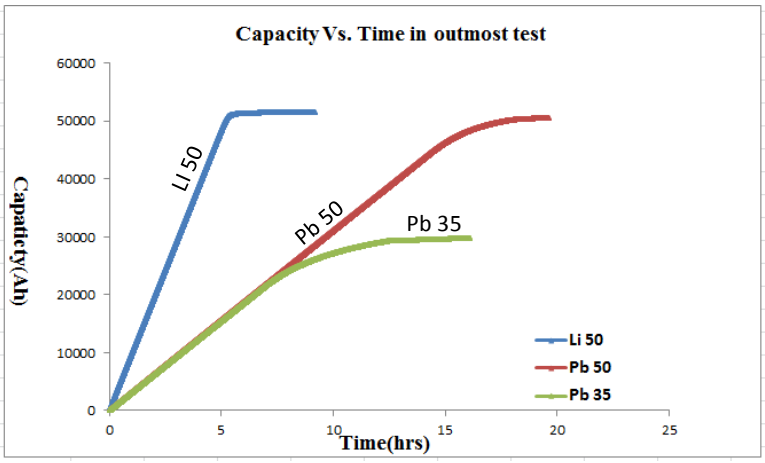

Figure 3.8 (a) Battery discharge capacity as a function of time profiles under outmost test condition; (b) Battery charge capacity as a function of time under charging condition preset by each 120V battery recharger

Figure 3.9 further shows the charge capacity of the Li-ion battery under the charge current varying from 2A to 11A. From the figure we can see that the capacity as a function of time under the constant current charging mode can be described as

$$C = I * t + b$$

where C is capacity, I is input current, t is the time and b is the energy consumed by the internal resistance. Because slope of the curves is equal to I, a larger input current corresponds a higher slope and faster speed to fully charge. Although, all of the charge current can reach full capacity, the charge time needed is much different. For example, at the charge current of 3A which is the normal charge current of lead acid battery, it will need 15 hours to be fully charged. However, at 11A charge current which is the normal charge current of Li-ion battery, the time needed to fully charge is only about 5 hours.

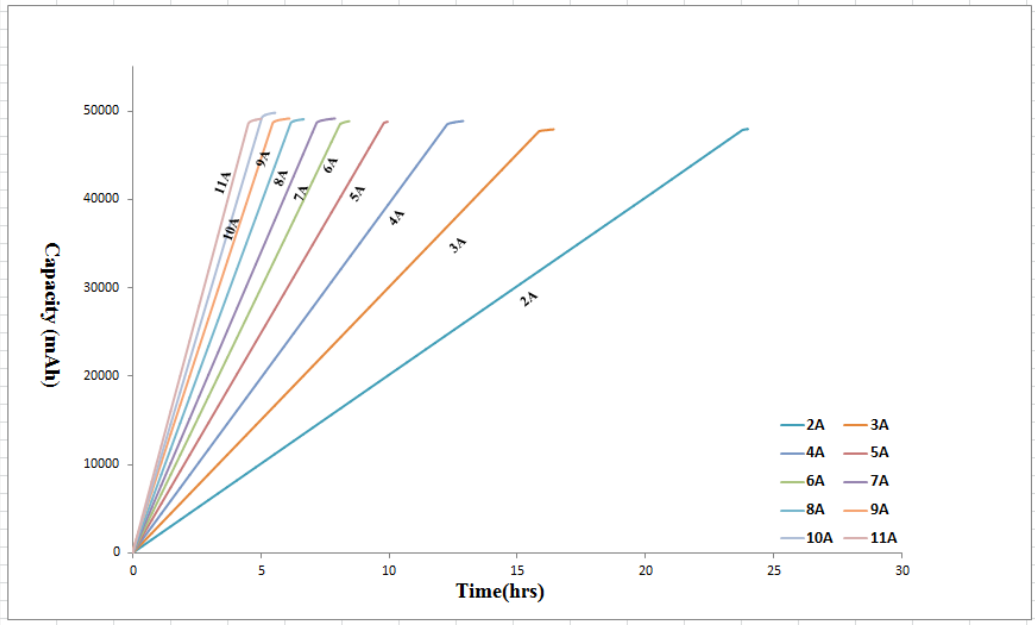

Figure 3.9 The charge capacity as a function of time of the 50Ah Li-ion batteries under the constant charge current varying from 2A to 11A

Figure 3.10 shows the advantage of Li-ion battery in temperature rise compare to lead acid battery. For Li-ion battery, the maximum temperature rise is 26^{o}C at 9A, however, for lead-acid battery the maximum temperature is 38^{o}C at 5A. Since the temperature was measured on the s of the battery, we speculate that the core temperature could be near or over 50^{o}C, which will reduce the life cycle or even cause the leaking problem for lead

acid battery. Therefore, compared to lead acid battery, Li-ion battery can be charged by a high current without high temperature rise, which means a great advantage of saving the time of recharge.

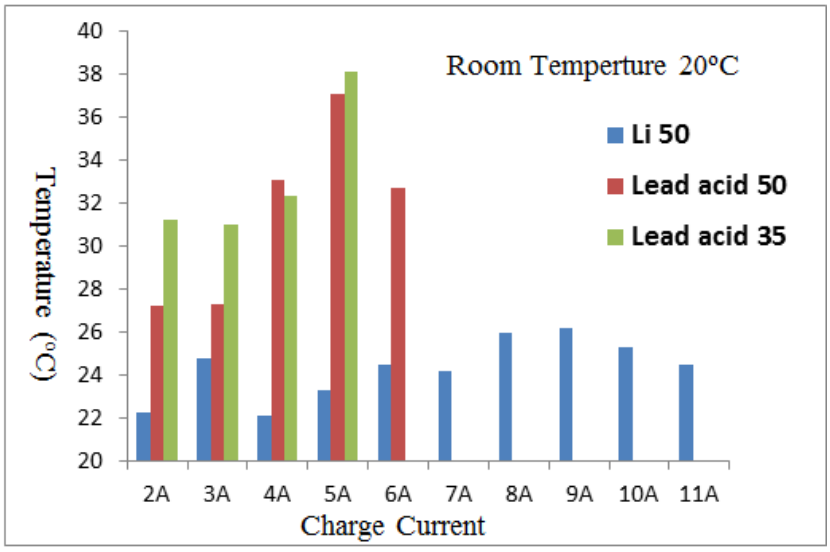

Figure 3.10 Temperature change under different charge current of the three different types of batteries

The performances (voltage and current as a function of time) of the three batteries operating under the four loading cases are shown below from *Figure 3.11* to *Figure 3.14*. The yielding point at the end of the curve means the battery cannot maintain the voltage which is required by the motor. Therefore, the controller cuts off the circuit. We consider this point is the maximum running time of the batteries.

From the figures below we can see the maximum running times of Li-ion batteries at the four loading cases, i.e. no loading, 90lbs. loading, 180lbs. loading, 270lbs. loading, running time is 7.7 hours, 7.5 hours 6.6 hours and 5.4 hours respectively. While the maximum running times of 50Ah lead acid battery at the four loading cases is 7.4 hours, 6.1 hours 5.1 hours and 3.8 hours respectively. Apparently, the maximum running time

increased from 1 hours to 2.5 hours when the load vary from no load to 270lbs. by replacing 50Ah lead acid battery with 50Ah Li-ion battery. In addition, compare *case4* to *case1*, the lead acid battery reduced 54.7% of running time however, Li-ion battery only reduced 9.5% of running time.

(a)

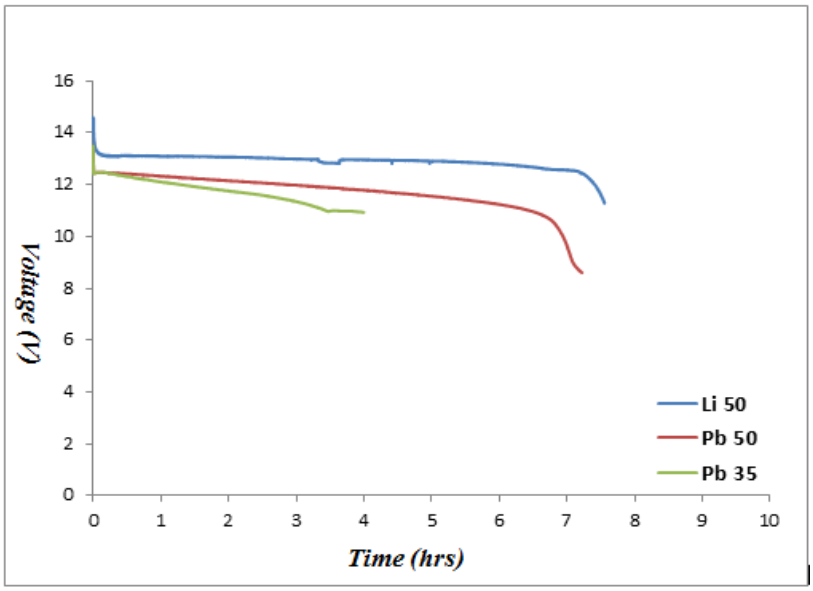

(b)

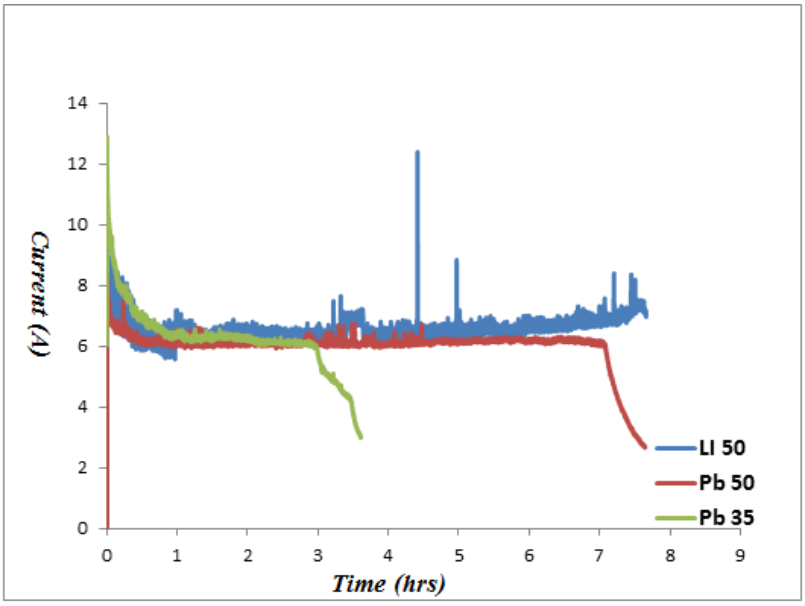

Figure 3.11Battery performance test of three kinds of battery Case1 no loading (a) Voltage as a function of time (b) Current as a function of time

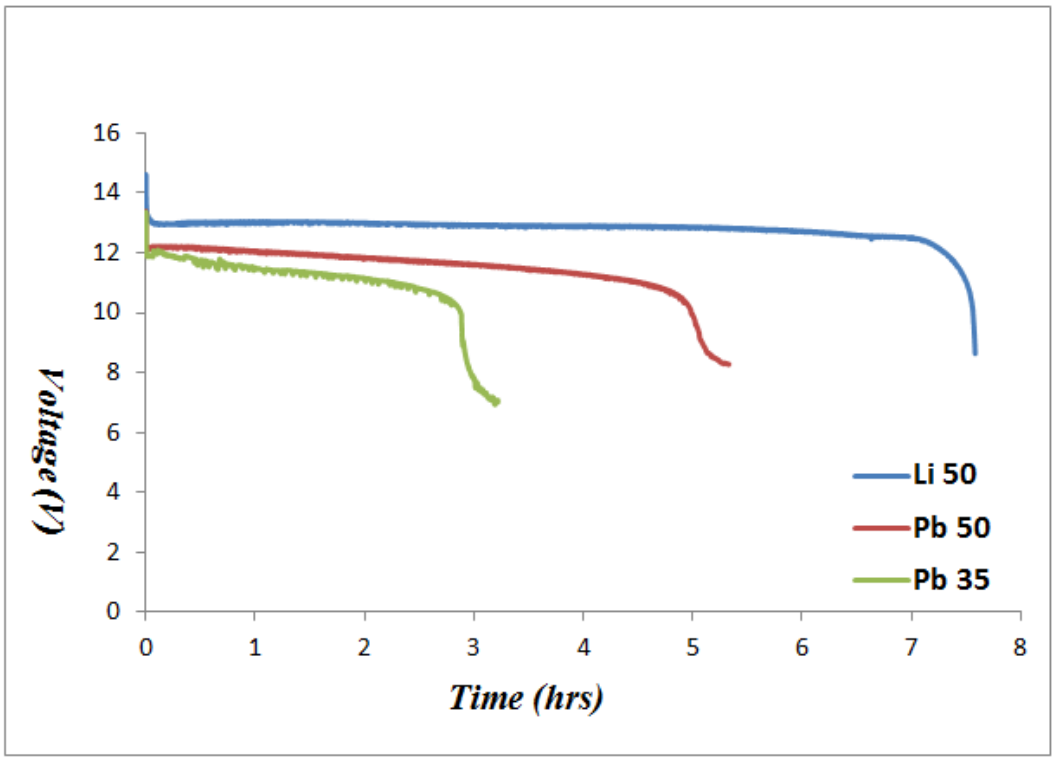

(a)

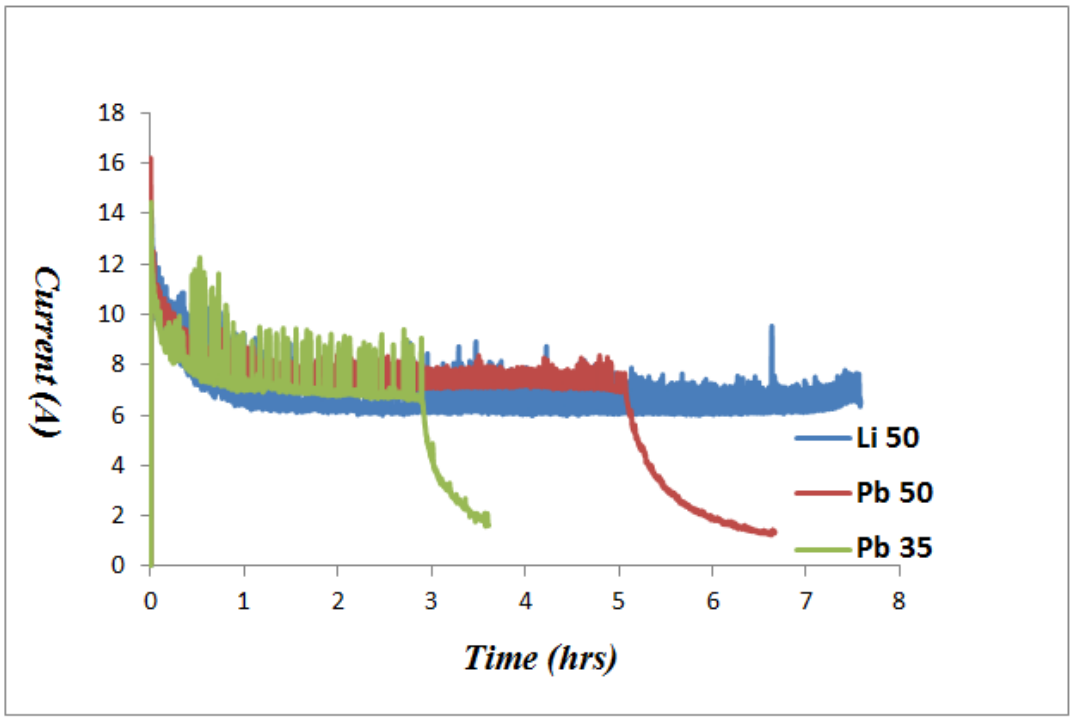

(a)

Figure 3.12 Battery performance test of three kinds of battery Case2 90lbs. loading (a) Voltage as a function of time and (b) Current as a function of time

(a)

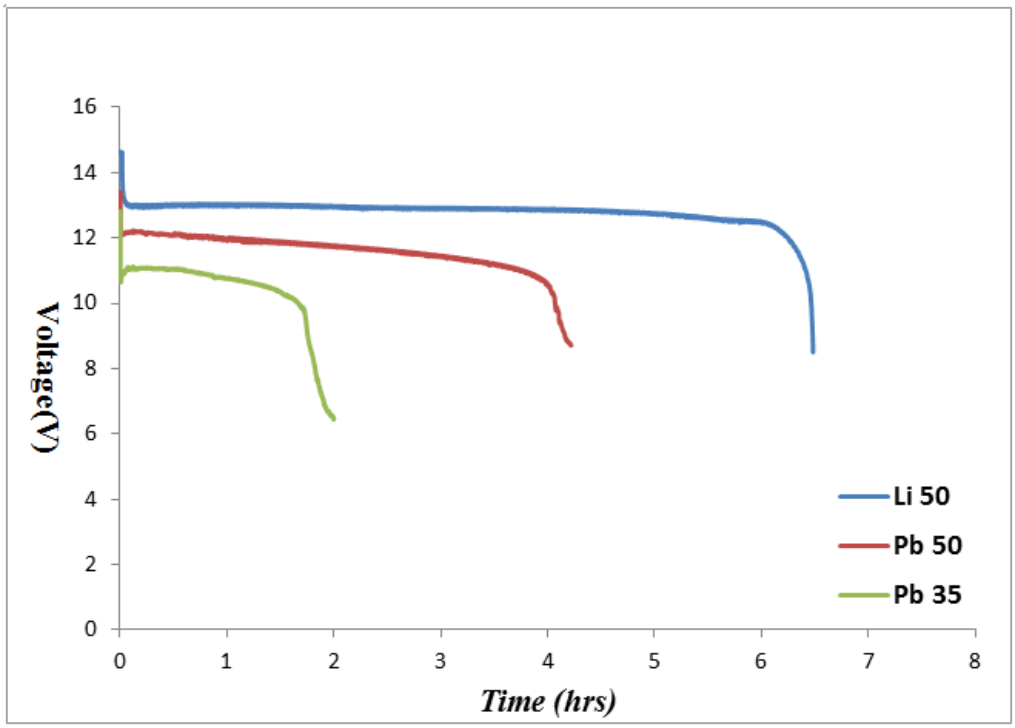

(b)

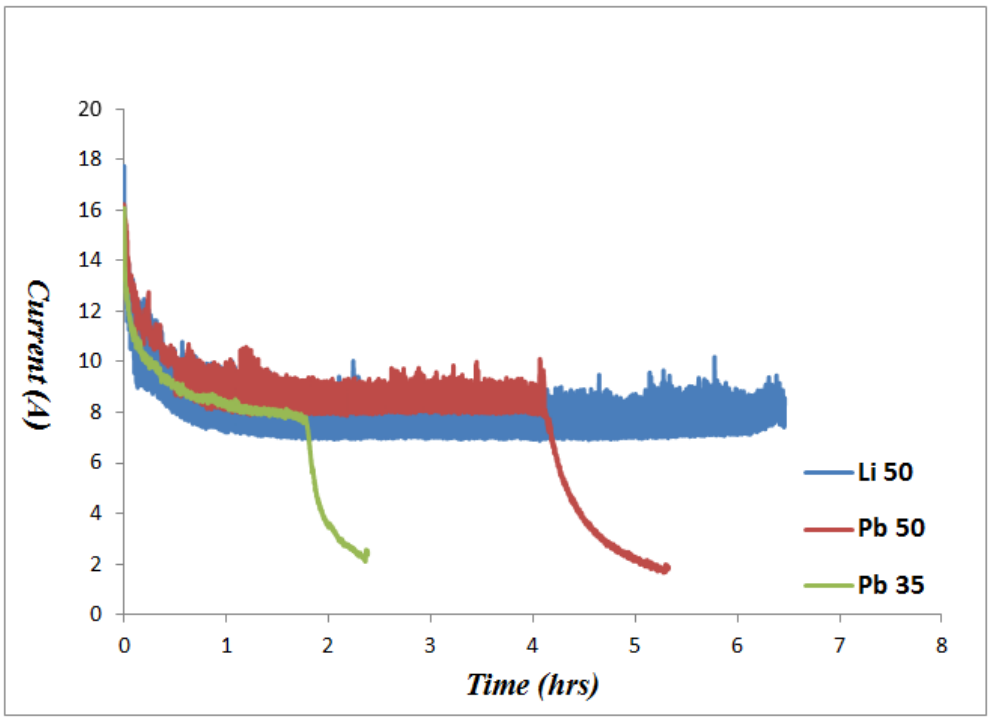

Figure 3.13 Battery performance test of three kinds of battery Case3 180lbs. loading (a) Voltage as a function of time and (b) Current as a function of time

(a)

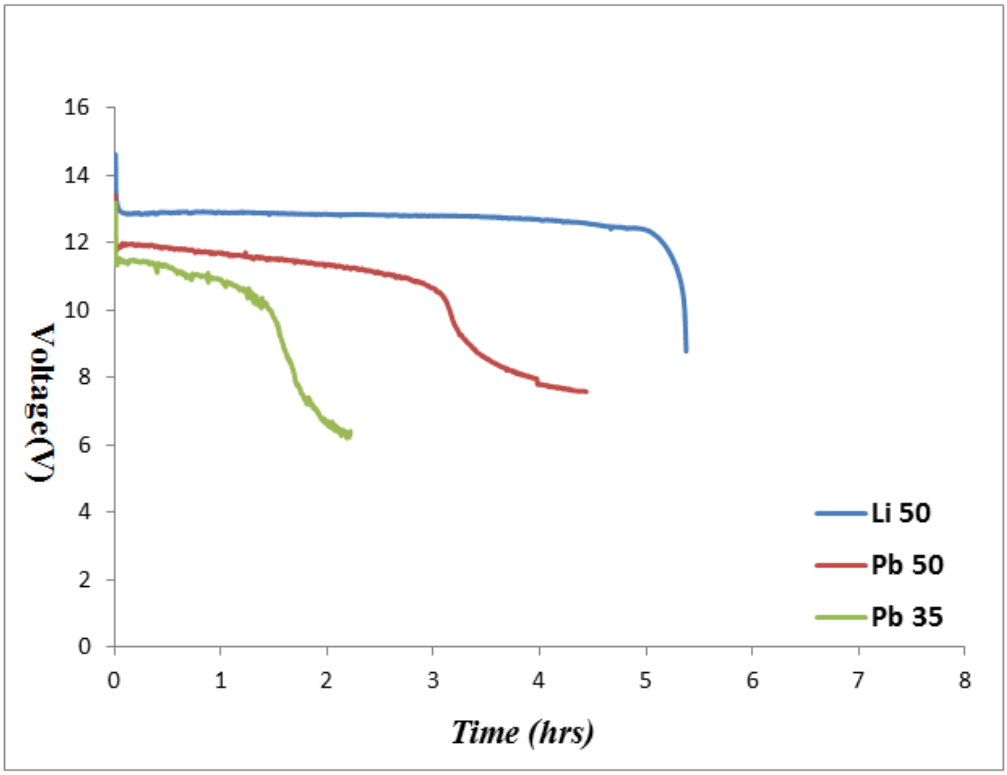

(b)

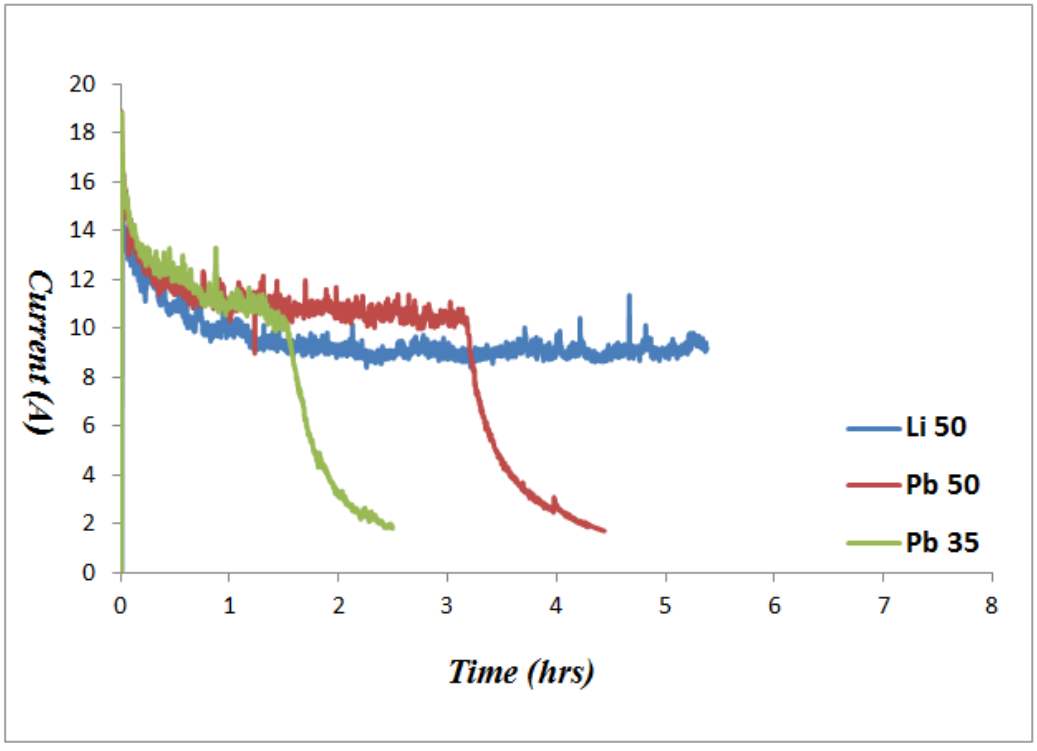

Figure 3.14 Battery performance test of three kinds of battery Case4 270lbs. loading(a) Voltage as a function of time and (b) Current as a function of time

4. Motor Replacement

4.1 Introduction

In this section, the main goal is to reduce the energy consumption from the motor system to save energy and increase the running time at the same time. As discussed in chapter 1, hub motor shows advantages over the ordinary geared motor in many aspects such as light weight, low maintenance cost, and high efficiency etc. Therefore in our design we select a pair of 24V 180W hub motor to replace the original geared motor in our prototype wheelchair. Further we determine the maximum running times before and after replacing the gear motor with hub motors powered by either 50Ah lead acid batteries or 50Ah Li-ion batteries in the same way described in the previous sessions. Prior to the performance test, we have designed and conducted strength analysis of connecting parts which are used to assemble the hub motor on the frame.

4.2 Connecting Parts Design and Strength Analysis

In order to install the hub motors on the Electrical Wheelchair Jazzy 1113 Power Chair， we designed connecting parts to replace the original gear motor, which is shown in *Figure 3.15*. The connecting parts are consisted of four individual parts; two L shaped channels on each side are used to connect the frame of Jazzy 1113 Power Chair by four of 1/4in bolts, and a 0.75in thick aluminum plate is the main part to connect the axle of hub motor with an 18mmdiameter hole and 4mm×4mm keyway. Three 1/4”-28 bolts are arranged as a triangle position on the surface of L shaped channel to hold all parts

together and against the torque from the hub motor. *Figure 3.16* shows how we used the connecting parts to install the hub motors to the frame of electric wheelchair.

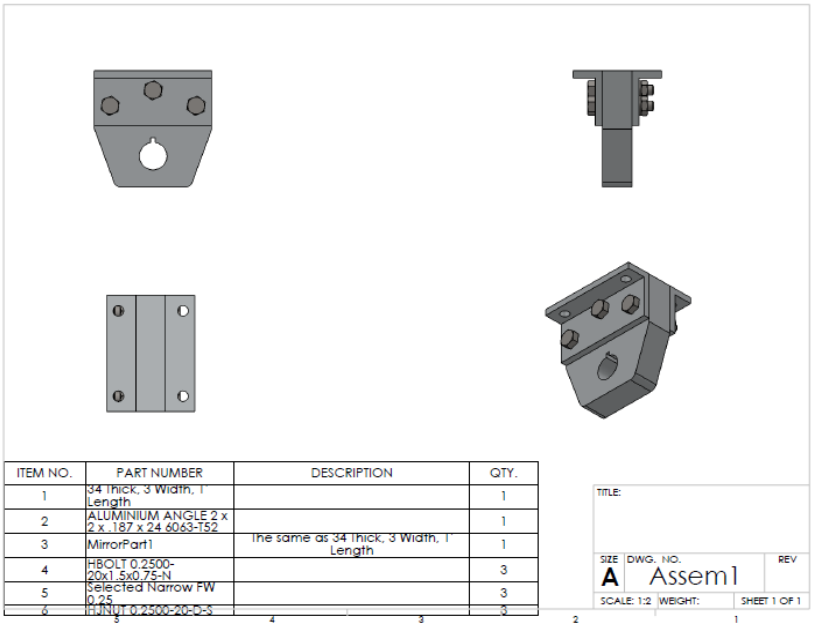

Figure 3.15 Modeling designed in Solidworks of the connection component for hub motor

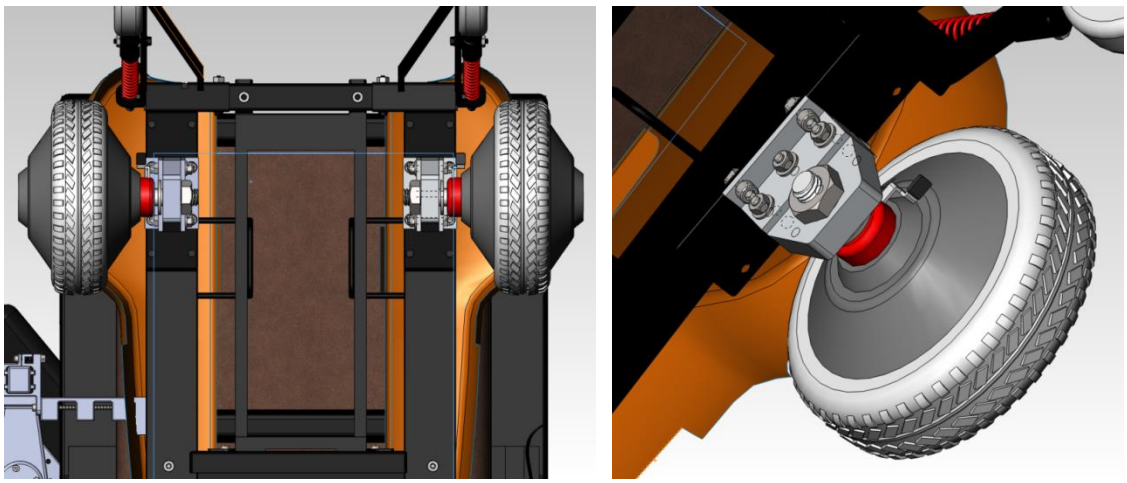

Figure 3.16 The final assembly of hub motors to the electric wheelchair with the help of the connecting parts. The left is the overview and the right is enlarged view of the connecting parts

We made a static analysis in solidworks to simulate the motor test condition in order to examine the mechanism can stand the torque from the hub motor. In the setting part of simulation, we calculate the maximum torque from :

$$P = \frac{rpm \times T \times 2\pi}{60}$$

The power of the hub motor is 180W and we want to verify the mechanism can stand the maximum stress, so we defined the RPM in the low speed position on the controller to get the lowest RPM at 30.

So my input Torque equal to:

$$T = \frac{180 \times 60}{2\pi \times 30} = 57.69\text{Nm}$$

We use Direct Sparse solver in Solidworks simulation because this solver is more efficient than the FFEPlus when the simulation has more contacts and bolt connectors.

Because of we need to define the connection type as bolt so we need to determine the preload and Friction factor (K).

The preload can be found in the equation:

$$T = K * F_i * d \text{ [27]}$$

$$F_i = 0.75 * A_t * S_p \textit{(For Reusable connections)}$$

$$F_i = 0.9 * A_t * S_p \textit{(For Permanent connections)}$$

Where,

Fi= bolt preload (lbf);

T=bolt installation torque (ft-lb);

K=torque coefficient;

At=Tensile Stress Area (in^2);

Sp=Proof Strength of bolt (Psi);

d=bolt nominal diameter (in);

And A_t can be found from:

$$A_t = 0.7854 * (D - \frac{0.9743}{n})^2$$

Where,

D=Basic major diameter;

n=Number of threads per inch;

If proof strength is not known, a rough approximation can be made using Sp = 0.85*Sy where Sy is Yield strength of material.

Figure 3.17 describes the convergence plot of the process calculation within all studies. For helping the engineer visualize how the solution is converged, a plot of convergence are continuous being updated by each iterative. The solver parameters are used for controlling the calculate speed or result accuracy by changing the preset values or the Maximum number of iterations (P1) and Stopping threshold (P2). For increasing the accuracy of the simulation, one way is to decrease the stopping threshold value. For

increasing the calculation speed the way is to increase the stopping threshold value or decreasing the maximum number of iterations.

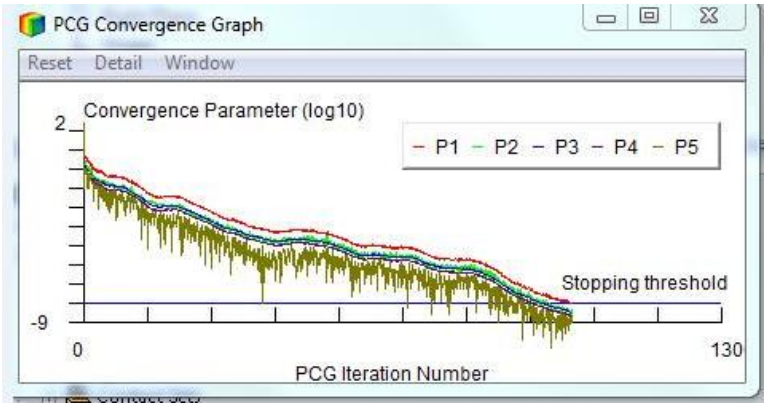

Figure 3.17 Convergence process during the iterations in the simulation of connection components showing the first five parameters where P1 (red) represents Maximum number of iterations and P2 (green) represents Stopping threshold

Table 3.3 Mesh information and details of the connecting components

Mesh Information

Mesh type	Solid Mesh
Mesher Used:	Standard mesh
Automatic Transition:	Off
Include Mesh Auto Loops:	Off
Jacobian points	4 Points
Element Size	0.205554 in
Tolerance	0.0102777 in
Mesh Quality	High
Remesh failed parts with incompatible mesh	On

Mesh Information - Details

Total Nodes	22893
Total Elements	12718
Maximum Aspect Ratio	38.253
% of elements with Aspect Ratio < 3	89.6
% of elements with Aspect Ratio > 10	0.157
% of distorted elements(Jacobian)	0
Time to complete mesh(hh;mm;ss):	00:00:07
Computer name:	R152B-24-087

Table 3.3 shows the mesh information and details, the 4 points Jacobin points were selected due to the uniform geometry of the study parts and the element size and

tolerance were automatic generated according to the shape of the components. There are 22893 nodes and 12718 elements in this study case and.

Figure 3.18 shows how we set up the boundary condition, the green arrow is fixture. The blue arrow defined the bolt connection and red arrow is indicated the location of torque added to the part. After the mesh and set up the boundary condition, contact type and load force. We got the result which show in the *Figure 3.19(a)* to *Figure 3.189(c)* below.

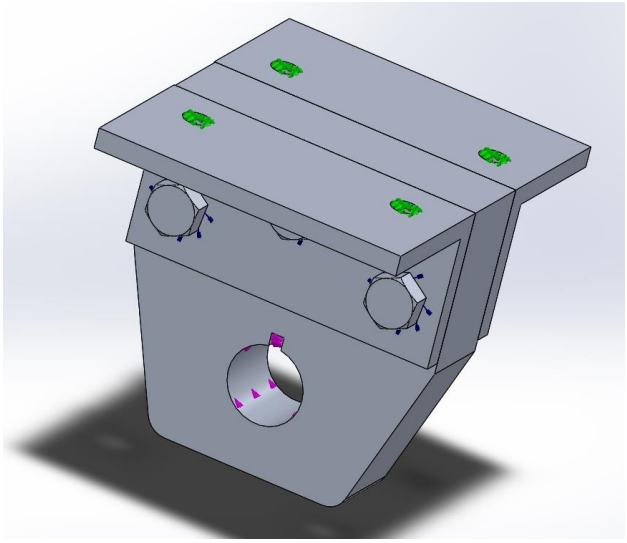

Figure 3.18 Boundary condition set up for connecting part static analysis

(a)

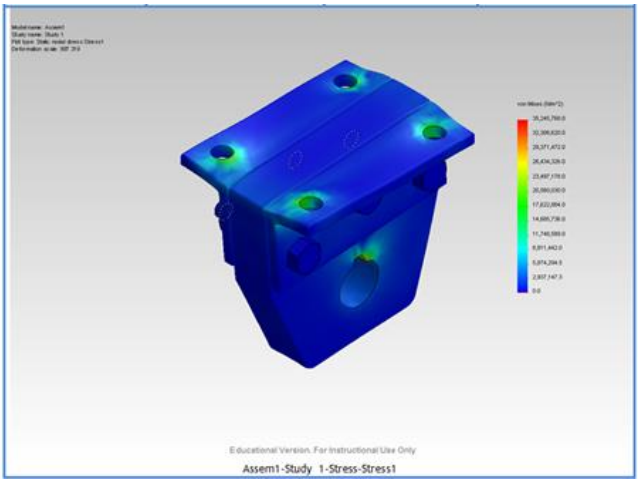

(b)

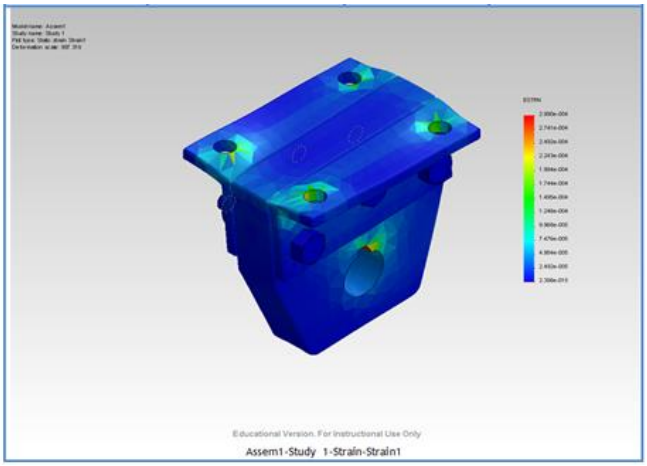

(c)

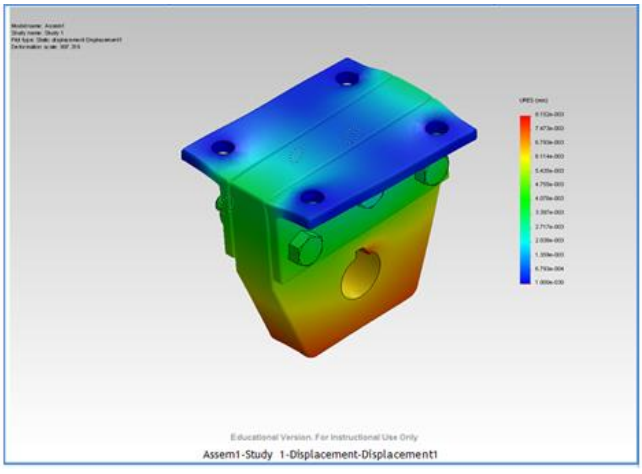

Figure 3.19 The simulation results showing the distribution (a) stress (b) strain and (c) displacement of the connecting components for the hub motor to the frame of electric wheelchair

In summary, From *Figure (a)* the maximum stress is 3.52e7 N/m^2 at Node: 4439 less than 4.0e $8N/m^2$ which is the yield stress of aluminum, from *Figure (b)* and *(c)* we can see all the deform happened around the boundary constrains but the maximum strain is 0.00114858 at Element: 4068 and the maximum displacement is 0.0543345 mm, which are all proved that the connecting part is able to stand with the torque from the hub motor.

5. Hub Motor Test and Result Analysis

The test stand almost the same as the one we build for battery test but due to the operate voltage of hub motor is 24V, we have to connect two 12V batteries in series to support it. The Circuit diagram of gear motor and hub motor are showing below in *Figure 3.20(a)* and *Figure 3.20 (b)*.

From *Figure 3.21* and *Figure 3.25* we can see the comparison of test result between voltage and current under four same test load condition, 12V 50Ah Lead-acid and 12V 50Ah LiFEPO4 lithium-ions (Li-ion vendor) were the two batteries used in the test for representing the performance of hub motor and gear motor under these two kinds of battery material.

(a)

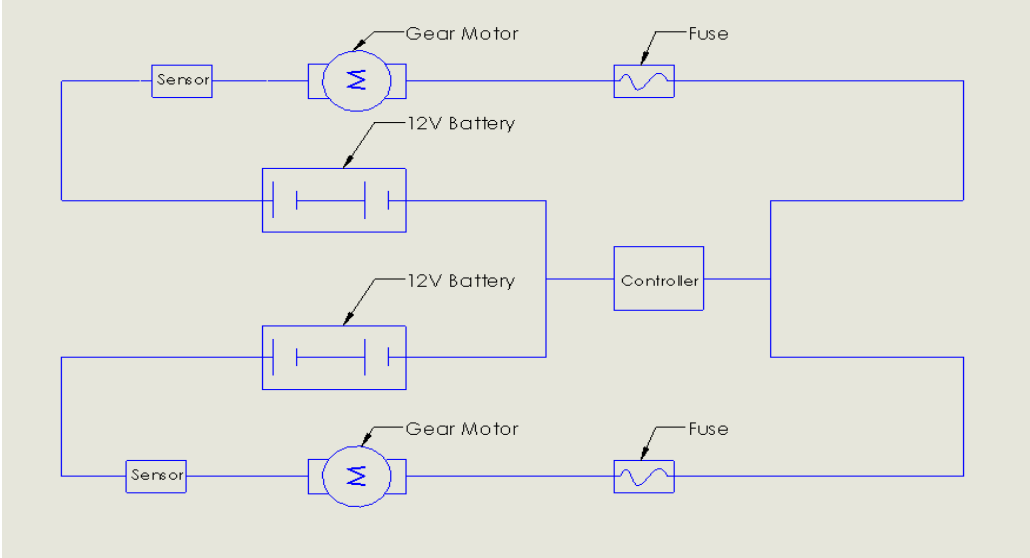

(b)

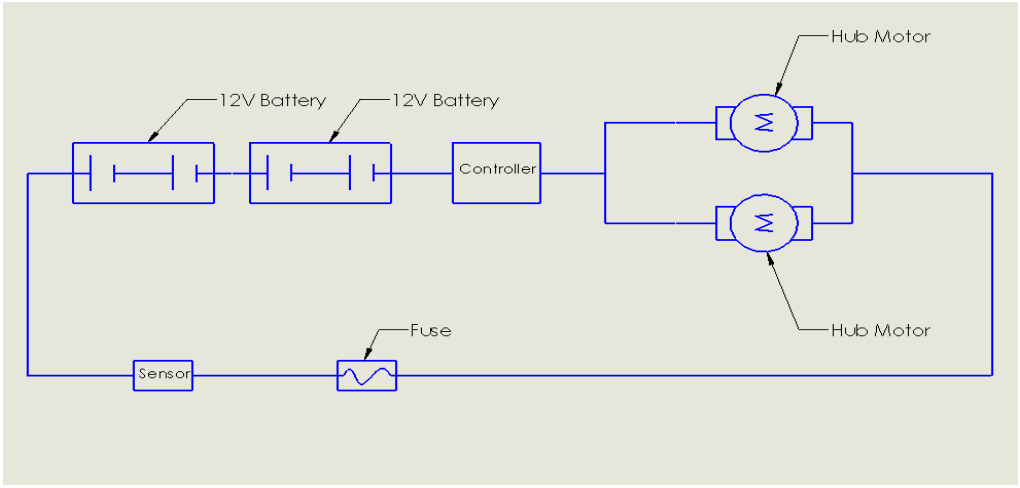

Figure 3.20 (a) Circuit diagram of gear motor and (b) Circuit diagram of hub motor

(a)

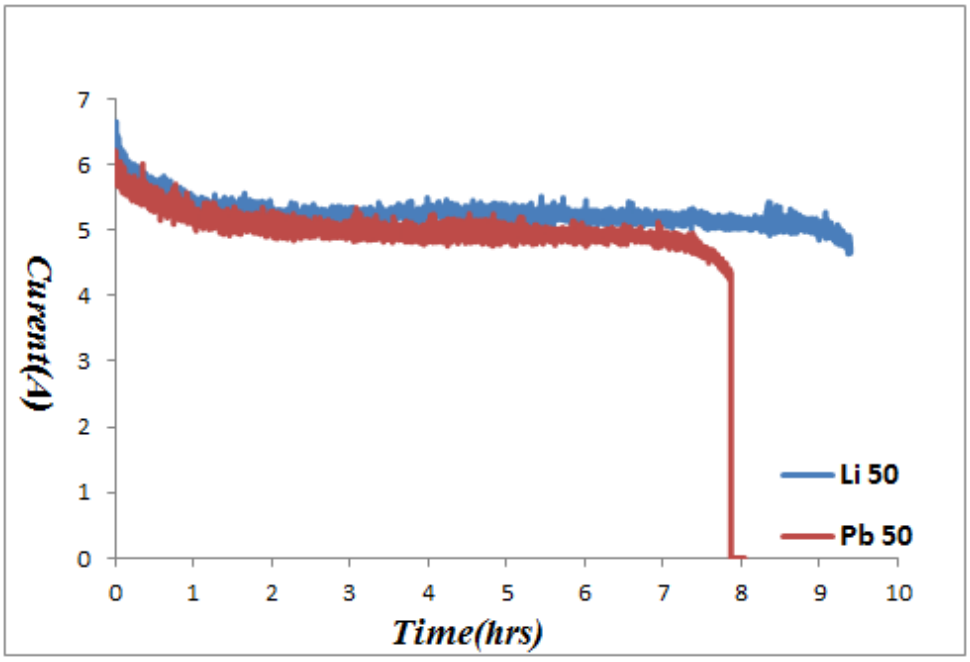

(b)

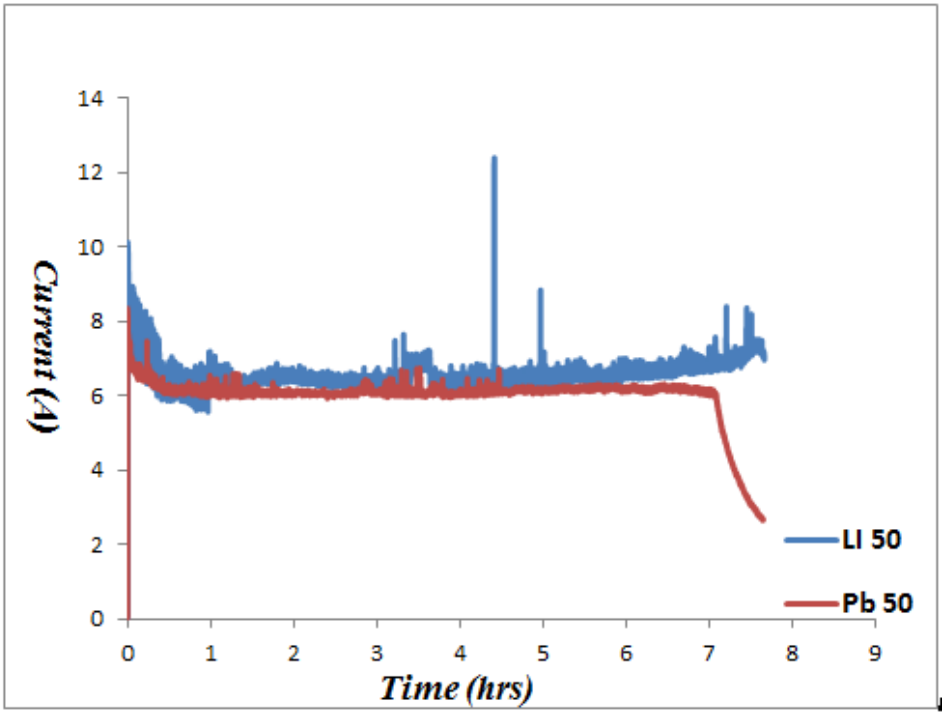

Figure 3.21 Motor performance test of hub and gear motor under the condition of case1 no load (a) Operating voltage and current as a function of time for hub motor and (b) Operating voltage and current as a function of time for gear motor

(a)

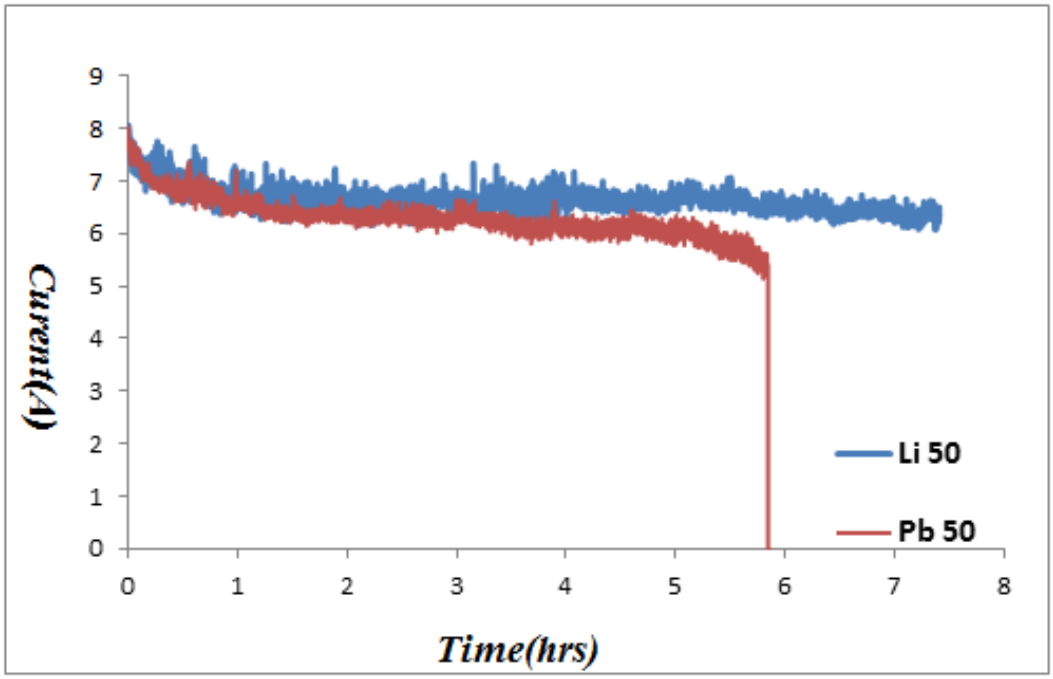

(b)

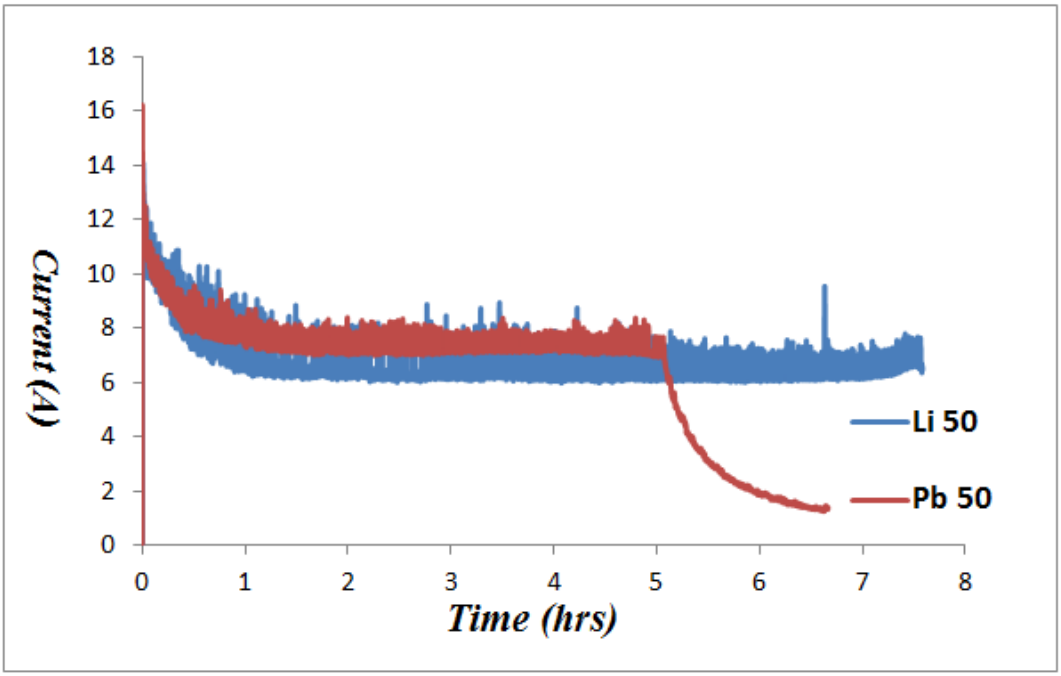

Figure 3.22 Motor performance test of hub and gear motor under the condition of case2 90lbs. (a) Operating voltage and current as a function of time for hub motor and (b) Operating voltage and current as a function of time for gear motor

(a)

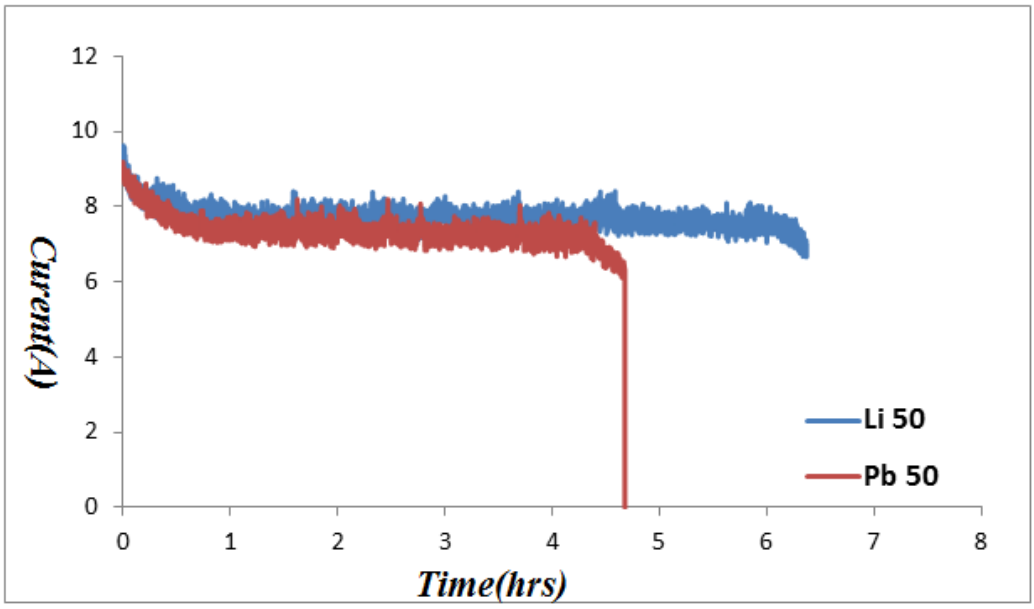

(b)

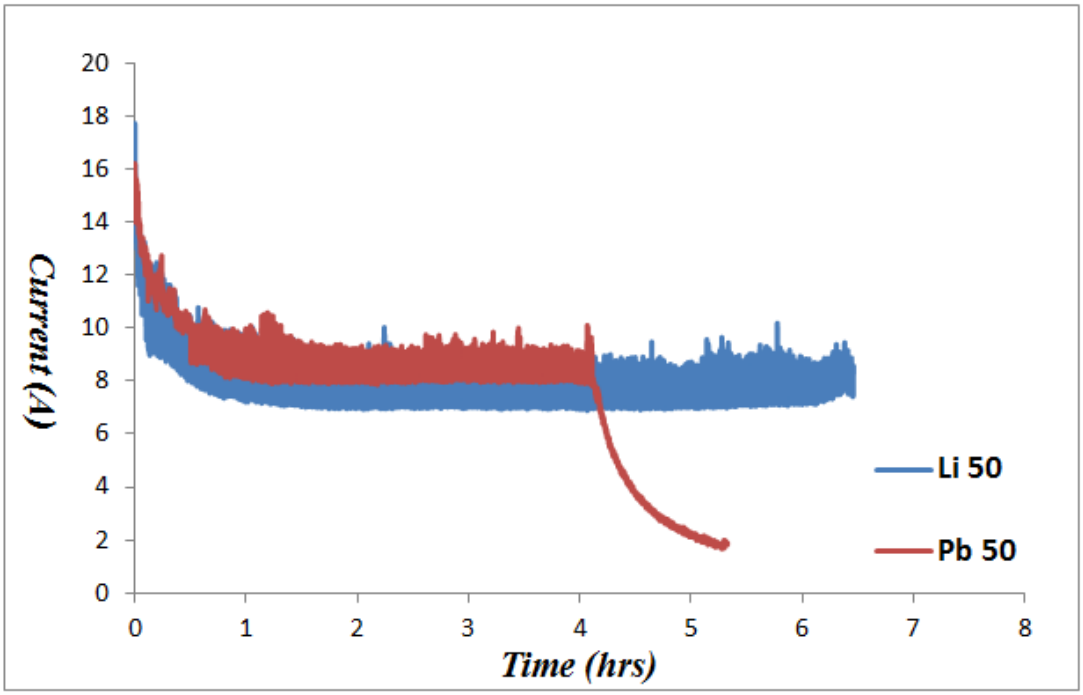

Figure 3.23 Motor performance test of hub and gear motor under the condition of case3 180lbs. (a) Operating voltage and current as a function of time for hub motor and (b) Operating voltage and current as a function of time for gear motor

(a)

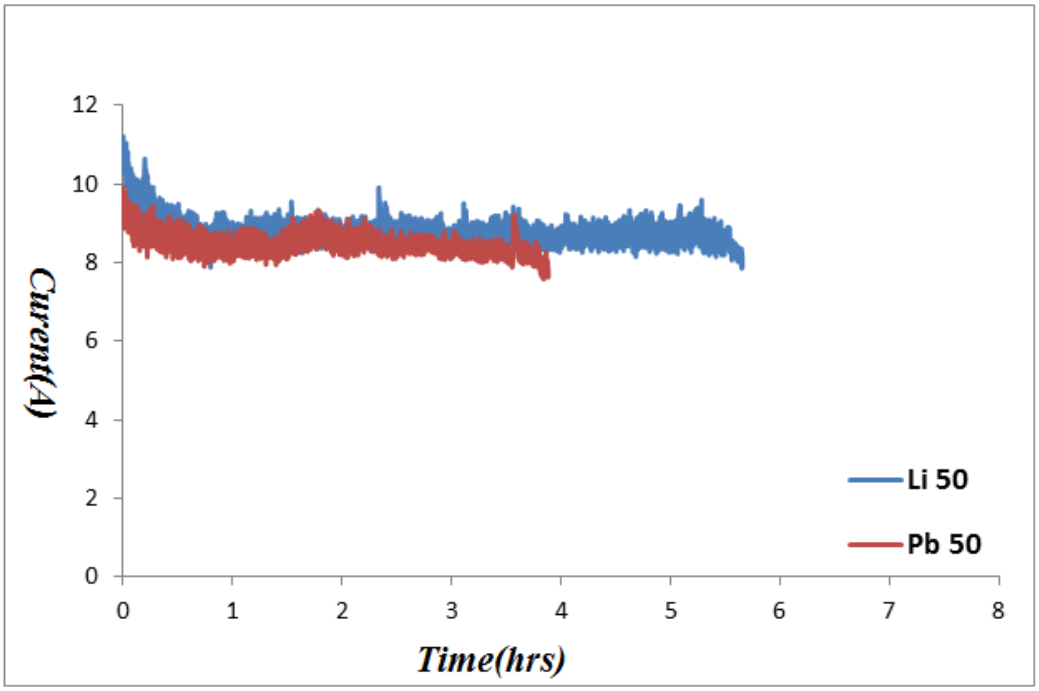

(b)

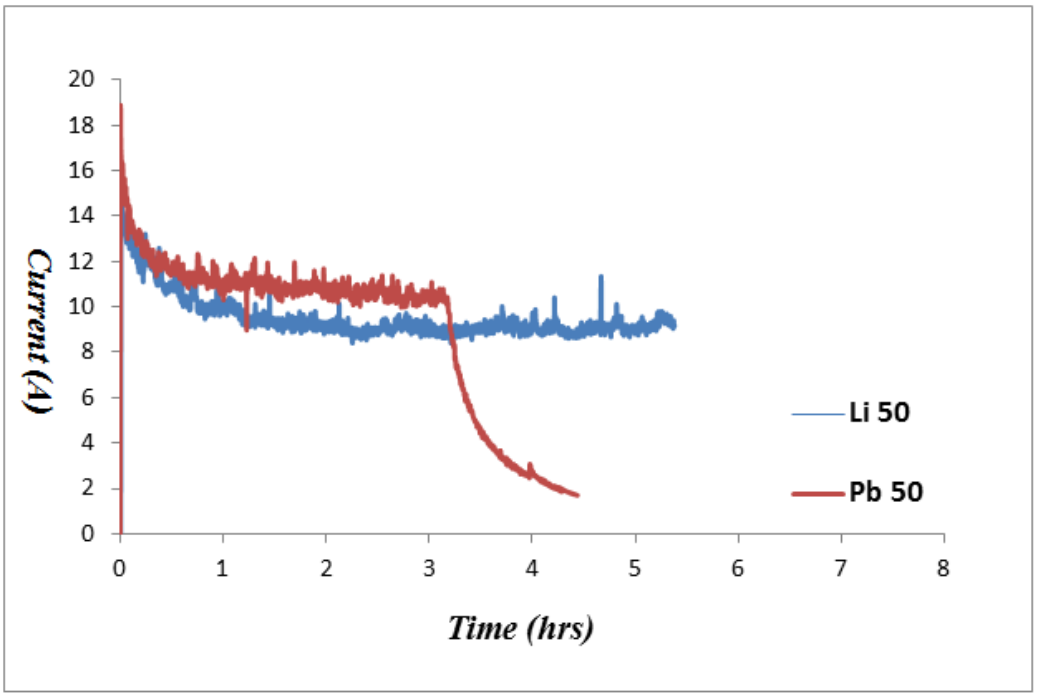

Figure 3.24 Motor performance test of hub and gear motor under the condition of case4 270lbs. (a) Operating voltage and current as a function of time for hub motor and (b) Operating voltage and current as a function of time for gear motor

6. Conclusion

6.1 Weight Comparison after Replacement

Table 3.4 Weight comparison between new and old design

	With Gear Motor and Lead-acid Battery		With Hub Motor and Li-ion Battery
	Chair (including the supporting arms):	53 lbs.	53lbs.
	Two batteries :	each 26.5 lbs. 33Ah	**each 16.1 lbs. 50Ah**
	Two motor-reducer systems:	each 17.5 lbs.	**each 11 lbs.**
	Bottom frame (including rear wheels):	35.5 lbs.	35.5 lbs.
	Two front wheel assemblies:	each 4.5 lbs.	each 4.5 lbs.
	Foot rest:	6.0 lbs.	6.0 lbs.
	Controller box:	2.0 lbs.	2.0 lbs.
	Two plastic frames (including some parts to connecting bottom frame):	3.5 lbs.	3.72 lbs.
	Total weight:	197.0 lbs.	**163.42 lbs.**
	Weight Reduced (%)		**(17.04%)**

Table 3.4 compares the weight of the wheelchairs powered with (1) the gear motor and lead acid battery and (2) the hub motor and Li-ion battery. The first column in *Table 3.4* list the original weight and the weight after replacement of Jazzy 1113 Power Chair, the original weight of motors and reducer system is 35lbs., 17.8% of the total weight, the batteries is 53lbs., 26.9% of total weight. In the second column, list the weight after we replace the gear motor and lead-acid batteries with light weight, high efficient hub motor, and high energy density, better performance Li-ion batteries, the improvement is significantly, the weight percentage of powertrain and battery in the whole electric

wheelchair system reduced form 17.8% to 13.6% and 26.9% to 19.7% respectively, The total weight reduced is from 197.0lbs. to 163.42 lbs. and what need to emphasized is that not only reduced the weight by replace the battery but also increased the capacity from 33Ah to 50Ah.

6.2 Battery Performance Improvement

In summary, from the data collected in the battery test, it is obvious that higher weight loads requires more power, resulting in the withdrawal of more current from the batteries. Comparing between Li-ion 50Ah battery and Lead-acid 50Ah battery (see *Figure 3.25(a)),* we can find that when the wheelchair is powered by 50Ah Li-ion batteries, the capacity can be fully utilized under all testing conditions, while for the lead-acid batteries, the percentage can be utilized of capacity decrease gradually from 95% to 70% with increase the load from zero to 270lbs.. From *Figure 3.25(b)* we can see that by change the battery type from Lead-acid to Li-ion, the running time of electric wheelchair, increased 0.4 hrs. 2.4 hrs. , 2.2 hrs. and 2.1 hrs. under No Load, 90lbs. load 180 lbs. load and 270 lbs. load respectively. Thus, we can draw a conclusion that Li-ion batteries are more suitable for high current continuous output situation compared to Lead-acid batteries. And we highly recommend Li-ion battery for those overweight customer rather than Lead-acid batters in order to ensure the range of activities and duration of running time.

(a)

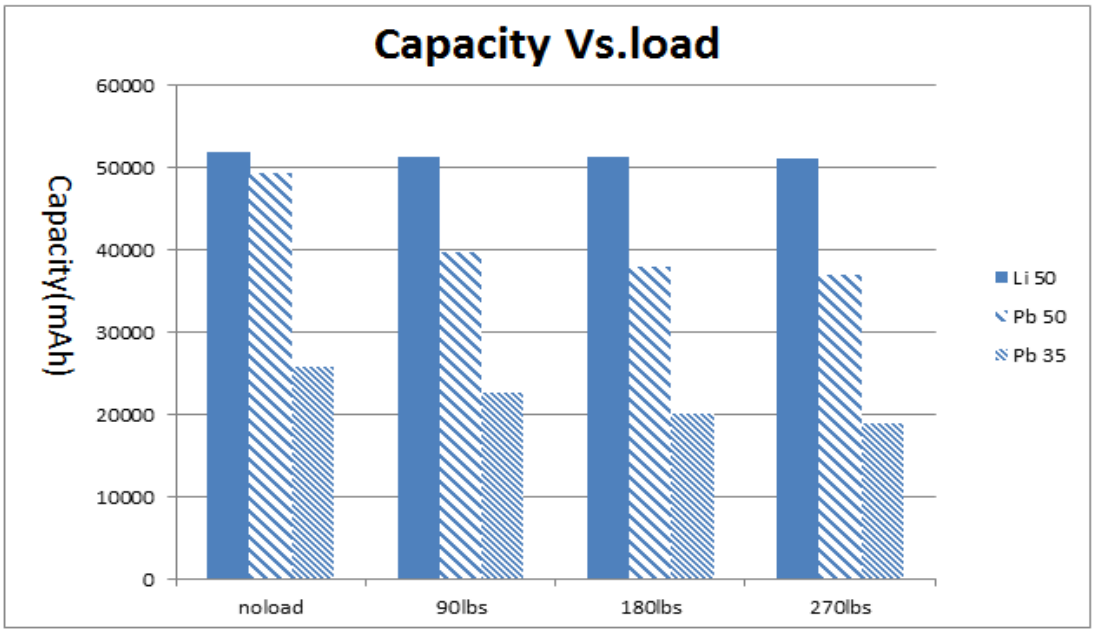

(b)

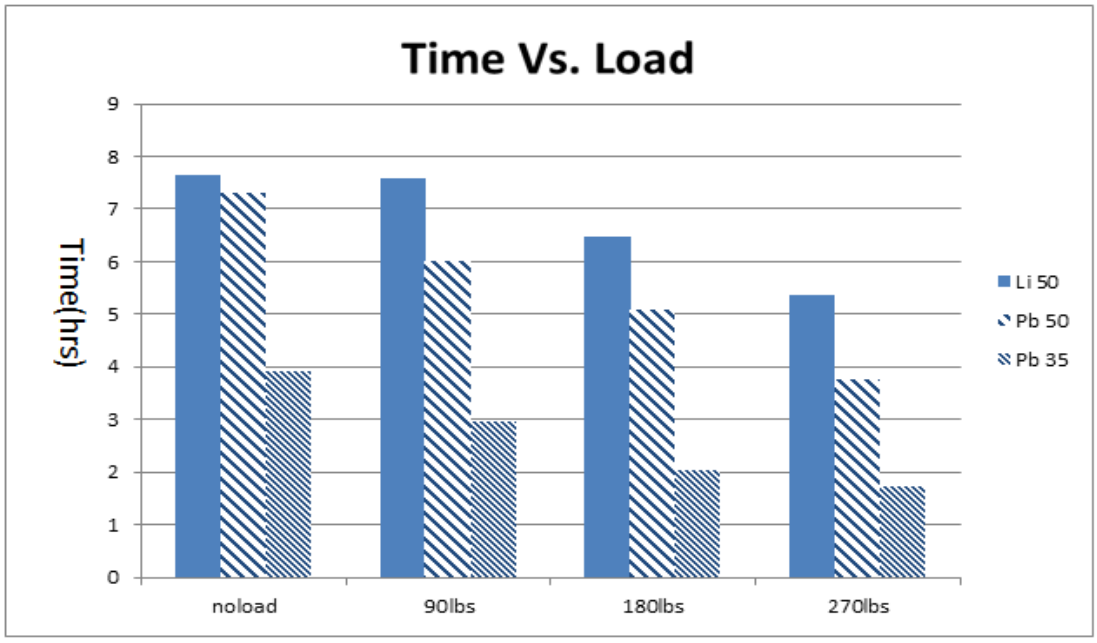

Figure 3.25(a) Discharge capacity of three types of batteries under each simulation case and (b) Discharge time of three types of batteries under each simulation case

Table 3.5 The discharge capacity and the relative percentage based on Li-ion batteries of the three kinds of testing batteries

Battery / Case	Li 50		Pb 50		Pb 35	
	Capacity(mAh)	Percentage %	Capacity(mAh)	Percentage %	Capacity(mAh)	Percentage %
No Load	51689	100	49300	95.37	29220	56.53
90lbs	51628	100	39953	77.73	26228	50.80
180lbs	51754	100	37654	72.75	23830	46.04
270lbs	51240	100	35473	69.15	22442	43.79

Table 3.6 The discharge time and the relative percentage based on Li-ion batteries of the three kinds of testing batteries

Battery / Case	Li 50		Pb 50		Pb 35	
	Time(hrs)	Percentage %	Time(hrs)	Percentage %	Time(hrs)	Percentage %
No Load	7.7	100	7.4	96.10	3.9	50.64
90lbs	7.5	100	6.1	81.33	2.9	38.66
180lbs	6.6	100	5.1	77.27	2.0	30.30
270lbs	5.4	100	3.8	70.37	1.8	33.33

6.3 Motor Improvement

In the summary of motor test, it is worth to note that the two kinds of motors are limited by the controller to running under 6mph (maximum speed), which is for the safety reason. From the *Figure 3.26 (a)*, it can be seen that for lead acid battery, the running time increased at least one hour under each case after installing the hub motors. For the Li-ion battery, the running time under the no load case increased one and a half hours. But for the other three cases, the operating time increased less than half hour after replacing gear motors with hub motors. From the *Figure 3.26 (b)*, we can see that the operating currents are reduced by 1A after installing hub motors when the wheelchair is powered by either lead acid or Li-ion batteries. The improvement withdrawal more capacity when using lead-acid batteries can be attributed to the reduction of the output current and increase of the efficiency after replacing the gear motors with the hub motor. When using Li-ion batteries, the running time extended longer under no load case is the synergetic result of the reduced weight and the increased efficiency which is the same as using lead-acid batteries. It is also interesting to note the difference under the three loading cases. Because the Li-ion battery is not much less sensitive to the output current compared to lead acid battery, the maximum capacity can be reached either with gear motors or hub motors leading to insignificant change of running time.

(a)

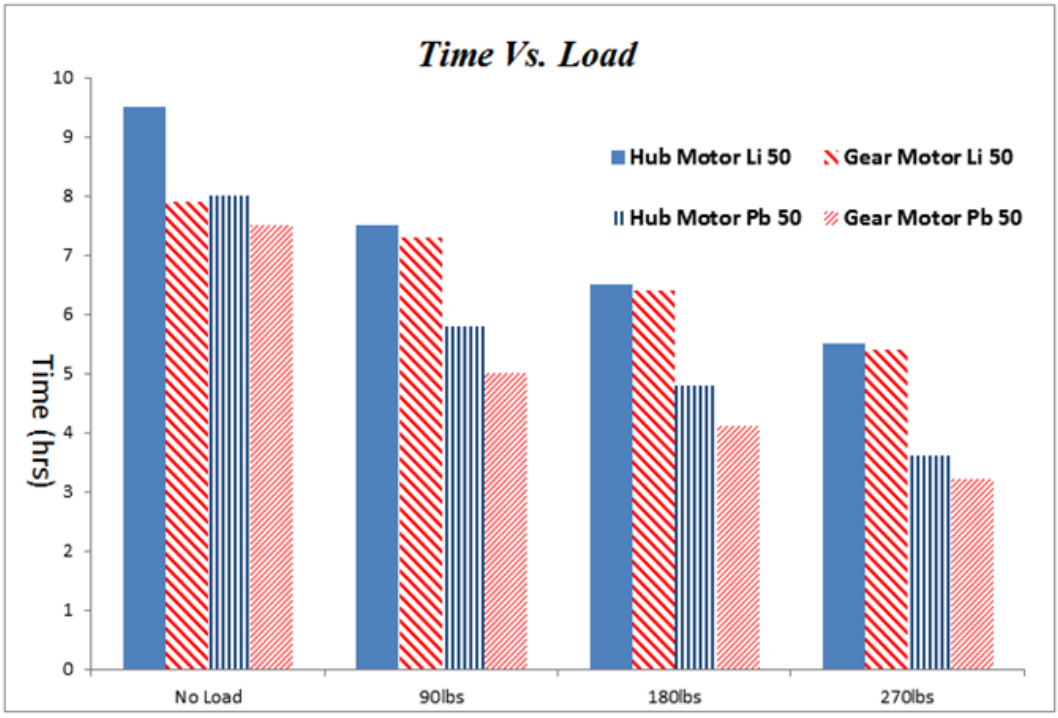

(b)

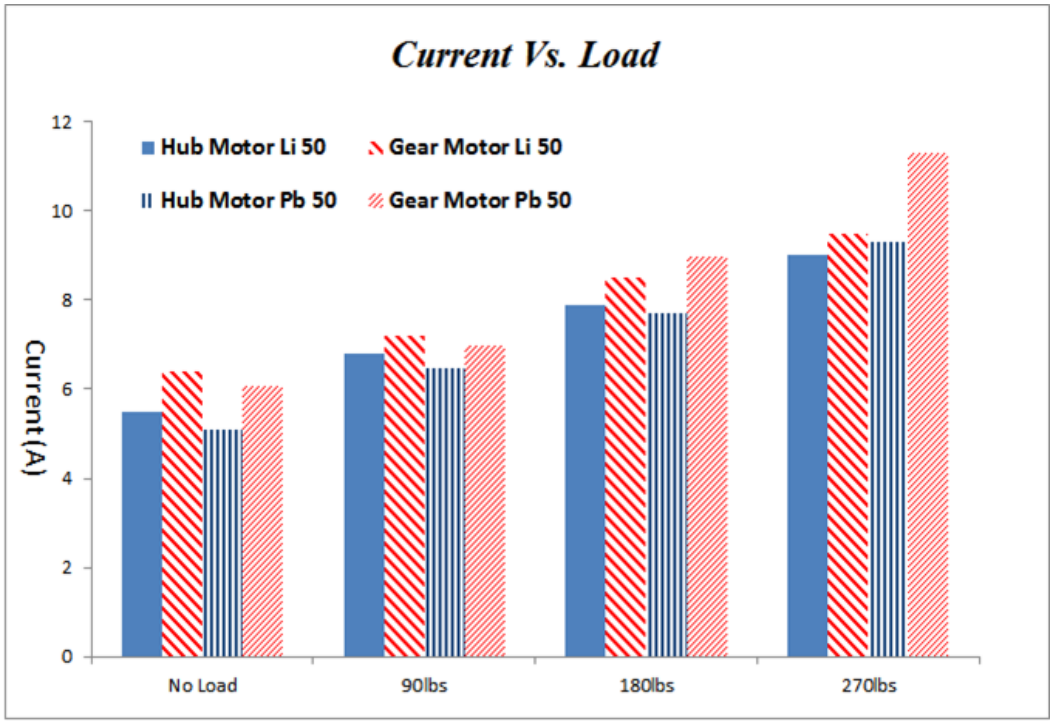

Figure 3.26(a) Discharge time comparison between hub motor and gear motor under each simulation case and powered by two types of batteries and (b) Discharge current comparison between hub motor and gear motor under each simulation case and powered by two types of batteries

Table 3.7 The discharge time of hub and gear motor under the power of Li-ion and lead acid battery and the relative percentage based on Li-ion batteries of the three kinds of testing batteries

Motor / Case	Hub Motor Li 50		Gear Motor Li 50		Hub Motor Pb 50		Hub Motor Pb 50	
	Time(hrs)	Percentage %	Time(hrs)	Percentage %	Time(hrs)	Percentage %	Time(hrs)	Percentage %
No Load	9.5	100	7.9	83.15	8	84.21	7.5	78.94
90lbs	7.5	100	7.3	97.33	5.8	77.33	5	66.66
180lbs	6.5	100	6.4	98.46	4.8	73.84	4.1	63.33
270lbs	5.5	100	5.4	98.18	3.6	65.45	3.2	58.18

Table 3.8 The discharge current of hub and gear motor under the power of Li-ion and lead acid battery and the relative percentage based on Li-ion batteries of the three kinds of testing batteries

Motor / Case	Hub Motor Li 50		Gear Motor Li 50		Hub Motor Pb 50		Gear Motor Pb 50	
	Current (A)	Percentage %	Current (A)	Percentage %	Current (A)	Percentage %	Current (A)	Percentage %
No Load	5.5	100	6.4	116.3	5.1	92.72	6.1	110.9
90lbs	6.8	100	7.2	105.8	6.5	95.58	7.0	102.9
180lbs	7.9	100	8.5	107.5	7.7	97.46	9.0	113.9
270lbs	9.0	100	9.5	105.6	9.3	100.3	11.3	125.5

Chapter 4: Design Studies of an Eddy-Current Dynamometer for Energy Efficiency Verification

1. Introduction

A dynamometer can be used to determine torque and power required to operate a driven system. Eddy current (EC) dynamometers are the most commonly absorbers used in modern chassis dynamometer [28]. An eddy current dynamometer is usually consisted of a metal rotor and 6 or 8 pieces of stators to produce an electromagnetic field. The voltage and current applied on stators will change the strength of the magnetic field. In addition, it requires an electrically conductive core, shaft, or disc moving across a magnetic field to produce resistance to movement. Most eddy current dynamometers are air or water cooled.

In this study, two kinds of eddy current dynamometers were designed for high rotational speed - low torque motor and low rotational speed - high torque motor, respectively. In general, the design principle of the eddy current dynamometers is as the following: 1) By reading the current and voltage from PowerLog sensors connected between the motor and battery, input power (P_{in}) is calculated by multiplying them together; 2) Motor, rotational shaft, torque sensor and the rotor are sequentially connected in series. When the rotor begins to rotate with the shaft in the electromagnetic filed

produced by the stator, eddy current will be generated in the rotor; and 3) According to Lenz's law, the eddy current will be always against the change of the magnetic flux in the rotor. As a result, a force in an opposite direction of the movement will be generated. The rotational speed can be read from the PowerLog sensor. And from the equation $P = \tau \times \omega$, the maximum output power (P_{out}) can be calculated. The ratio of input and output power is the efficiency of the motor under the test.

2. Dynamometer Design for High-Speed Low-Torque Motor

The first step of this project is to verify the feasibility and accuracy of the design before applying it on the larger wheel chair electric motor. An incorrect and incomplete design from another student's past project, originally developed from the research of WU [30], was modified and selected in this step.

Figure 4.1 shown below displays the configuration of the high speed motor dynamometer. The electric motor is coupled to the eddy brake with a rotary socket torque sensor made by OMEGA. This torque sensor measures torque up to 1500 in*lbs and the maximum running speed is 5000 RPMs. Additional sensors are added to measure the RPMS, current and voltage of the motor. The electric motor used in this test is for RC airplanes and has a power of 800 watts. The range of the rotational speed of the motor is 2000 RPMs to 4000 RPMs.

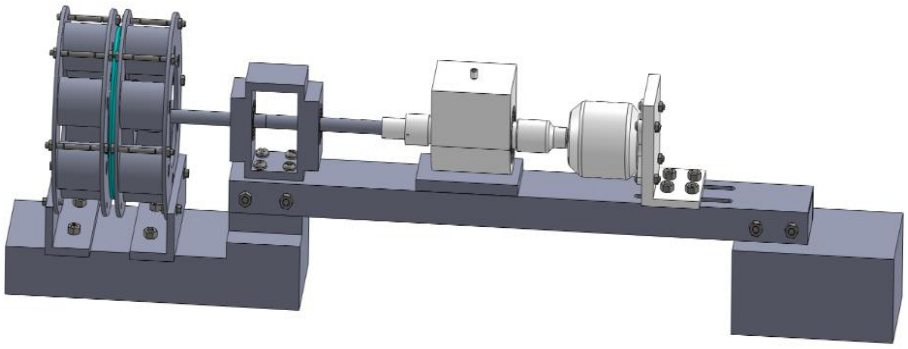

Figure 4.1 The prototype design of eddy current dynamometer for high speed low torque motor use, from right to left is stators, rotor, torque sensor and motor

2.1 Theory and Primary Calculations of Stators

When designing an eddy brake used as a dynamometer, the primary consideration is how much torque can be produced under a certain angular velocity. For the range mentioned above, the torque produced by the dynamometer must be greater than that of the motor. Because the torque produced by an eddy brake increases with the growth of the rotational speed, the eddy brake is designed that the torque it produced is equal to that produced by the motor at the minimum rotational speed, i.e. 2000 RPMs in this case.

The power equation of the electric motor is shown below:

$$P = \tau \times \omega \tag{4.1}$$

Here P is the power (Watts), τ is the Torque (Nm) and ω is the angular velocity (rad/sec). The equation can be rearranged as $\tau = \frac{P}{\omega}$. By converting 2000 RPMs to rad/sec and substituting it into the equation shown above, it was found that the desired torque produced by the eddy brake at 2000 RPMs is 3.82 N*m.

Once the desired torque of the eddy brake is acquired, the desired braking force of the eddy brake was found. The equation for torque of an eddy brake is

$$\tau = Fe \times R \tag{4.2}$$

Where $\tau\ is\ Torque\ (Nm)$, $Fe\ is\ Braking\ Force\ (N)$, and R is the radius of rotor disk (m). The equation 4.3 can be rearranged to find braking force from the desired torque $= \frac{\tau}{R}$. Using the desired torque 3.8 N*m and the radius of the rotor disk from the previous student's design, the desired braking force was found to be 66.49 N. Once the desired braking force was found, the brake could be designed.

To improve the accuracy of calculations and design, the J. H. Wouterse's model was later used. The J. H. Wouterse's model is an equation using variables and parameters of an eddy current brake to find the braking force [29].

$$Fe = \frac{1}{4}\frac{\pi}{\rho} D^2 d B_0^2 c v \tag{4.3}$$

$$c = \frac{1}{2}\left[1 - \frac{1}{4}\frac{1}{\left(1+\frac{r}{A}\right)^2\left(\frac{A-r}{D}\right)^2}\right] \tag{4.4}$$

Where,

$A = Disk\ Radius\ (m)$

$d = Disk\ Thickness\ (m)$

$Fe = \ Braking\ Force\ (N)$

$D = Diameter\ of\ Soft\ Iron\ Pole\ (m)$

$B_0 = Air\ Gap\ Induction\ at\ Zero\ Speed\ (T)$

$r = Distance\ From\ Center\ of\ Disc\ to\ Center\ of\ Pole\ (m)$

$\rho = \ Specific\ Resistance\ of\ Disk\ Material\ (\Omega \times m), (Aluminum)$

$v = Tangetial\ Speed\ of\ the\ roating\ disk, measured\ at\ center\ of\ pole\ (\frac{m}{s})$

The J. H. Wouterse's model can be rearranged to solve for the B_0, so that the electromagnets could be designed.

$$B_0 = \sqrt{\frac{4Fe\rho}{\pi D^2 dcv}} \tag{4.5}$$

Then $Air\ Gap\ Induction\ at\ Zero\ Speed$ B_0 value was divided by the number of magnets in order to find the amount of induction B produced by each magnet. The magnetic flux per stator was solved based on

$$\Phi = B * A_g \tag{4.6}$$

where $\Phi = Magnetic\ Flux\ Per\ Stator\ (Wb)$, $B = Induction\ Per\ Stator\ (T)$, and $A_g = Area\ of\ Gap\ (m^2)$.

After finding the magnetic flux per stator, the next step in designing the electromagnets was to find the total reluctance of each stator. The total reluctance R is the sum of the reluctance of the core R_{core} and the reluctance of the air gap R_{gap}

$$R = R_{core} + R_{gap}$$

$$\mathcal{R}_{core} = \frac{l}{\mu_0 \mu_r A_c} \tag{4.7}$$

$$\mathcal{R}_{gap} = \frac{g}{\mu_0 A_g} \tag{4.8}$$

Where $\mu_0 = 4\pi \times 10^{-7}(mgs^{-2}), permeability\ of free\ space,$

$\mu_r = relative\ permeability\ (Iron\ Core \sim 200)$

$A_c = Area\ of\ Core(m^2)$

$A_g = Ac \times 1.05, for\ 5\%\ fringing, (m^2)$

$g = length\ of\ air\ gap$

Assuming that the power supply would be capable of delivering 3 Amps of current through the coils, the number of turns per coil could then be calculated by

$$N = \frac{\Phi R_{Total}}{I} \tag{4.9}$$

In this design, an aluminum disk with a thickness of 0.125 in is used as the rotor and each of the 12 stator poles has (6 on each side of the motor to increase magnetic flux) a diameter of 0.5 in and a length of 1.5 in. Accordingly, the number of turns of copper wire per core was found to be approximately 316.

If the power supplies would be able to produce 3 Amps of current, the resistance of each stator unit (6 stator coils) can be calculated based on the Ohm's law,

$$R = \frac{\rho L}{A} \tag{4.10}$$

Where $R = Resistance\ (\Omega)$, $L = Length\ (m)$, $A_r = Area\ (m^2)$, $\rho = Resistivity\ (\Omega \times m)$. In this design, 18 gauge wires (0.0403 in. diameter) were chosen for the amount of current it could withstand. It was calculated that approximately 6000 in of wire would be needed for each stator unit. Since the resistivity of copper is $1.68 \times 10^{-8}\ (\Omega \times m)$, the resistance of each stator unit was found to be 3.095 Ω. And by applying Ohm's Law, the required voltage for each stator unit would be 9.28 V.

From:

$$\int_0^T pdt - \Delta(E + V) = 0 \tag{4.11}$$

Where *P* is the instantaneous power *t* is time we can get:

$$\mathrm{p} = \frac{2S^2\Delta_h B^2\omega^2 sin^2\omega t}{\pi\rho} \tag{4.12}$$

$$\Delta_h = \sqrt{\frac{2}{\omega\mu_r\mu_0\sigma}} \tag{4.13}$$

And

$$\mathrm{p} = \frac{1}{T}\int_0^T pdt = \frac{S^2\Delta_h B^2\omega^2}{\pi\rho} \tag{4.14}$$

Therefore,

$$\mathrm{T} = \frac{N_p^2 S^2 \Delta_h B^2 \omega^2}{\pi \rho} \tag{4.15}$$

T*able 4.1* summarizes the calculation results and the parameters of the first dynamometer we designed. In order to produce enough torque the parameters in the table have to be fulfilled. Calculation based on *equation 4.11* to *4.15* results in the braking torque and motor torque as a function of RPMs within the motor range from 200o to 4000, which is plotted *Figure 4.1*. In the figure, we can see that the braking torque is increase with the rotational speed and always larger than the motor torque in the given range of the rotational speed which means that our design has met the requirement.

Table 4.1 The calculation results and design parameters to be used in the dynamometer for the selected high speed low torque motor

<table>
<tr><td>Rotational speed range (rpm)</td><td colspan="2">2000</td><td colspan="2">4000</td></tr>
<tr><td>Desired torque range (N*m)</td><td colspan="2">3.82</td><td colspan="2">1.88</td></tr>
<tr><td>Desired force range (N)</td><td colspan="2">66.49</td><td colspan="2">32.98</td></tr>
<tr><td>Reluctance in the circuit (H)</td><td colspan="2">1.3972e6</td><td colspan="2">1.3972e6</td></tr>
<tr><td rowspan="5">Design parameters</td><td>Wire gauge</td><td>16</td><td rowspan="3">Input current</td><td rowspan="3">3A</td></tr>
<tr><td>Wire resistance</td><td>3.095Ω</td></tr>
<tr><td>Length of wire</td><td>152.2m</td></tr>
<tr><td>Turns</td><td>316</td><td rowspan="2">Input voltage</td><td rowspan="2">9.28V</td></tr>
<tr><td>Number of stators</td><td>12</td></tr>
</table>

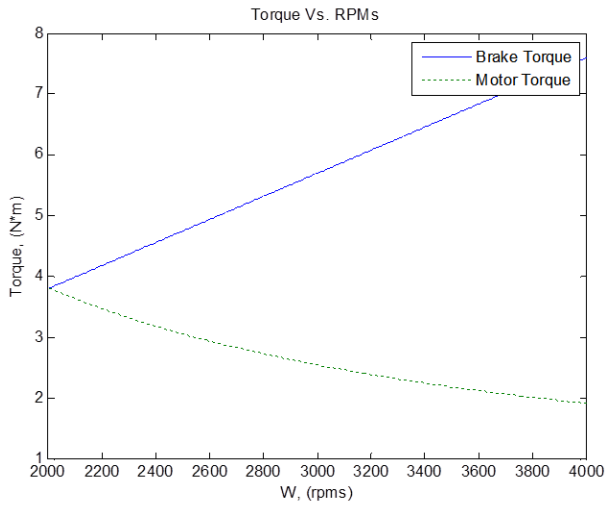

Figure 4.2 Calculated brake torque and motor torque as a function of rotational speed in the range of 2000 - 4000 rpm based on the first design parameters

2.2 Shaft and Disk Strengthen Verify and Design

Figure 4.3 shows the 3D model of rotor and stator designed using Solidworks for the high speed low torque motor. There are six pairs of stator and 316 turns of copper wire on each one for generating sufficient magnetic field for braking. The material of the rotor disk is aluminum which has a high conductivity of 3.5*10^7 S/m and low price compared to other metals.

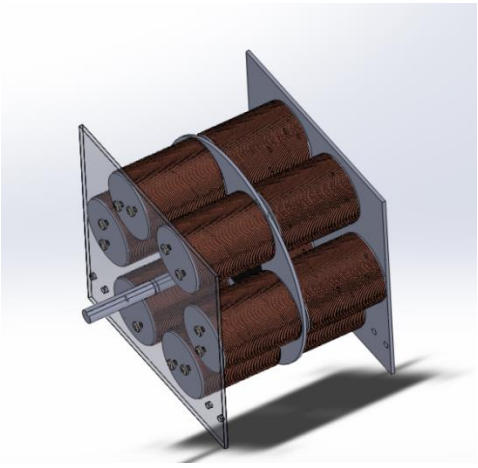

Figure 4.3 3D Model of rotor and stator for the high speed low torque motor, six pairs of stator and an aluminum rotor in the middle

The physical case of this study is to verify the shaft and aluminum disk can stand the max torque inputted from the high speed low torque motor and the criteria is maintain the displacement on the rotor is less than 0.5mm. We use FEA method of Static analysis in Solidworks to do the simulation. The reason for choosing static analysis is due to the frequency of input load is much lower than the fundamental frequency of this system.

Table 4.2 shows the mesh setup of this static simulation. The Jacobin points are used to define how good or bad the mesh is. In this study we set it as four points due to no complex surface or edges in the system and provide a faster calculation speed. The element size and tolerance were automatically calculated by Solidworks according to the size and geometrical shape of the components.

Table 4.2 Mesh information of shaft static analysis of the dynamometer design used for high speed low torque motor

Mesh Information

Mesh type	Solid Mesh
Mesher Used:	Standard mesh
Automatic Transition:	Off
Include Mesh Auto Loops:	Off
Jacobian points	4 Points
Element Size	0.314806 in
Tolerance	0.0157403 in
Mesh Quality	High
Remesh failed parts with incompatible mesh	Off

Figure 4.4 (a) shows the mesh result of this static analysis. *Figure 4.4 (b)* shows the boundary condition we selected. The green arrow on the disk is the fixture constrain and the green arrow on the shaft represents a bearing support at the end of the shaft to constrain the displacement on X,Y,Z direction. Purple arrow is the torque which applied to the shaft. And the blue arrow is a label of screw connection.

(a)

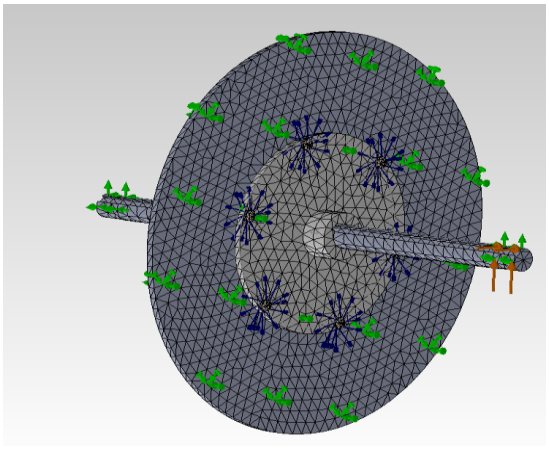

(b)

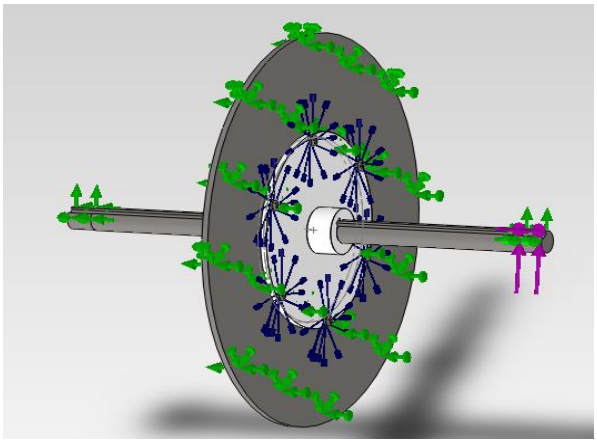

Figure 4.4 (a) mesh result; (b) boundary conditions in the case of shaft displacement static analysis in order to verify the strength of the system can stand the input torque

Figures 4.5 (a), (b) and *(c)* presented the results of simulation in terms of stress, displacement, and strain, respectively. From *Figure 4.5(a)* we found that the max stress is 439MPa and happened at the keyway area. Since the ultimate tensile strength of steel is equal to *841MPa,* the shaft will not yield at that area. From *Figure 4.5(b)* we can see that the stress only causes a negligible displacement of *3.117e-001 mm*. From *Figure 4.5 (c)*, there is no strain concentrated in any small area on the disk although the strains are distributed around the Polycarbonate disk. Hence we can conclude that the system is strong enough to do the following test.

(a)

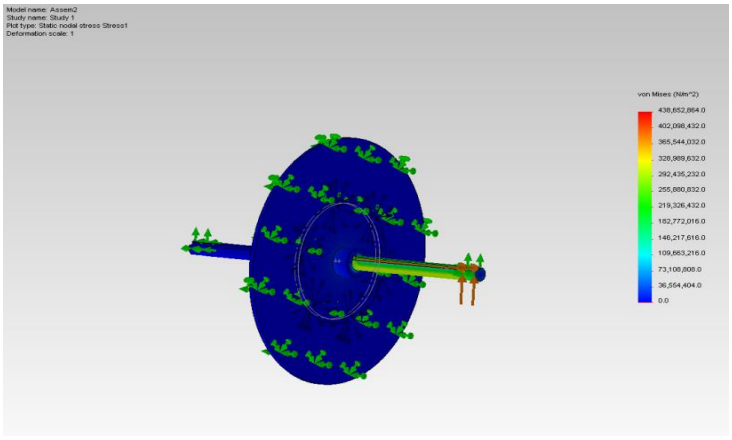

(b)

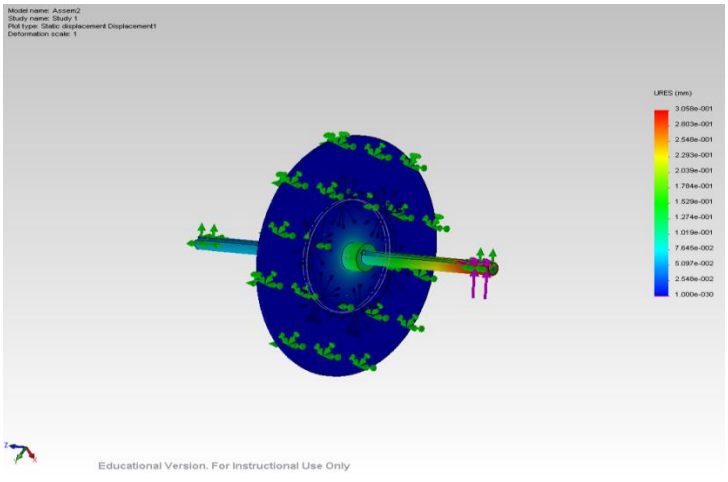

(c)

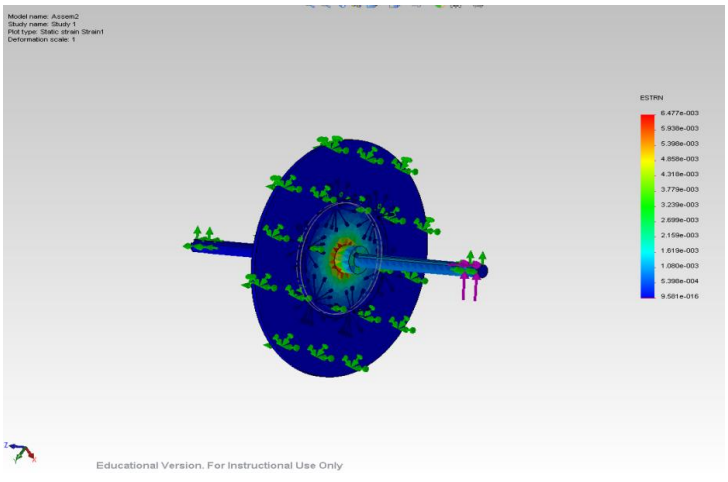

Figure 4.5 The simulation results showing the distribution of (a) stress (b) strain and (c) displacement of the rotor and shaft for the low torque high speed motor use dynamometer

2.3 Dynamometer Assembling and Test Results

After all of the designs, calculations and simulations have been completed, we manufactured each part and assembled them together, which is shown in *Figure 4.6*. Each stator in the figure is evenly placed in the support disks with the interval distribution of North Pole and South Pole.

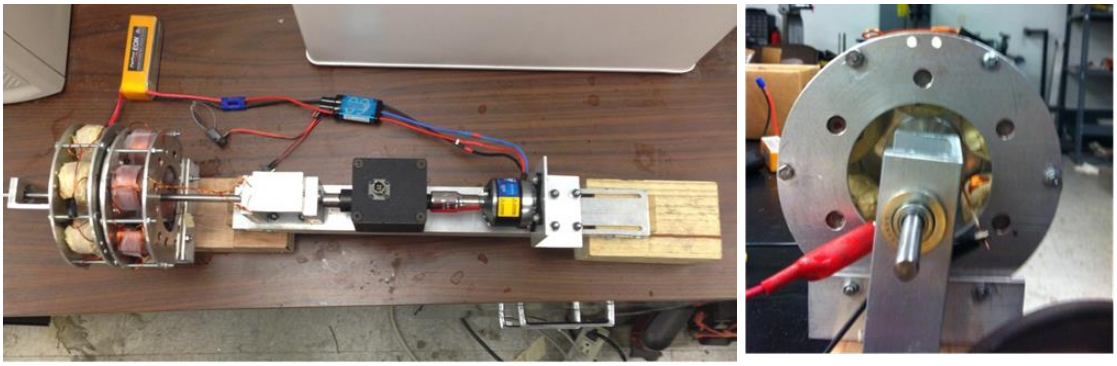

Figure 4.6 Assembly of first prototype dynamometer top (left) and side view (right)

However in the test, the performance of the dynamometer is not like what we expect. According to the calculation showing in *Table 4.1*, the torque generated by the eddy current should be able to stop the rotor from rotating when the rotational speed of the exceeded 2000RPM. But in fact, the rotational speed of the rotor did not slow down enough and the surface of the rotor is not heat up as well.

2.4 Failure Analysis

After careful checking and testing, the reasons that the performance of dynamomter did not match with the calculation and theory in the design can be attribbuted to the following manufacturing flaws:

2.4.1 Air Gap Precision Control:

From the *equation 4.10* and *4.11* we know that the reluctance of air gap is proportion to the distance of gap. In the process of assembling, it is difficult to guarantee the 3mm length of air gap due to the bolt hole location on the wood base is not coincidce with the hole on the L channel. We had to make a little adjustment to the hole on the base in order to put the bolt in. Consequently, the air gap became larger than that was designed.

2.4.2 Insufficient Wire Turns:

In the design, we didn't fully take into account of the difficulties arised in the manufacturing process. Winding wires is not as easy as we had expected and the space limitation was ignored. In the design, the core of the stator is a 1.5in long and radius of 0.25 in steel rod. In order to ensure the wire from burning out, 16 gauge magnatic wire is necessary. As a result the radius of the magnatic wire compared to the radius of the steel rod is not small enough for us to wind up to 316 turns. The utmost winding turns we could achieved are 198, which is only 62% of the design value. The second difficulty we faced is the surface of the steel rod is too smooth to wrap the coil on and keep firmly contact with each orther. As a result too big air gap between the coil and the core. The high magnetic reluctance of air decreased the magnetic field intensity and the ability to restraint magnetic flux.

2.4.3 The Connection Between the Shaft and Rotor and the Location of Bearing:

The connection between the shaft and rotor shown in *Figure 4.7* is not work very well due to two reasons. Firstly, the bearing is unable to constrain the vibration of rotor due to the location is too far away. Secondly, the screw hole on the shaft is so shallow that the connect screw constantly falls off during the rotating test.

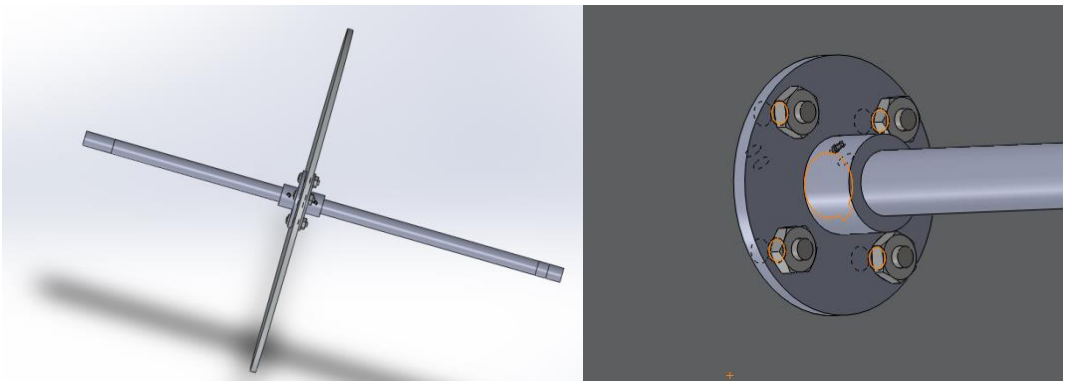

Figure 4.7 Image showing the connection between shaft and rotor in the high speed low torque motor use dynamometer overall view (left) and enlarge view (right)

3. Dynamometer Design for Hub Motor

Due to the low rotation speed and high power characteristics of a hub motor, the torque inputted form the hub motor is much higher than the previous motor. Consequently, larger stator, more wire turns, bigger rotor and a higher strength shaft are required.

After analyzing the possible reasons for the failure occurred in the first prototype dynamometer for the high speed low torque motor, we have figured out the ways to

overcome the corresponding problems and begin to design the second version dynamometer for the testing Hub motor to be used in the new electrical wheelchair.

The basic ideal is from the paper written by E.Simeu and D.Georges in 1995 *(Figure 4.8)* [31]. This design is consisted of 6 full of copper wire stators and a copper disc as the rotor, the stators are circled around the rotational shaft. With this design concept of eddy current dynamometer in their paper, we changed the shape of stator from round bar to a rectangle shape to tackle the problem that no enough wire coils can be wound on the stators.

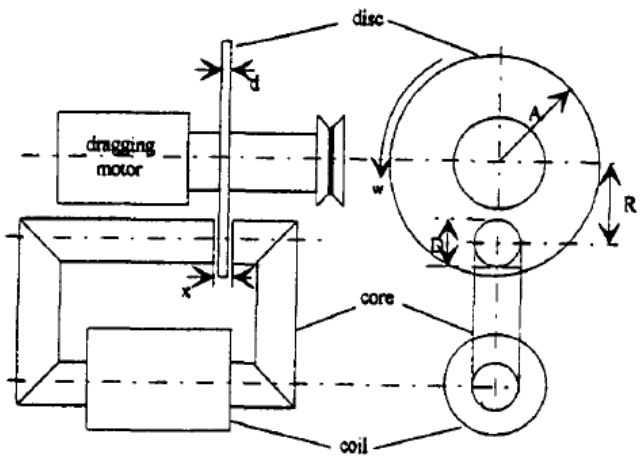

Figure 4.8 Eddy current brake design reported in 1995 [30]

From *Figure 4.9* we can see that the turns are wound in the middle of the stator to produce balanced magnetic field in both side, and due to there are insulate skin on the wires, we do not need to consider the problem of short circuit except too hot temperature from the rotor melt the skin. Because the power of the hub motor is 180W and the rotational speed is about 140 RPM, the torque generated from it will be much higher than the previous motor. There for, accounting to the calculation we need about 800 turns of copper wires to produce enough magnetic flux.

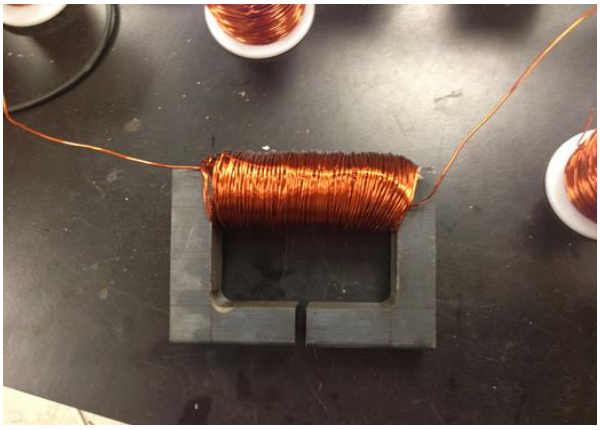

Figure 4.9 Image of one stator for hub motor use dynamometer which is contains 800 turns of 16 gauge wire

In order to prevent the air gap failure happening again, our design is improve in the following two aspects: 1) using six screws to fix the rectangular stator to the stable wall of the dynamometer directly; 2) supporting the left end of the shaft by a bearing which can be adjust to appropriate position to compensating the error which accumulated from right hand side when we assembly all together; and 3) locating another bearing support as close as possible to the rotor for reducing the vibration and increasing the rigidity of the system.

In practice, we know that when the movement of the disk through the magnetic field of the electromagnets creates eddy currents in the disc, it can be considered as a swirling current flowing in the low resistance conductor, which is similar to a short circuit generating a huge amount of heat and the coil on the stator also can be consider as a heat source depending on the input current, in order to extent the use life of dynamometer and prevent the short circuit caused by melting skin on the wire coils, a high efficient cooling system is necessary. In this design, we include the air cooling system which is consisted of three pairs of Fan 412. We have performed a flow simulation to evaluate the

performance of installing three fans on each side of the dynamometer. The cooling system design is described in detail in session 3.2.

Figure 4.10 exhibits the new design of the eddy current dynamometer to be used to determine the torque of hub motor during operation. In the design, the parts from the right side to left side are hub motor, Omega torque sensor and the combination of rotor and stator. In the test, a PowerLog sensor will be connected to the hub motor in series for reading the input power. At the same time the output power will be measured and recorded by Omega Torque sensor when the rotor spinning in the magnetic field created by the electromagnets. The mechanism of calculation is finding the point when the brake force produced by the electromagnets equal to the torque from the hub motor.

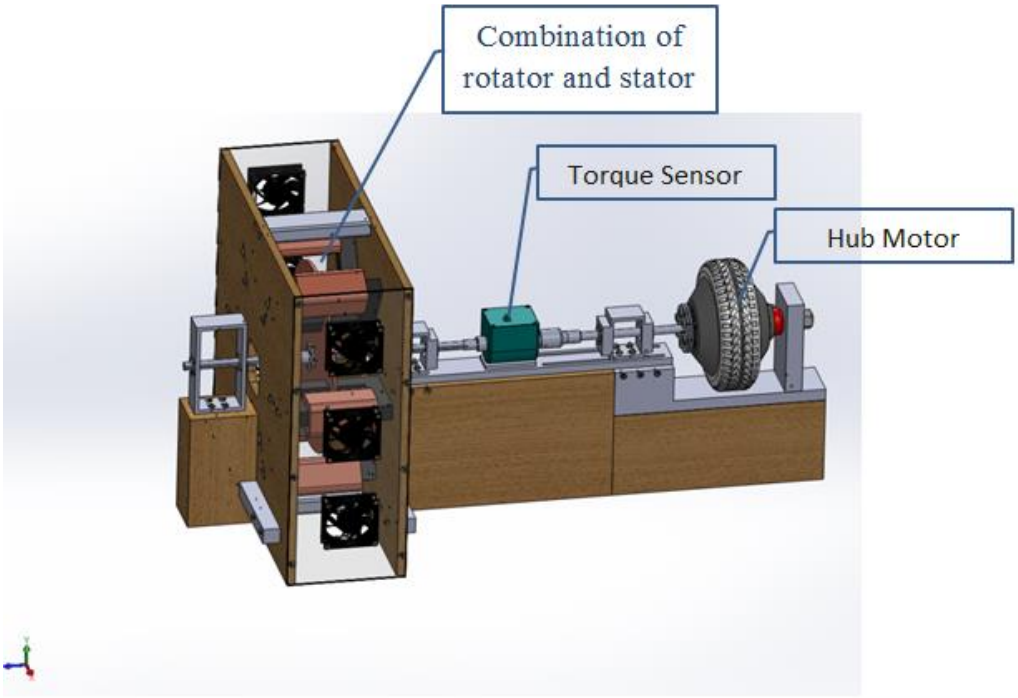

Figure 4.10 Final design of eddy current dynamometer for hub motor use which consist of air cooling system, six stators, torque sensor, and hub motor

3.1 Shaft and Disk Verification

Because of input torque increased a lot after we change the motor from high speed motor to the hub motor, it is necessary to redo a strength analysis for shaft and disk in order to prevent any failure occurrence during the testing.

A design study *table 4.3* shows how we looking for the optimal results of stress and displacement by varying the diameter of shaft from 0.25in (6.35mm) to 0.5in (12.7 mm). After comparing the computed stresses, displacements and masses in the five scenarios, we determined the best result of 0.375in (9.525mm) as our shaft in the dynamometer.

Table 4.3 Study table of shaft and rotor for verifying the displacement and stress with different diameter of the hub motor use dynamometer

	Scenario 1	Scenario 2	Scenario 3
Diameter of rotor	0.25in	0.375in	0.5in
Diameter of fix	0.25in	0.375in	0.5in
Diameter of shaft	0.25in	0.375in	0.5in
Stress1	18699 N/mm^2	3149.8 N/mm^2	500.81 N/mm^2
Displacement1	0.12318in	0.03493in	0.01891in
Mass1	0.0241202 lb	0.0615633 lb	0.113688 lb
Frequency1	953.20886 rad/s	993.07806 rad/s	1038.25391 rad/s
Frequency2	3333.3418 rad/s	3423.31006 rad/s	3512.12915 rad/s
Frequency3	3356.74219 rad/s	3449.35205 rad/s	3540.91211 rad/s
Frequency4	5472.80176 rad/s	5534.58545 rad/s	5605.73486 rad/s
Frequency5	5493.63672 rad/s	5540.4043 rad/s	5624.19971 rad/s
Displacement2	2.17836in	2.19989in	2.17997in
Mass2	6.83764 lb	6.87923 lb	6.93523 lb

In addition, *Figure 4.11* shows if the resonance phenomenon happened in the system the maximum displacement is 9.102e2 mm. However, from table 4.3 we know the first natural frequency of the system is 953.2 rad/s (10924.19 RPM) which is much higher than the maximum rotational speed of the hub motor. In other words, the results of model

analysis indicated that the resonance phenomenon will not happen due to there is no overlap between these two frequencies.

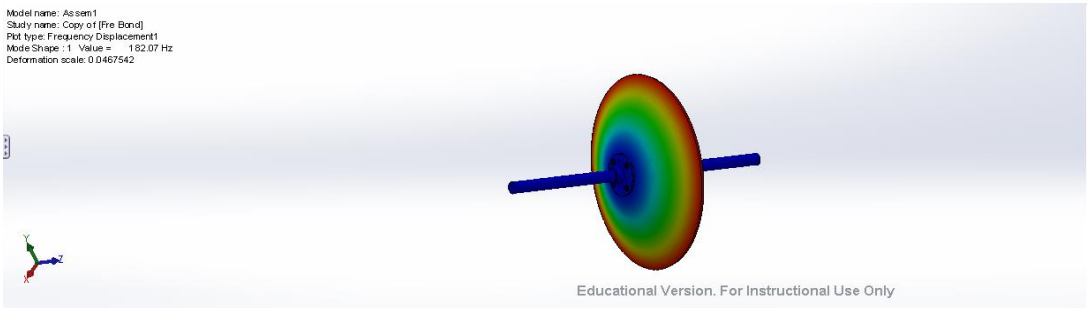

Figure 4.11 The simulation result of deformation generated at the shaft and rotor if the resonance phenomenon occurred in the system

3.2 Cooling System Design

For evaluating the effect of cooling system, we use flow simulation in Solidworks to simulate the ambient temperature of the brake system and the Heat Flux coefficient of the heat source and simulating how air flow through the electromagnetic parts. *Table 4.4*is the Specification of Fan 412 which lists the key parameters we inputted in the simulation.

Table 4.4 Fan 412 Specifications used for setup the flow simulation of hub motor use dynamometer [31]

Papst 412FM 40mm Quiet Fan Specifications	
Dimensions	40 x 40 x 10 mm
Mass	17 g
Air Flow (m^3/h)	6
Air Flow	3.5 CFM
Nominal Voltage (V DC)	12
Voltage Range (V DC)	10...14
Noise	19 dB(A)
Bearing Type	Sintec-Sleeve Bearing
Power Input	0.6 Watt
Nominal Speed (min^{-1})	4300 rpm
Temperature Range	-20...+70 C
Service Life L_{10} at 20C (Hours)	45,000
Service Life L_{10} at 60C (Hours)	15,000

Heat is mainly generated from two parts, i.e. coil on the iron core and the rotor due to the eddy current flow inside.

The basic calculation of heat generation rate of each stator is:

$$R = L * \rho = \frac{220' \times 12 \times 25.4}{1000} \times 0.0132 = 0.885139\Omega \quad (4.16)$$

Where R is the resistance of the wire (Ω), $L\ is\ the\ length\ of\ the\ wire(m)$, and ρ is the resistivity of the wire (Ω/m). The copper resisivity is $0.0132\ \Omega$/m.

The power of heat generation (watt) from the coil can be calculated based on the input current I(A) and resistance of wire R,

$$P_s = I^2 \times R = 7.5^2 \times 0.885139\Omega = 49(watt) \quad (4.17)$$

The total power of the coils is then equal to

$$P_{Stotal} = P * 6 = 294\ (watt) \quad (4.18)$$

The heat generation rate of the rotor (P_R) is very complex for calculating the accurate value. Based on the conservation of energy principle, we know that the heat generation power should be less than the total input power minus the power consumed by the stator which is equal to the $P_R = P_p + P_m - P_{Stotal} = 386W$, where P_p is the maximum input power of power supply which is 500W, and P_m is the maximum input power of motor which is 180W.

Figure 4.12 shows how the air flow and heat convction in the system without and with three pairs of fan, under no fan case, only top is open for air exchange and due to no air pressure diference between two side of the system, the speed of air flow is slow. Under the case of adding three pairs of fan on each side, the the open area and air

pressure difference is increased therefore the speed of air flow and air exchange were increased as well, as a result the temperature in the system were decreased.

(a)

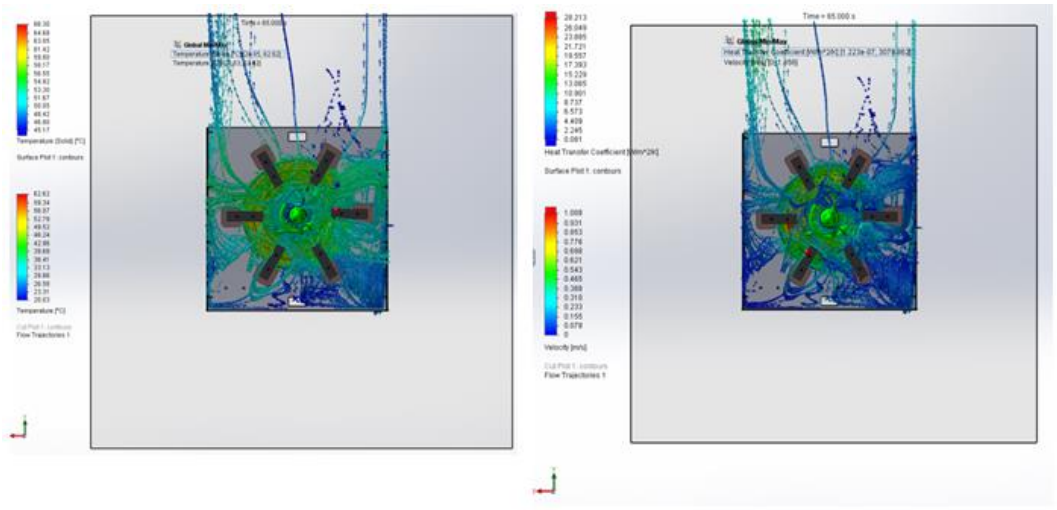

(b)

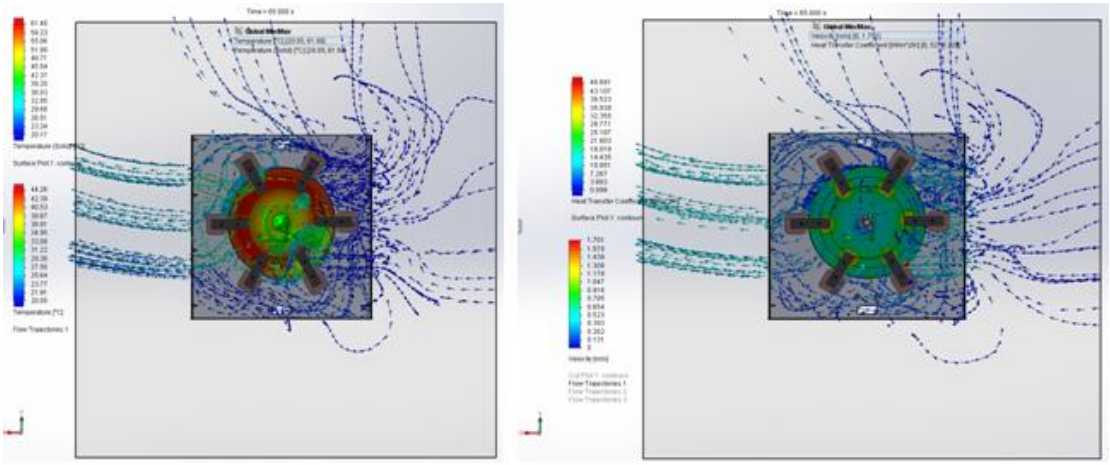

Fig 4.12 Simulation results showing the air flow around the rotor and stators and the surface temperature on the rotor (a) Case of no fan installed in the designed dynamometer system (b) Case of three pairs of fans evenly distributed around the rotor and stators on both sides

Table 4.5 shows the comparison of several parameters of the system with and without three pairs of Fan 412 on each side of the transparent plastic plate. And the physical time of simulation is 65 seconds.

In conclusion, by arranging three pairs of fan on each side, the ambient temperature reduced from 62.62°C to 44.26°C and doubled the heat flux coefficient of the rotor from

28.213 W/m^2/K to 46.961W/m^2/K which ensured the operating environment of the system.

Table 4.5 Comparison of the simulation results including the temperatures near and on the rotors, air flow velocity, and heat flux coefficient between the no cooling system in the design and three pairs of fans in the design

Name	Air Temperature near the rotor Max/Min(°C)	Temperature on the rotor Max/Min(°C)	Velocity of Air Max (m/s)	Heat Flux Coefficient Max$(W/m^2/K)$
With six Fans	44.26/20.05	61.40/20.17	1.701	46.961
Without Fan	62.62/20.05	66.30/45.17	1.006	28.213

4. Conclusion

In the first two sections we introduced and studied the theory of eddy current dynamometer. After that, we designed and manufactured a prototype for high speed low torque motor use, during the design we use Solidworks to verify the strength of the shaft and rotor. However, due to air gap precision control, insufficient wire turns and the connection between the shaft and rotor and the location of bearing, the dynamometer is not able to work in the test. In order to solve these problems, we read the paper published by E.Simeu and D.Georges and redesigned a new dynamometer for test the hub motor with the new shape of stators and the components for connecting the shaft with the rotor. During the design a study table was made to select the best shaft and prevent the resonance phenomenon happen in the system. In the last, due to the eddy current flow in

the rotor will cause a lot of heat and reduce the life time of the dynamometer. we did a flow simulation to compare the performance between no fan case and three pairs were added on each side of the dynamometer. From the result of simulation we can see that the ambient temperature reduced from 62.62℃ to 44.26℃ and increased the heat flux coefficient of the rotor from 28.213 W/m^2/K to 46.961W/m^2/K which ensured the operating environment of the system.

In addition, the prototype design, parts manufacture and assembly of the eddy current dynamotor is finished. The experience of manufacture and design concept which have been discussed in chapter 4 is a guidance and reference for the others to review. The only problem left before the final test and verify this design of eddy current dynamometer is how to synchronize the data between the input power terminal and output power terminal in order to get a continuous and accurate result. The design of these data processing systems, the final test works of the dynamometer will forward to my teammate to be continue.

Chapter 5: Prototype/Design of Onboard Functional Components/Mechanism

1. Introduction

In this chapter we added some functional components and mechanisms to the electric wheelchair to enhance the use experience. In order to add the ability of navigation and telecommunication for the electric wheelchair, an iPad holder was assembled to the wheelchair for holding iPad or other electronic devices. An on board power outlet were added to the electric wheelchair to extend the operating time of these devices. In the last, a wheel width changeable mechanism were designed to help user go through some narrow door and two quick battery release mechanism were designed to help user to take the bad battery out or replace the dead battery with fully charged battery without any waiting time.

2. Design and Install an Onboard iPad Holder

iPad is the most common tablet device currently due to its user friendliness, strong operational performance and thousands of available applications. Electric wheelchair users are able to take an active part in the social society with the help of it onboard. In order to free those severely disabled persons' hands from holding the iPad, we designed two onboard iPad holders.

The first design of the iPad holder is consisted of three main parts, the first part is a small rectangular aluminum plate which is connected to the slot in the armrest by a shaft, the function of this part is for rotating the main frame of the holder 90 degree vertically to lift it and hold the main frame in front of user. The second part is the main frame, *Figure 5.1* shows these two parts, the first on is used for rotating the iPad to different view position and the second one is used for adjusting the location of iPad in the horizontal direction. The last part is a slider connect to the main frame by an I beam and connect to the iPad with the special Velcro hook. Therefore, when the slider moves on the I beam the location of the iPad will be adjusted inside or outside.

Figure 5.2 shows the final assembly of the first iPad holder. The feature of this design is contained the holder inside of the armrest which will not interfere with the users when they don't need to use the iPad. Moreover, due to the special connection between the holding arm and the iPad, users can take the iPad with them easily when they leave the wheelchairs.

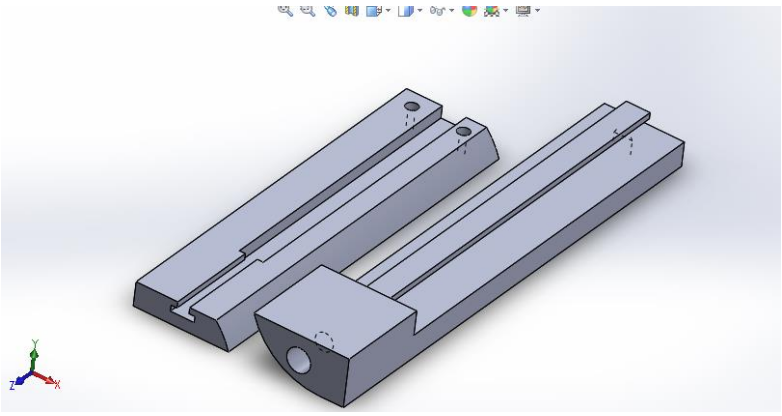

Figure 5.1 The two parts of the iPad holder frame. The right side part is used for rotating the iPad for a different view position and the left side part for adjusting the location of iPad in the horizontal direction, and these two parts able to be connected by the slot on each other

Figure 5.3 shows the prototype after manufacture and assembled to the electric wheelchair. We choose aluminum to manufacture each part due to its low price and low density. The milling machine is the main manufacture tool for cutting and drilling. We also added a 0.125in aluminum plat in the slot to increase the strength of the armrest.

Figure 5.2 3D Model of the first iPad holder. The left two images show the iPad and the holder in the usage position and the right two images show the retracted position of the iPad and holder

Figure 5.3 Final assembly of the first iPad holder. Top left image shows the retracted position of the iPad and holder. Top right side image shows the operating position of the iPad and holder. The bottom images shows the top view of different usage position of the iPad and holder

Figure 5.4 shows the second design and prototype of the iPad holder. The iPad holder is consisted of an iPad keyboard case and a goose neck which can rotate 360 degree. Both parts are commercially available. The goose neck is used to connect the bottom frame of the electric wheelchair and the keyboard case. A suction cup is used to fix the keyboard case on the goose neck. And to fold the keyboard case to the right side while the electric wheelchair is running, we installed a hinge between the keyboard case and the top of the goose neck. This Design is not lonely fit for the iPad, but also able to carry other devices like iPhone, laptop and so on.

Figure 5.4 Pictures of second prototype of the iPad holder. Left side image shows the operating position of the iPad and holder. The right side images show the procedure of folding the iPad to the right side of the armrest

3. Onboard USB Inverter and 110V Power Outlet

After the addition of so many electronic devices to the electric wheelchair, an on board charger is necessary. Maximal Power inverter was selected due to its multiple standard 110V stock and a unique build in USB charge stock. [32] What's more, the width of this inverter is smaller than the height of the armrest, so we can attach it to the

left side of the armrest without leaving any negative effect to the user. And there is a switch on the inverter which can turn off the inverter when it is not being used.

Figure 5.5 shows how the power inverter, voltage converter were connected to the circuit. The inverter and the hub motor are connected to the battery in parallel so that it can withdraw the current separately. In addition, to solve the different input voltage requirements between the inverter and hub motor, we used a high quality DC/DC Converter to reduce the voltage from 24V to 12V to fit the operating voltage of the inverter. *Figure 5.6* shows the voltage converter is attached to the frame of the electric wheelchair and *Figure 5.7* shows the inverter is charging an iPhone by using its USB stock.

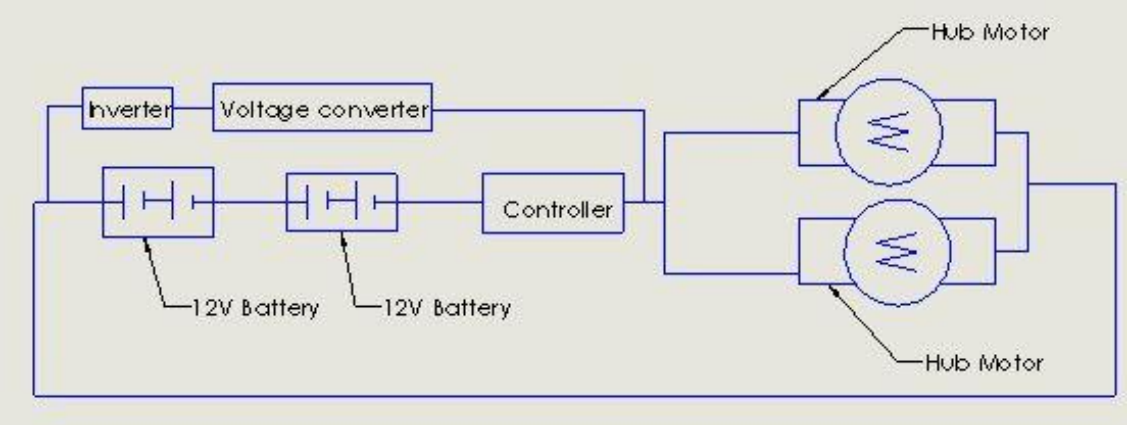

Figure 5.5 Circuit diagram shows the ability of batteries to support the power inverter and motors at same time. And the circuit connection of batteries, controller, motors, power inverter and voltage converter.

Figure 5.6 DC/DC converter used to change the 24V voltage from the battery to power the 12V power inverter. The device is attached to the back bottom frame of the electric wheelchair. There are four cables on the converter: two of them are connected to the batteries and the other two connected to the Power Inverter.

Figure 5.7 Left image shows a Maximal Power Inverter Outlet with three 110V stander stocks and one USB charge stock, attached to the left side armrest of the electric wheelchair. The right image shows an iPhone is charging onboard

4. Design of Rapid Battery Release/Replacement Mechanism

For the current Electric Wheelchair design, replacing the dead battery is very inconvenient. In many available electric wheelchairs, the design and structure restricts battery replacement. For instance, the seat and frame have to be taken away in order to replace the batteries. Disabled individuals can hardly to do such a work. Therefore they have to bring the chairs to the maintenance stores simply for battery replacement, which cost time and money. According to our survey, many individuals are considering to live in an independent life and are willing to perform such simple task at home if it is possible. In addition, they don't have time to wait for the battery recharge if they can rapidly replace with a pre-charged backup battery. In this section we will describe our designs of rapid battery release mechanisms.

Figure 5.8 shows the feature of first concept design. It consisted of a pair of slider an aluminum plate and 8 location adjustable jigs, by moving the slider in or out, user can change battery much easier than before. *Figure 5.9* shows more detail about this design the battery container was an aluminum plate with two slots and eight jigs on it. The four jigs on the short edge of the plate will hold the position of each battery, and the remaining four jigs will squeeze the other side of the batteries. The benefit of this design is that the squeezing jigs can move in the slot to fit different sizes of batteries. What's more, an 8 degrees angle was added between the slider and the ground so that the slop will make it easier for the users to pull out the batteries. When the slider is pushed back, a pair of spring locks will hold it in potion while the electric wheelchair is moving.

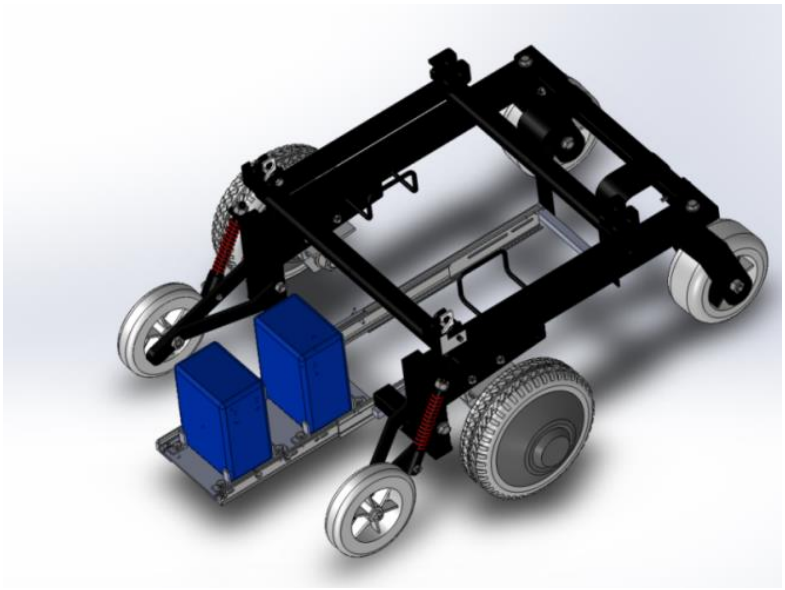

Figure 5.8 The first design of battery quickly release mechanism. The image shows the battery is out of the frame and ready for replacement

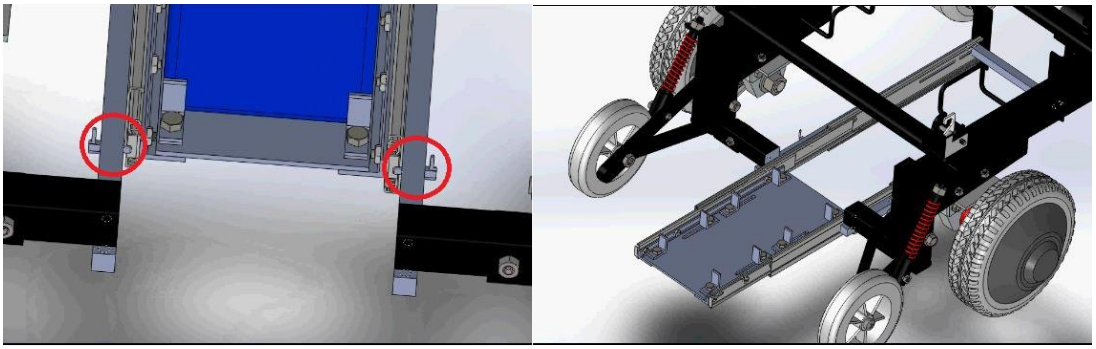

Figure 5.9 The left image shows the spring lock (circled area) used for holding the battery tray in position while the electric wheelchair is driving. The right side image shows the battery holding tray with eight adjustable jigs for holding different size batteries

Figure 5.10 shows an OEM drawer container is used for carrying 24V 50Ah batteries. The power socket is placed at the front of the slider. When someone pushes the drawer, it will slide to the end of the trial and be plugged into the stock. A pair of lockers located at the end of the slide trail to keep the container in position. With this mechanism, the batteries became an independent module which can be replaced quickly and easily.

Figure 5.11 shows more detail of this OEM battery container, is consist of Li ion batteries with different capacity for user to choose and the plug on the container need to be designed as a charge port and discharge port in order to reduce the component needed on the electric wheelchair. The material of this container was selected as ABS plastic due to the low weight, low price and high strength and the size of it is 15in. x8in. x3in. and the size will change with the capacity of batteries as well.

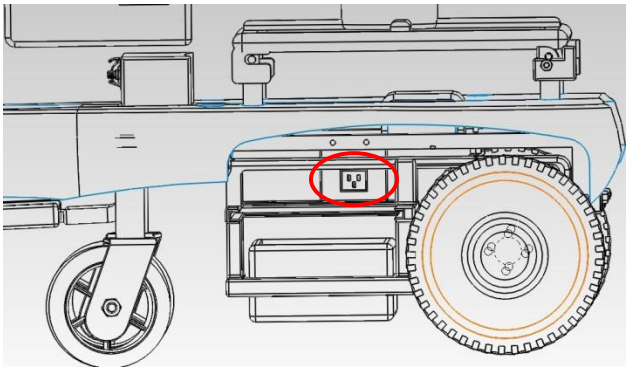

Figure 5.10 The second design of a quickly battery release mechanism. The image shows the support structure for battery container, the slider on each side for helping the user to drag out and slid in the battery container and a power stock which can be used for charging and discharging the batteries

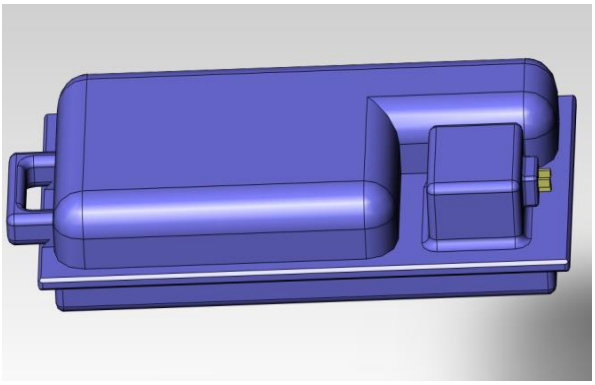

Figure 5.11 Battery container of the second quickly battery releases mechanism to pack batteries and its charger inside. From left to right is the handle, room for battery storage and the battery charger

5. Wheel Width Changeable Mechanism

The unchangeable wheel distance of the electric wheelchair will become a problem for the electric wheelchair users, when they have to pass some narrow area or door. In order to solve this problem, we come up with an idea of wheel width changeable mechanism.

*Figure 5.12(a) a*nd *(B)* shows more details about this mechanism. The components from left side to right side is the drive shaft (grey) with threads on it for retracting/extending the wheel, the support cylinder with threads inside (red) for connecting the mechanism to the frame of wheelchair and containing the drive shaft, and the motor (green) to drive the extension and retraction. In the end of this mechanism, a 24V motor will power it through a worm gear in order to convert the vertical rotation to horizontal rotation.

For the Jazzy 1113 electric wheelchair the width between the two wheels is 2.5 in. wider on each side than the armrests spacing of the seat. From *Figure 5.12* shows when users have to go through a narrow door or an aisle, the wheel width changeable mechanism can solve the problem by drawing back the axles of the two wheels 2.5 inch inside of the two cylinder container so that the width the between the wheels is the same as the armrests spacing of the seat.

(a)

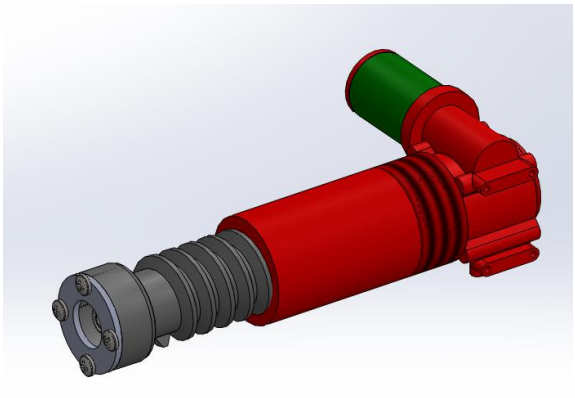

(b)

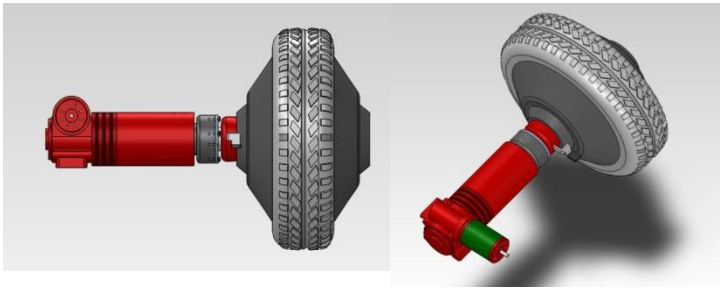

Figure 5.12 Solidworks images showing (a) the extended mode of wheel width changeable mechanism. The components from left side to right side is the drive shaft (grey) with threads on it for retracting/extending the wheel, the support cylinder with threads inside (red) for connecting the mechanism to the frame of wheelchair and containing the drive shaft, and the motor (green) to drive the extension and retraction; (b) the retracted position of wheel width changeable mechanism. The drive shaft is gradually threaded into the red cylinder part while the electric wheelchair is driving and retracts the wheel towards inside.

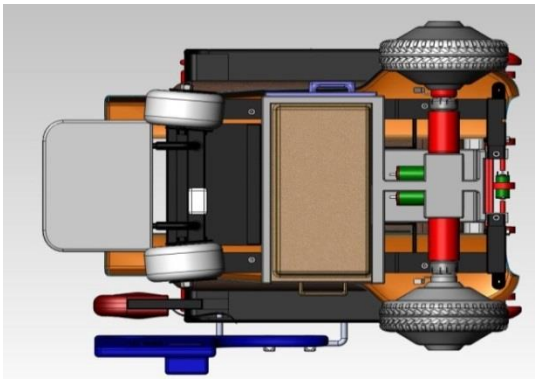

Figure 5.13 Solidworks image from the bottom view of the wheel width changeable mechanism assembled. The two red cylinders of this mechanism are welded to the support structure fixed to the wheelchair frame. The support structure also serves as for the battery container (see figure 5.10).

6. Conclusion

In this chapter, we designed and manufactured several onboard functional components and mechanism to improve the use experience of electric wheelchair. First of all, in order to add the telecommunication and navigation features to the electric wheelchair and free user's hand from holding these devices. Two kinds of iPad holder were designed, one is able to hold the iPad in front of the user and store it in the armrest while the electric wheelchair is running. The other one is able to fold to several positions for different usage.

Secondly, due to so many electronic devices were added to the electric wheelchair, an onboard charger is necessary. Maximal Power inverter Outlet was selected, due to its slim shape and 3 110V stander power stocks and one USB stock. However, the operating voltage of this device is 12V, a 24V to 12V converter were added to the circuit for reducing the voltage to its operating voltage.

In the last, two quickly battery releases mechanism and a wheel width changeable mechanisms were designed. The features of first quickly battery releases mechanism are location adjustable jigs for holding different size of batteries and two inclined slider supports on each side of the frame to help the user pull the battery out easily. The second quickly battery release is more like a concept design, a special battery container was designed to store all of the batteries and charger within it. With this design, the speed of battery replacement will be much faster than before and saved a lot of time to wait for the battery recharge. And several sizes and capacity of these containers will be made for user to choose. What's more, wheel width changeable mechanisms were deigned to add the

ability to the electric wheelchair to go through the narrow door or aisle. Under the help of the storage cylinder and the threads on it, the electric wheelchair able to contract the wheel 2.5in back on each side.

In conclusion, with these components and mechanism, the electric wheelchair will becomes more convenient and comfortable which helped the users to take a more active part in the social society.

Conclusions

First of all, some studies and new concepts which related to the design and test of Electric Wheelchair have been literature reviewed in chapter 2, the data and chart that published by these authors can be used as a reference to verify our tests and study.

Secondly, charge and discharge characteristic of several different kinds of battery were tested with Jazzy 1113 Power Chair. From the test, a lot of data were collected and category as different material and capacity. By compare the voltage and current of different batteries, we draw the conclusion that Li-ion batteries are more suitable for large current continuous output situation compare to Lead-acid batteries. The reason is due to the capacity can be utilized of lead-acid battery begin to decrease rapidly from 95% to50% as the increase of load on the seat. From the summary figure in chapter 3, we know that by changing the battery from Lead-acid to Li-ion, running time increased 0.4 hrs. , 2.4 hrs. , 2.2 hrs. and 2.1 hrs. under no load, 90lbs. load, 180 lbs. load, and 270 lbs. load cases respectively.

Thirdly, in order to reduce the energy consumption and extend more running time, the original gear motors on Jazzy 1113 Power Chair were replaced by a high efficient and lower weight hub motors and at the same time a maintenance free feature were added to the electric wheelchair as well. A connecting component was designed, for assembly the new hub motor to the frame of electric wheelchair.

From the motor comparison result demonstrated in chapter 3, for lead acid battery, the running time increased at least one hour under each case, because of the declension of continuous output current and efficient increase after the replacement of motor, which make the motor able to withdraw more capacity from the lead acid battery. But for the Li-ion battery, the performance is not very outstanding, only the running time of no load case increased one and a half hours, the running time of the other three cases are all increased less than half hour compare to the original gear motor. The main reason can be explained by the insensitive to the output current of li-ion battery compare to lead-acid battery. And the efficient increased and weight reduced form the motor not able to against the load added.

At last, for examining the efficient of different motor, an air cooling non-contact eddy current dynamotor have been studied and designed. The basic theory behind it is calculating the ratio between the input power from the motor and the torque generated by the eddy current brake. In the beginning, the one for high speed motor use dynamotor was not working successfully due to three design and manufacture problems, and which also makes us to reconsider and change the design of second dynamotor for low speed motor use in order to overcome those difficulties in manufacture and assembly stage, from the lessons we learned in the first one, we changed the stator from a round rod to a C-frame channel which solved the problems of short of magmatic wire turns and able to control the air gap more precisely. What's more, in order to make the electric wheelchair more comfortable and convenient for the disabled person to use, in chapter 5, some features and functions were added to the Electrical Wheelchair such as Usb and 110V power outlet, iPad holding arm.

With these improvements, the electric wheelchair not only became more reliable and more functional but also means the user have more chance to take an active part in the normal social activities.

Appendix

1. Hub Motor Specification

Part name:	SWXK
Rated Voltage (V)	24/36
Rated Power (W)	180~250
Max Diameter (mm)	134
Max Speed (rpm)	285
Rated Efficiency (%)	≥78%
2P	20
Reduction Ratio	01:04.4
Weight (kg)	≤3.0
Open size (mm)	100
Drive and freewheel type	Front
Spoke Specification	Front
Cable location	Shaft side right
Hall sensor	Optional
Integrate speed sensor	Optional
Connector	Optional
Brake type	V/Disc (>160)
Surface	Silver/Glossy black painted
Noise (dB)	<50
Salt fog test (h)	24/96
Water proof Grade	IP54
Certification	CE ROHS

2. Battery specifications

1. 12V 50Ah LifePo$_4$ Battery

NO.	ITEM		Specifications
3-1	Nominal Capacity:		50Ah
3-2	Rated voltage		12V
3-3	Internal Resistance		≤36mΩ
3-4	Max. charging current		50A
3-5	Max. charging voltage		14.6±0.05V
3-6	Max. continuous discharging current		100A
3-7	Max.pulse discharging current		450A
3-8	Terminal discharged voltage		10 ±2V
3-9	Cycle life (2000times)		≥35 Ah
3-10	Dimensions		222*158*200mm
3-11	Weight		Approx.8.1kg
3-12	Working temperature		-20~60℃
3-13	Storage temperature	In one month	-20~45℃
		In six months	-20~35℃
3-14	Working enviroment		
	RH		5%~95℃
	Absolute humidity		0.26~25g/m³
	ambient pressure		70kpa~106kpa

2. 12V 50Ah Lead Acid Battery

Battery Model	LP 12V 50AH	
Dimension	Length	257 ±3mm (10.11 inches)
	Width	132± 2mm (5.19 inches)
	Container Height	200± 2mm (7.87 inches)
	Total Height (with Terminal)	200± 2mm (7.87 inches)
Approx Weight	Approx 16.0 kg (35.3lbs)	
Terminal	T6	
Container Material	ABS	
Rated Capacity	52.0 AH/2.60A (20hr ,1.80V/cell,25^{0}C/77^{0}F) 50.0 AH/5.00A (10hr,1.80V/cell,25^{0}C/77^{0}F) 43.1 AH/8.62A (5hr,1.75V/cell,25^{0}C/77^{0}F) 39.0 AH/13.0A (3hr,1.75V/cell,25^{0}C/77^{0}F) 30.5 AH/30.5A (1hr,1.60V/cell,25^{0}C/77^{0}F)	
Max. Discharge Current	600A (5s)	
Internal Resistance	Approx 8.0mΩ	
Operating Temp.Range	Discharge : -15~50^{0}C (5 ~122^{0}F) Charge : 0~40^{0}C (32 ~104^{0}F) Storage : -15~40^{0}C (5~104^{0}F)	
Nominal Operating Temp. Range	25±3^{0}C (77±5^{0}F)	
Cycle Use	Initial Charging Current less than 15.0A.Voltage 14.4V~15.0V at 25^0 C(77^0 F)Temp. Coefficient -30mV/^{0}C	
Standby Use	No limit on Initial Charging Current Voltage 13.5V~13.8V at 25^0 C(77^0 F)Temp. Coefficient -20mV/^{0}C	
Capacity affected by Temperature	40 ^{0}C (104 ^{0} F) 103% 25 ^{0}C (77 ^{0}F) 100% 0 ^{0}C (32 ^{0}F) 86%	
Self-Discharge	Leoch LP series batteries may be stored for up to 6 months at 25^0 C(77^{0}F) and then a freshening charge is required. For higher temperatures the time interval will be shorter.	

3. Matlab Code for Dynamometer Torque Calculation

```
%Computation for Braking Torque of Eddy Current Retarder
%Dewei Guan 6/20/2012
%%%%%%%%%%%%%%%%%%Variable%%%%%%%%%%%%%%%%%%%%%%%%%%%%%%%%%%
clear all; clc
mm=10^-3;
in=0.0254;                  %m
r1=140*mm;                  %Inner radius(mm)
r2=238*mm;                  %Outer radius(mm)
h=16*mm;                    %Thickness (mm)
Np=4;                       %Number of the pairs of magnetic pole
d=87*mm;                    %Diameter of the stator
n=1000;                     %Number of revolutions
sigma=0.6e7;                %Electrical conductivity of the rotor plate
rho=1/sigma;                %electrical resistivity
w=2*pi*Np*n/60;             %Angular frequency of magnetic field changes
wn=pi*n/30;                 %Angular velocity of the plate
v=wn*(r2-r1);               %Linear speed of the plate
Sp=pi*d^2/4;                %Cross section area of the stator
Sd=pi*(r2^2-r1^2);          %Area of the rotor plate
mu0=4*pi*10^-7;             %Vacuum magnetic conductivity
N=350;                      %Number of turns
I=26.5;                     %Current (A)
sdelta=1.4*mm;              %Air gap (mm)
```

```
%%%%%%%%%%%%%%%%%%Equation of Eddy Current%%%%%%%%%%%%%%%%%%%%
%bdelta=sqrt(2/(sigma*mu*w));  %Average depth of penetration of the plate
Rm0=sdelta/(mu0*Sp)          %Magnetoresistance of Air gap (H^-1)
Em=N*I                       %Magnetomotive force (A*t)
Phi=Em/(2*Rm0)               %Magnetic flux (Wb)
B=Phi/Sd                     %Magnetic flux density (T)
Jm0=sigma*B*pi*n*(r2-r1)/30    %Jm0=sigma*B*v Current density amplitude (A/mm^2)

%%%%%%%%%%%%%%%%%%Equation of Braking Torque%%%%%%%%%%%%%%%%%%%%
mur=180;                     %Relative magnetic conductivity
mu=mur;
bdelta=sqrt(2/(sigma*mu*w));  %Average depth of penetration of the plate
%T=((pi*bdelta*(r2^2-r1^2)^2)/(2*rho*log(r2/r1)))*B^2*wn %Electromagnetic torque
T=((sqrt(6)*pi^3*d^4*N^2*I^2)/(480*log(r2/r1)*sdelta^2))*sqrt(n/(mur*rho*Np))*10^-10
T_tot=T*Np*2
```

References

[1] Steinmetz E. (2002). Americans With Disabilities 2002 in Current Population Reports, pp. 70-170. US Census Bureau, Washington DC. Available online at http://www.census/2006 /pubs/p70-107.pdf.

[2] Wheelchair Pride blog. Available at http://www.wheelchairpride.com/2010/07/how-manywheelchair-users-are-there.html

[3] Disability Statistics Center at UCSF. Available at http://dsc.ucsf.edu/publication.php

[4] A. Chih-Chiang Hua, , and B. Zong-Wei Syue. "Charge and Discharge Characteristics of Lead-Acid Battery and LiFePO4 Battery." The 2010 International Power Electronics Conference IEEE, 2010. 4244-5393. Print.

[5] Cowlishaw, M.F. (December 1974). "The Characteristics and Use of Lead-Acid Cap Lamps" (PDF). Trans. British Cave Research Association 1 (4): 199–214.

[6] Yoshihiko Takahashi, Syogo Matsuo, and Kei Kawakami (2010). *Energy Control System of Solar Powered Wheelchair, Solar Energy, Radu D Rugescu (Ed.), ISBN: 978-953-307-0520*

[7] Ur Réhman, Shafiq, Rännbäck, Sven, Liu, Li *"Tongue operated electric wheelchair "DIVA – Digital Vetenskapliga Arkivet, (2010)*

[8] Javier Minguez *"Brain-Computer Interfaces research" (2010)*

[9] T. Suzuki, M. Hashimoto, and K. Takahashi International Conference on Robotics and Biomimetic 2011 IEEE "Laser-*based Road Recognition for a Smart Electric Wheelchair*."

[10] Chalk, S. G.; and Miller, J. F. (2006) Key challenges and recent progress in batteries, fuel cells, and hydrogen storage for clean energy systems, Journal of Power Sources, 159 (1)

[11] GE's "Plug in" to Hybrid and Battery Technologies, 2008 Available at http://www.ge.com/battery/plugin.html

[12] Nguyen, J. (2005) Performance of Li-ion batteries in motive applications, http://www.battcon.com/PapersFinal2005/NguyenPaper2005.pdf

[13] Anderson, D.L. (2009) An evaluation of current and future costs for Lithium-ion batteries for use in electric vehicle powertrains, Master Thesis.

[14] Chaturvedi, N.A.; Klein, R.; Christensen, J.; Ahmed, J.; and Kojic, A. (2010) Algorithms for advanced battery-management systems, Control Systems, IEEE, 30(3), 49-68

[15] Cao, J.; Schofield, N.; and Emadi, A. (2008) Battery balancing methods: A comprehensive review, Vehicle Power and Propulsion Conference, IEEE, 1-6

[16] Ehsani, M.; Gao,Y.; and Emadi, A. (2009) Modern electric, hybrid electric, and fuel cell vehicles: fundamentals, theory, and design, CRC Press.

[17] Williamson, S.; Lukic, M.; and Emadi, A. (2006) Comprehensive drive train efficiency analysis of hybrid electric and fuel cell vehicles based on motor-controller efficiency modeling, Power Electronics, IEEE Transactions, 21(3), 730-740

[18] Chau, K.T.; Chan, C.C.; and Liu, C. (2008) Overview of permanent-magnet brushless drives for electric and hybrid electric vehicles, Bottom of Form Industrial Electronics, IEEE Transactions, 55(6) 2246-2257

[19] Gao, Y.; and Ehsani, M. (2006) A torque and speed coupling hybrid drivetrain-architecture, control, and simulation, Power Electronics, IEEE Transactions, 21(3) 741-748

[20] DeCicco, John M.; Kliesch, James. ACEEE's Green Book: The Environmental Guide to Cars and Trucks. ISBN 0-918249-45-7.

[21] Panasonic Sealed Lead-Acid Handbook, Matsushita Battery Industrial Page 1-77 January Feb 2000

[22] Mitsubishi Heavy Industries Technical Review Vol. 49 No. 1 (March 2012)

[23] DiGiovine, C. P. Power Wheelchair Batteries http://www.spinlife.com/s pintips/details/k/Power%20Wheelchai r%20Batteries/c/4.

[24] Y.-P. Yang, , W.-C. Huang, and C.-W. Lai. "Optimal design of rim motor for electric powered wheelchair." IET Electtr Power Appl. 1.5 (2007): 13. page. Web. 13 Feb. 2013.

[25] Kasuhiko Torii, Hamamatsu;KeijiInoue,Hamana-gun;Hiroaki Yamamoto,Kosai,all of(JP) "*MOTOR HAVING WORM GEAR MECHANISM*" Patent

[26] *C. Y. LIU*, K. J. JIANG, and Y. ZHANG. "DESIGN AND USE OF AN EDDY CURRENT RETARDER IN AN AUTOMOBILE."International Journal of Automotive Technology. 12.4 (2011): 611-616. Print.*

[27] JAZZY 1113 ATS available at http://www.pridemobility.com /pdf/ OwnersManuals/USJazzy/US_Jazzy_1113_ATS_om.pdf

[28] Engineeringtoolbox. (2005, 8 24). *Retrieved from www.engineeringtoolbox.com*

[29] Winther, Martin P. (1976). Eddy Currents. Cleveland, Ohio: Eaton Corporation.

[30] J.H.Wouterse.*Critical Torque of Eddy Current Brake with W idely Separated Soft Iron Poles. IEEE Proceed—ings,1991.138(6):153—158.*

[31] WU Ying—feng. , LI Gang—yan, *evaluation method of performance characteristic of eddy current retarder. china journal of highway and transport*, 19(5), 115-118. *China Journal of Highway and Transport*, (4), 7-8.

[32] E.simeu. , & D.georges, (1996). *Modeling and control of an eddy current brake. Pergamon*, 4(1), 19--26.

[33] Cool Tech PC. (n.d.). Papst 41240mm quite fan. *Retrieved from* http://endpcnoise.com/

[34] Maximal Power DC AC 200S 200 Watts DC 12V to AC 110V Continou Car/Vechicle Power Inverter Car Charge Converter with 3 Outlets and Built-in USB Port available at http://skeladoh.blogspot.com/2013/03/cheap-maximal-power-dc-ac-200s-200.html